NUMERICAL ANALYSIS OF DEEP RC BEAM WITH CIRCULAR HOLES THIN SHEAR PLATES

HO HONG YEU

A project report submitted in partial fulfilment of the requirements for the award of Bachelor of Engineering (Honours) Civil Engineering

Lee Kong Chian Faculty of Engineering and Science
Universiti Tunku Abdul Rahman

April 2021

DECLARATION

I hereby declare that this project report is based on my original work except for citations and quotations which have been duly acknowledged. I also declare that it has not been previously and concurrently submitted for any other degree or award at UTAR or other institutions.

Signature : *Ho Hong Yeu*

Name : Ho Hong Yeu

ID No. : 1602788

Date : 16 April 2021

APPROVAL FOR SUBMISSION

I certify that this project report entitled **" NUMERICAL ANALYSIS OF DEEP RC BEAM WITH CIRCULAR HOLES THIN SHEAR PLATES"** was prepared by **HO HONG YEU** has met the required standard for submission in partial fulfilment of the requirements for the award of Bachelor of Engineering (Honours) Civil Engineering at Universiti Tunku Abdul Rahman.

Approved by,

Signature : 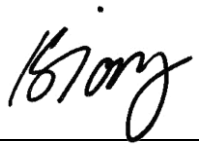

Supervisor : Woon Kai Siong

Date : 10/05/2021

ACKNOWLEDGEMENTS

I would like to extend my deepest gratitude to my final year project supervisor, Dr Woon Kai Siong. Dr Woon had dedicated his patient guidance, enthusiastic encouragement, and beneficial critiques throughout the entire study. First, he guided me in constructing the fundamental of this study. Besides, he sacrificed his precious time organizing training sessions to teach the operation of ABAQUS software. Lastly, he always contributes his invaluable advice in polishing the content in my report.

I would also like to extend my sincere thanks to my research moderator, Dr Lau See Hung. Dr Lau had provided plenty of constructive comments in correcting the shortcomings in my study. Also, the time and attention she had paid during my project presentation.

Last but not least, I gratefully acknowledge the assistance from my friends, Mr Lee Yi Han, Mr Chow Melvyn, Mr Tang Wee Jian, and Mr Chai Khem Fei.

This study would never be completed in the absence of either party.

ABSTRACT

Reinforced concrete (RC) deep beam in massive structures are constructed to provide sufficient load carrying capacity. However, concrete honeycomb due to reinforcement congestion is a common problem in RC deep beam. Circular holes thin shear plates appear to be an effective substitute to conventional shear links, providing higher load carrying capacity yet using less space. Finite element analysis (FEA) using ABAQUS software is capable of solving complex deep beam problems in a timely and cost-effective manner. In this study, a numerical model was established to yield good matching results to the experimental results published by Jasim, et al. (2020). The verified numerical model was used to further study the test specimens with 50 mm, 75 mm, 100 mm, 125 mm, and 150 mm circular holes spacing. Load-displacement curves were plotted to evaluate the load-carrying capacity of the test specimens. A maximum 2.90 % improvement was observed in the test specimen with 100 mm circular holes spacing, N100. Therefore, N100 was determined as the optimum design for the further discussion of stress distribution and crack pattern. Von Mises stress contour of the concrete and reinforcement were generated to investigate the stress distribution over the loading process. Reinforcement stress capacity of N100 is increased by 1.79 %, but concrete stress capacity is reduced by 2.23 %. Plastic strain magnitude (PEMAG) diagram and concrete tension damage contour provide a clear visualization of the crack pattern. Shear compression failure is deduced based on the diagonal cracks accumulating at the concrete strut.

TABLE OF CONTENTS

TABLE OF CONTENTS **i**

LIST OF TABLES **iii**

LIST OF FIGURES **iv**

LIST OF SYMBOLS / ABBREVIATIONS **viii**

LIST OF APPENDICES **x**

CHAPTER

1 INTRODUCTION **1**

1.1 General Introduction 1

1.2 Importance of the Study 1

1.3 Problem Statement 2

1.4 Aim and Objectives 3

1.5 Scope and Limitation of the Study 4

1.6 Outline of the Report 4

2 LITERATURE REVIEW **5**

2.1 Introduction 5

2.2 Detailing to Improve Load Carrying Capacity 6

2.2.1 External Steel Plating System 6

2.2.2 External FRP System 10

2.2.3 Internal/ Near Surface Mounted (NSM) FRP System 13

2.2.4 Embedded Steel Section 16

2.3 Reinforcement Methods to Ease Reinforcement Congestion 17

2.4 Finite Element Analysis 20

2.4.1 Structural Finite Element Analysis 20

2.5 Summary 29

3 METHODOLOGY **30**

3.1 Introduction 30

3.2 Historical Work 31

	3.3	Specimen Specification		32
		3.3.1	Reference Beam (Jasim, et al., 2020)	32
		3.3.2	Control Beam	33
		3.3.3	Test Specimens	34
	3.4	Numerical Modelling		36
		3.4.1	Material Properties	37
		3.4.2	Interaction Properties	43
		3.4.3	Element Type and Mesh Size	44
		3.4.4	Boundary Conditions and Load Definition	45
	3.5	Results Verification		46
	3.6	Optimization		46
	3.7	Summary		47
4	**RESULTS AND DISCUSSIONS**			**48**
	4.1	Introduction		48
	4.2	Model Validation with Reference Beam		48
	4.3	Control Beam with Conventional Shear Link		51
	4.4	Test Specimens with Circular Holes Thin Shear Plates		52
		4.4.1	Load-displacement Curve	52
	4.5	Optimization		58
	4.6	Generalization and Comparison between Control Beam, C01 and Test Specimen, N100		58
		4.6.1	Concrete Von Mises Stress Contour	58
		4.6.2	Reinforcement Von Mises Stress Contour	61
		4.6.3	Plastic Strain Magnitude (PEMAG) Diagram	64
		4.6.4	Concrete Tension Damage Contour	66
	4.7	Summary		69
5	**CONCLUSION AND RECOMMENDATIONS**			**70**
	5.1	Conclusion		70
	5.2	Recommendations		71
REFERENCES				**73**
APPENDICES				**78**

LIST OF TABLES

Table 3.1: Reference Beam Geometry and Material Properties. 32

Table 3.2: Control Beam Geometry and Material Properties. 34

Table 3.3: Test Specimens Specification. 35

Table 3.4: Concrete Parameters of CBP Model (Demir, et al., 2016). 38

Table 3.5: Steel Reinforcing Bar Parameters (Terng, 2019). 42

Table 3.6: Steel Plate Parameters (Terng, 2019). 43

Table 4.1: Test Results of Jasim, et al. (2020) Experimental RC Deep Beam, and Reference Beam, R01. 49

Table 4.2: Results of Test Specimens. 56

Table 4.3: Concrete Von Mises Stress Magnitude. 61

Table 4.4 Reinforcement Von Mises Stress Magnitude. 63

LIST OF FIGURES

Figure 2.1: Bolted Steel Plates Deep Beam Detailing (Barnes, et al., 2001). 7

Figure 2.2: Bolted Side Steel Plate Beams Detailing (Zhu, et al., 2007). 8

Figure 2.3: Bolted Side-plated RC Beams Detailing (Li, et al., 2017). 9

Figure 2.4: SCS Deep Beam Configuration (Leng, et al., 2015). 10

Figure 2.5: CFRP Strips and CFRP Fabrics Detailing (Zhang, et al. 2004). 11

Figure 2.6: Externally Bonded FRP Systems (Islam, et al., 2005). 12

Figure 2.7: Externally Bonded FRP Systems (Maaddawy and Sherif, 2009). 13

Figure 2.8: Detailing of FRP-reinforced Deep Beam (Farghaly and Benmokrane, 2013). 14

Figure 2.9: FRP and WMM Strengthening Scheme (Albidah, et al., 2019). 15

Figure 2.10: Failure of FRP and WMM Deep Beam (Albidah, et al., 2019). 15

Figure 2.11: Aligned (Left) and Unaligned (Right) Configuration with 3 NSM-FRP and 3 Steel Stirrups (Ibrahim, et al., 2020). 16

Figure 2.12: SRC Deep Beam Detailing (Chen, et al., 2018). 17

Figure 2.13: SFRLC Beam Detailing (Kang, et al., 2012). 18

Figure 2.14: Bundle Diagonal Reinforced Coupling Beams (Khai, et al., 2017). 19

Figure 2.15: SCC and VC Beams Detailing (Kefelegn and Gebre, 2020). 19

Figure 2.16: BSP Beams Detailing (Li, et al., 2018). 22

Figure 2.17: Crack Patterns from Experimental Observation and Numerical Analysis (Li, et al., 2018). 22

Figure 2.18: Load-deflection Curves of BSP Beam (Li, et al., 2018). 22

Figure 2.19: Crack Patterns from Experimental Observation and Numerical Analysis (Jasim, et al., 2020). 23

Figure 2.20: Load-deflection Curves of CFRP Beam (Jasim, et al., 2020). 23

Figure 2.21: Tested Specimens with Various Location of CFRP Reinforcement (Hawileh, et al., 2012). 24

Figure 2.22: Expreimental Crack Patterns and Numerical Principal Compressive Stress (Hawileh, et al., 2012). 24

Figure 2.23: GFRP Deep Beam Detailing (Metwally, 2015). 25

Figure 2.24: Load-deflection Curves of GFRP Deep Beam (Metwally, 2015). 25

Figure 2.25: Crack Patterns from Experimental Observation and Numerical Analysis (Metwally, 2015). 26

Figure 2.26: Detailing with Embedded Struts (Ibrahim, et al., 2018). 27

Figure 2.27: Detailing with Intensify Ties (Ibrahim, et al., 2018). 27

Figure 2.28: Crack Patterns from Experimental Observation and Numerical Analysis (Ibrahim, et al., 2018). 27

Figure 2.29: Numerical Load-deflection Curve (Chiriki and Harsha, 2020). 28

Figure 2.30: Von Mises Stress Contour of DB2 (Chiriki and Harsha, 2020). 29

Figure 3.1: General Flow of the Research Methodology. 31

Figure 3.2: Reference Beam Detailing, R01 (Jasim, et al., 2020). 33

Figure 3.3: Reference Beam Experimental Load-displacement Curve (Jasim, et al. 2020). 33

Figure 3.4: Experimental Observation (Left) and Numerical Simulation (Right) of Reference Beam Failure Behaviour (Jasim, et al., 2020). 33

Figure 3.5: Control Beam Detailing, C01. 34

Figure 3.6: Specimen Detailing: (a) N50 (b) N75 (c) N100 (d) N125 (e) N150. 35

Figure 3.7: Modified Tension Stiffening Model (Wahalatantri, et al., 2011). 40

Figure 3.8: Concrete Stress-strain Curve in Compression. 40

Figure 3.9: Concrete Stress-strain Curve in Tension. 41

Figure 3.10: Concrete Compression Damage Curve. 41

Figure 3.11: Concrete Tension Curve. 41

Figure 3.12: Stress-strain Relationship of Steel Reinforcing Bar (Terng, 2019). 42

Figure 3.13: Stress-strain Relationship of Steel Plate (Terng, 2019). 43

Figure 3.14: Surface-based Tie Constraint on Solid Surface (Dassault Systèmes Simulia Corp., 2017). 44

Figure 3.15: Embedded Elements (Dassault Systèmes Simulia Corp., 2017). 44

Figure 3.16: Translation and Rotational Degrees of Freedom (Dassault Systèmes Simulia Corp., 2014). 46

Figure 4.1: Load-displacement Curve of Jasim, et al. (2020) Experimental RC Deep Beam, and Reference Beam, R01. 49

Figure 4.2: Experimental Cracking (Jasim, et al., 2020). 50

Figure 4.3: Tension Damage Contour of R01. 50

Figure 4.4: Load-displacement Curve of Control Beam, C01. 52

Figure 4.5: Load-displacement Curve of C01 and N50. 53

Figure 4.6: Load-displacement Curve of C01 and N75. 53

Figure 4.7: Load-displacement Curve of C01 and N100. 54

Figure 4.8: Load-displacement Curve of C01 and N125. 54

Figure 4.9: Load-displacement Curve of C01 and N150. 55

Figure 4.10: Enlarged View at the Yield Point. 55

Figure 4.11: Enlarged View at the Fracture Zone. 56

Figure 4.12: Concrete Von Mises Stress Contour of C01 at 1.5 mm. 59

Figure 4.13: Concrete Von Mises Stress Contour of C01 at 10 mm. 60

Figure 4.14: Concrete Von Mises Stress Contour of N100 at 1.5 mm. 60

Figure 4.15: Concrete Von Mises Stress Contour of N100 at 10 mm. 60

Figure 4.16: Reinforcement Von Mises Stress Contour of C01 at 1.5 mm. 62

Figure 4.17: Reinforcement Von Mises Stress Contour of C01 at 10 mm. 62

Figure 4.18: Reinforcement Von Mises Stress Contour of N100 at 1.5 mm. 63

Figure 4.19: Reinforcement Von Mises Stress Contour of N100 at 10 mm. 63

Figure 4.20: PEMAG Diagram of C01 at 1.5 mm. 65

Figure 4.21: PEMAG Diagram of C01 at 10 mm. 65

Figure 4.22: PEMAG Diagram of N100 at 1.5 mm. 65

Figure 4.23: PEMAG Diagram of N100 at 10 mm. 66

Figure 4.24: Tension Damage Contour of C01 at 1.5 mm. 67

Figure 4.25: Tension Damage Contour of C01 at 6 mm. 68

Figure 4.26: Tension Damage Contour of C01 at 10 mm. 68

Figure 4.27: Tension Damage Contour of N100 at 1.5 mm. 68

Figure 4.28: Tension Damage Contour of N100 at 6 mm. 69

Figure 4.29: Tension Damage Contour of N100 at 10 mm. 69

LIST OF SYMBOLS / ABBREVIATIONS

Ø	diameter, (mm)
ρ	density, kg.m^3
f_{ck}	characteristic compressive strength, MPa
f_{yk}	characteristic tensile strength
f_{ctm}	mean tensile strength, MPa
E	modulus of elasticity, MPa
v	Poisson's ratio
ψ	dilation angle, $^\circ$
ϵ	eccentricity
σ_{b0}/σ_{c0}	yield stress ratio
K_c	ratio of the second stress invariant on the tensile meridian
μ	viscosity
ω_c	compression stiffness recovery
ω_t	tensile stiffness recovery
f_c	compressive stress on the descending limb, N/mm^2
$f_c^{'}$	peak compressive stress, N/mm^2
σ	tensile stress on the descending limb, N/mm^2
σ_{t0}	peak tensile stress, N/mm^2

RC	reinforced concrete
STM	strut and tie method
FEM	finite element method
FEA	finite element analysis
SRC	steel-shaped reinforced concrete
SFRC	steel-fibre-reinforced concrete
FRP	fiber reinforced polymer
CFRP	carbon fiber reinforced polymer
GFRP	glass fiber reinforced polymer
BSP	bolted side plating
SCS	steel-concrete-steel
NSM	near surface mounted
WWM	welded wire mesh

NSM-FRP	near-surface mounted hybrid carbon-glass fiber reinforced polymer strips
CSS	critical shear span
SFRLC	steel fiber reinforced lightweight concrete
SCC	self-compacting concrete
VC	vibrated concrete
CDP	concrete damage plasticity
LVDT	linear variable differential transducer

LIST OF APPENDICES

APPENDIX A: Design Calculations 78

APPENDIX B: Test Results Graphics 88

CHAPTER 1

INTRODUCTION

1.1 General Introduction

Reinforced concrete (RC) deep beam is a structural member widely used in the construction field. It is built in structure that supports massive loading over a small span, such as pile cap, transfer girder, strap beam in foundations, panel beam, shear wall, etc. (Raj and Gangolu, 2013). Implementation of RC deep beam as the transfer girder can provide more clear space at the lower floors because high strength RC deep beam reduces the usage of columns (Siow, 2015).

According to the BS EN 1992-1-1:2004 (European Commisssion, 2004), a beam with a clear span length less than three times its overall depth is classified as a deep beam. Unlike the analysis of conventional beams that focuses on their flexural behaviour only, deep beam considers both its shear behaviour as well as flexural behaviour. Beams are generally divided into the Bernoulli regions (B-Region) and the Disturbed regions (D-Region). Deep beam is categorized under the D-Region, where the strain distribution is nonlinear, and shear becomes critical (Mohamed, et al., 2014). Hence, the Euler-Bernoulli hypothesis that disregards the shear deformation effect is not applicable in deep beam design (Adinkrah-Appiah, et al., 2015). Two common methods used to solve deep beam problems are the finite element method (FEM) and strut and tie method (STM). Both FEM and STM require complex and tedious calculation, which is difficult to compute manually, hence requiring a lot of time, cost, and workforce if without the aid of computer software. ABAQUS and ANSYS are common examples of computer-aided engineering software used in this study to perform the numerical analysis of RC deep beam.

1.2 Importance of the Study

RC deep beam is the critical safety structural system supporting massive loads over a short span at transfer girders in high-rise buildings and bridges (Ismail, 2016). According to Yang, et al. (2003), the shear action with compression in diagonal direction and tension in a perpendicular direction exerted by heavy

loads will disturb the internal stresses and eventually deteriorate the load carrying capacity of the RC deep beam. Therefore, shear reinforcement becomes an important criterion in deep beam detailing design. The amount of shear reinforcement required increases as the load capacity of the deep beam increases.

However, the increasing amount of reinforcement leads to another problem, which is congested reinforcement. Congested reinforcement affects the workability and performance of the concrete during the casting process (Choi, et al., 2012). Congested reinforcement slows down the work of reinforcing contractors, as well as the ability of the concrete contractor to obtain proper concrete consolidation (Risser and Hoffman, 2010). According to American Concrete Institute (2014), it is the designers' obligation to ensure that all the reinforcement is assembled and placed appropriately for the concrete to consolidate fully. Unconsolidated concrete, also known as concrete honeycombs, weakens the load-bearing capacity of the concrete, causing the structure to not perform adequately as per design. Besides, water can easily inflow the honeycombs and corrode the reinforcement underneath, resulting in a loss of grip between concrete and reinforcement, which shortens the structure's lifespan.

Therefore, an optimum detailing of shear reinforcement is crucial in deep beam design. In this study, circular holes thin shear plates with various opening diameter and spacing are tested to substitute conventional shear stirrups in RC deep beam.

1.3 Problem Statement

Shear behaviour is rather critical in RC deep beam, such that continuous assessment and research become essential to explore this field (Leng, et al., 2015). In the past decades, studies had been conducted to improve the load carrying capacity of heavy-loaded RC deep beam by either adding additional reinforcement, modifying concrete mix design, or revising the shear reinforcement detailing. Li, et al. (2017) and Zhu, et al. (2007) proposed externally bolted steel plates on the vertical web surface of RC beam. Meanwhile, Chen, et al. (2018) proposed embedded wide flange H-section into steel-shaped reinforced concrete (SRC) deep beam. Current research available focus on revising the shear detailing of RC members supporting heavy loads.

However, there is a limited amount of research work available to explore the shear detailing of RC deep beam to support mild shear loads.

Reinforcement congestion is one of the most common causes of concrete honeycomb. Thus, professionals are discovering solutions to ease congested steel to solve honeycomb that deteriorates the strength of concrete structural members. Khai, et al. (2017) studied the effectiveness of bundled diagonal reinforcement to replace conventional transverse reinforcement in steel-fiber-reinforced concrete (SFRC) coupling beam in seismic action. Nevertheless, the research works are limited to detailing for slender beam and coupling beam. Therefore, a proposed detailing to ease reinforcement congestion in deep beam needs further exploration in this study.

Finite element analysis is well-known as a time and cost-saving approach to predict the loading behaviour and the crack pattern of structural members. Jasim, et al. (2020) numerically analyzed the failure mode, and load capacity of RC deep beam strengthened externally with carbon fiber reinforced polymer (CFRP) sheets at the web surface. The numerical model was proven accurate after validation with experimental results published by Jasim, et al. (2018). Reported studies in the literature have confirmed the validity of finite element numerical analysis on strengthening schemes such as fiber reinforced polymer (FRP) system, bolted plates, and embedded steel section. However, to the author's knowledge, the numerical study on the proposed RC deep beam embedded with circular holes thin shear plates is yet to be discovered and discussed.

1.4 Aim and Objectives

This study aims to perform a numerical analysis of RC deep beam with circular holes thin shear plates. The study objectives are listed as follows:

i. to verify the numerical results of the reference beam with the experimental results.
ii. to evaluate the load-displacement behaviour of RC deep beam with circular holes thin shear plates.
iii. to determine an optimum design of RC deep beam embedded with circular holes thin shear plates of various opening spacing.

1.5 Scope and Limitation of the Study

The numerical analysis is performed using ABAQUS, a nonlinear finite element modelling software to predict the behaviour of concrete members. The scope of the study is:

i. the deep beams are tested for the shear behaviour instead of the flexural behaviour.
ii. the loading condition is monotonic loading.
iii. the support condition is simply roller support on both ends.
iv. the concrete mix is premixed normal strength concrete.

1.6 Outline of the Report

Chapter 1 gives a general introduction to the topic studied. Also, it describes the importance and problem statements that initiated this study. The study's aim and objectives are highlighted in this chapter, along with the scope and limitations.

Chapter 2 contains a detailed review of sufficient literature in the past to identify the research gap. The literature review is performed based on the problem statement, which focuses on the proposed shear detailing to improve the load carrying capacity, solve reinforcement congestion issue, and apply finite element analysis in the study of concrete structures.

Chapter 3 outlines the methodology applied in the numerical study. A general flow of study is established to describe the four main parts of the numerical study, including numerical modelling, numerical analysis, results verification, and optimization.

Chapter 4 discusses the outcome of the study in detail. Graphical representations such as load-displacement curves, von Mises countours, plastic strain magnitude (PEMAG) diagrams, and concrete tension damage contours are provided to study the trend and relationship between the study variables.

Chapter 5 concludes the entire and summarizes the outcomes in short based on the discussion in Chapter 4. This chapter also identifies the inadequacy and limitations of this study. Recommendations are provided to improve and resolve the shortcomings in this study for further research purposes.

CHAPTER 2

LITERATURE REVIEW

2.1 Introduction

In the case study of conventional RC beam, where the probability of flexural failure is much greater than shear failure, and shear reinforcement analysis is often neglected. However, in deep beam, shear deformations are more considerable than flexural failure. Shear creates cracks that lead to diagonal compression failure and diagonal tension failure in deep beams (Osman, 2008). Research was conducted to propose novel shear detailing to improve the load carrying capacity of deep beam.

Reinforcement congestion has always been the main concern in the design of heavy-loaded structural members such as deep beam, beam-column junction, and bridge deck slabs. Reinforcement congestion leads to serious construction problems such as difficulties in placing and compacting concrete, especially at critical regions subjected to high bending moment and shear force (Kotsovos, et al., 2013). Improper placement and compaction of concrete create concrete honeycomb that deteriorates the load carrying capacity of the structural member. Therefore, various substitutes of conventional shear reinforcement had been discovered to ease the reinforcement congestion issue.

Strut and tie method (STM) is a common approach in the analysis of deep beam. STM divides a structural component into Bernoulli region (B-region) and Disturbed region (D-region). The Euler-Bernoulli hypothesis is only applicable in the B-region, where the plane section remains plane upon loading. Deep beam is analyzed in the D-region, where there are disturbances of stress distribution caused by concentrated forces or abrupt changes of geometry (Beres and Rabbat, 2007). STM illustrates a deep beam approximated with simple truss elements, including compression struts, tension ties, and connecting nodes (Mohammadhassani, et al., 2013). Even though STM is a typical approach in the design of D-region, but it still has the limitations of (1) difficult to determine the optimum truss configuration for some loaded structural members, (2) incapable of predicting the failure modes (Tan, et al., 2003 and Yang, et al., 2006). Therefore, finite element analysis (FEA) software serves as an alternative

to study the behaviour of RC deep beam in terms of the failure mode, load-deflection behaviour, and crack pattern. The numerically generated results are validated with existing experimental results published in the literature to evaluate the reliability of the FEA model.

Throughout the Chapter 2, the author reviewed sufficient literature to identify the research gap for the proposed detailing of RC deep beam with circular holes thin shear plates.

2.2 Detailing to Improve Load Carrying Capacity

Reinforced concrete (RC) deep beam is a popular choice in massive structures and shear is rather critical than flexural. Failure of RC deep beam could cause severe consequences such as injury and fatality. Construction accidents around the world warn engineers to take careful structural design steps. Reinforcement detailing design must strictly follow code provisions to avoid any under-designed structures, especially for huge members. However, conventional shear stirrups in RC deep beam might have reduced load carrying capacity due to loss of bonding strength between the stirrups and concrete. Therefore, novel shear detailings such as external steel plating sytem, external FRP system, near surface mounted FRP system, and embedded steel section were studied to improve the load carrying capcity of RC deep beam (Barnes, et al., 2001; Zhang, et al., 2004; Ibrahim, et al., 2020; Chen, et al., 2018).

2.2.1 External Steel Plating System

Barnes, et al. (2001) examined the effectiveness of externally attached steel plates in improving RC deep beam overall performance. Four deep beam specimens were attached with steel plates to the vertical left and right sides of the beam using epoxy resin to achieve adhesive bonding. Three specimens were attached with steel plates fixed with 16 mm bolts, as shown in Figure 2.1. There were steel plates with thicknesses of 2 mm, 4 mm, and 6 mm. The common conclusion for bonded and bolted steel plates was they provided significant improvement to the serviceability and ultimate load carrying capacity of the deep beam, provided proper plate anchorage be achieved. Moreover, deep beam attached with 2 mm thin plates was enhanced in terms of its shear capacity, while beams with 4 mm and 6 mm thick plates were enhanced in terms of

flexural capacity. By comparison, deep beam with bolted steel plates performed better than bonded steel plates, which could uphold higher experimental loading and larger deflection. However, bonded steel plates had the advantages of good surface cracking control, smooth external surface, and even stress distribution. Therefore, combining bonded and bolted steel plates might prove to be more efficient for the serviceability and ultimate limit states.

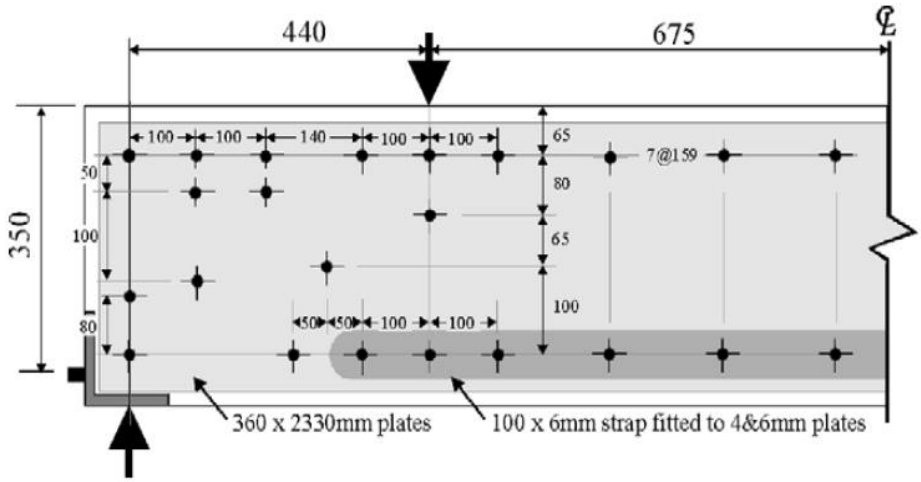

Figure 2.1: Bolted Steel Plates Deep Beam Detailing (Barnes, et al., 2001).

Zhu, et al. (2007) experimentally tested the behaviour of RC coupling beam strengthened with bolted side steel plates under reversed cyclic loading. The study focused on the load carrying capacity, deformation capacity, stiffness, strength degradation, and energy dissipation ability. Four coupling beam specimens were fabricated with 3 mm, and 6 mm bolted side steel plates and different shear connector arrangements. One specimen acts as the control specimen, as shown in Figure 2.2. Bolt connection was chosen over adhesive bonding because bolted steel plates are more durable over a long-term period. From the experimental results, bolted side plates significantly improved the load carrying capacity of the beam up to 96 % and the deformation capacity up to 90 %. Thicker steel plates provided a better enhancement to the beam load and deformation capacity. There was also a maximum increment in the stiffness of about 9 %. In addition, the beam with thick plates had the least strength degradation, with nearly 85 % strength retention capacity in all the loading cycles. Lastly, the ductile steel bolted to the beam increased the energy dissipation ability of the beam via inelastic deformation.

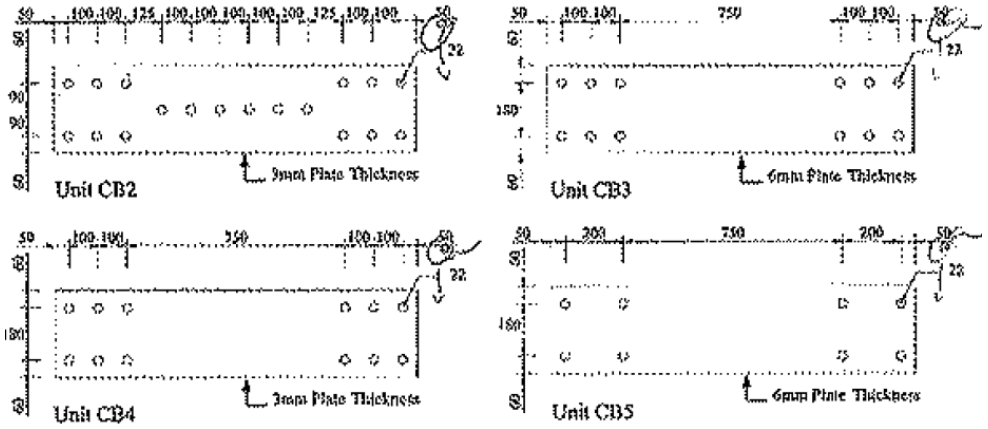

Figure 2.2: Bolted Side Steel Plate Beams Detailing (Zhu, et al., 2007).

Li, et al. (2017) experimented on the performance RC beam reinforced with bolted side-plating (BSP) technique. Steel plates were externally bolted at the vertical web surface of the beam. Seven beam specimens were prepared, one as the control and another six specimens varied in plate thickness, plate depth, bolt spacing, and the use of stiffeners, as shown in Figure 2.3. As a result, the BSP technique changed the failure mode of the beam from shear-tension failure to shear-compression failure, which happened in the shear span caused by the combination of concrete crushing and the development of shear cracks. BSP had no obvious effect on the initial flexural crack load. However, deeper steel plates and smaller horizontal bolt spacing significantly increased the diagonal cracking load. Moreover, BSP significantly enhanced the beam load carrying capacity ranging from 17 % to 50 %, particularly beam bolted with thick and deep plates. Thick and deep bolted steel plates had higher tensile strength and larger inertia moment. Thus, they could provide a greater enhancement in the load carrying capacity. BSP enhanced the stiffness of the beam as well, ranging from 11 % to 46 %. Stiffeners improved the stiffness by 20 % as compared to the BSP beam without a stiffener. However, additional stiffeners could merely improve the stiffness but exhibited negligible improvement in other aspects. Lastly, BSP improved the ductility of the beam as well, ranging from 19 % to 362 %.

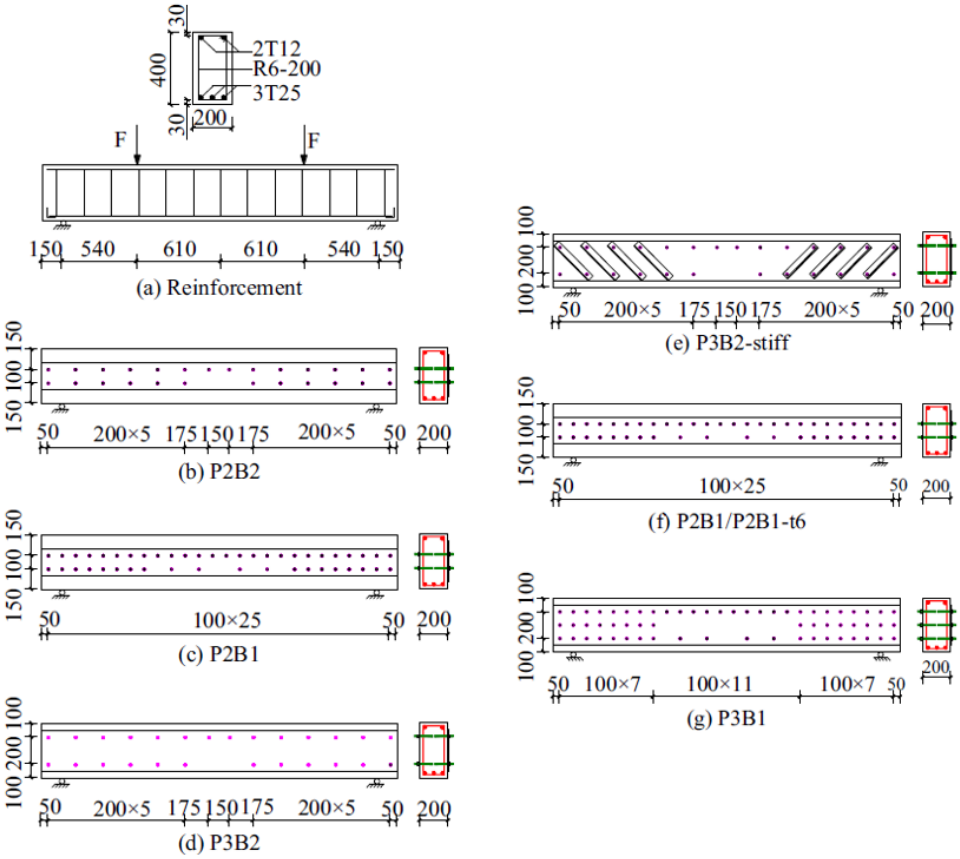

Figure 2.3: Bolted Side-plated RC Beams Detailing (Li, et al., 2017).

Leng, et al. (2015) investigated the failure mechanism and shear carrying capacity of both the simply supported and continuous steel-concrete-steel (SCS) sandwich deep beam. The concept of SCS composite structure was first discovered by Solomon, et al. (1976). Slipping failure between the steel plates and the concrete surface was a major problem in the design. Therefore, Leng, et al. (2015) modified the SCS system by replacing epoxy with headed studs to connect the steel plates to the top and bottom surface of the deep beam, as shown in Figure 2.4. As a result, the load carrying capacity of the deep beam had improved significantly, contributed by the strength of the bottom steel plate and the shear connectors. Furthermore, the failure pattern of SCS deep beam is different from typical RC structures because the membrane action of the outer steel plates improves the ductility properties of the deep beam. The simply supported SCS deep beam failed under 'bottom triangular area damage + horizontal cracking', while the continuous SCS deep beam failed under 'top + bottom triangular area damage.'

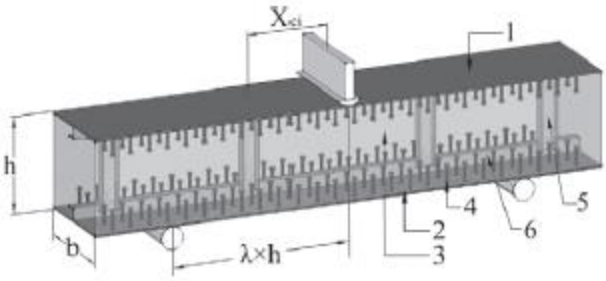

1: top steel plate; 2: bottom steel plate; 3: concrete core; 4: headed stud; 5: channel steel; 6: angle steel

Figure 2.4: SCS Deep Beam Configuration (Leng, et al., 2015).

Externally bonded or bolted steel plates have been proved effective in increasing the load carrying capacity of deep beams. However, the externally mounted steel plates are prone to moisture in the surrounding. Direct contact with moisture will corrode the plates and eventually deteriorate their strength.

2.2.2 External FRP System

Zhang, et al. (2004) experimented on RC deep beam strengthened with epoxy bonded carbon fiber reinforced polymer (CFRP) reinforcement in terms of the shear behaviour. Conventional steel stirrups were replaced by CFRP strips and CFRP fabrics bonded externally at the left and right surface of the deep beam. A total of eight specimens under one-point loading were divided into two groups, with one control specimen and three specimens with different CFRP detailing in each group, as shown in Figure 2.5. The results showed that CFRP strips enhanced the load carrying capacity of the beam up to 196.99 kN, which is twice the capacity of the control beam with 97.79 kN. Simultaneously, the CFRP fabrics enhanced the load carrying capacity up to 192.22 kN, which is 222 % of the control beam with 86.33 kN capacity. Moreover, CFRP reinforcement improved the ductility of the deep beam until it became brittle after reaching ultimate loading.

Islam, et al. (2005) tested the performance of RC deep beam strengthened with externally bonded fiber reinforced polymer (FRP) systems. Six specimens were prepared, with one control specimen, while the other five were strengthened with FRP wrap, strip, or grids, as shown in Figure 2.6. All the FRP reinforcement was bonded to the left and right surface of the deep beam using epoxy. Grid 1, Grid 2, and Grid 3 had different grid bar cross sectional

areas of 6.6 mm^2, 17.5 mm^2, and 39.2 mm^2 respectively. The results showed that the FRP reinforcement improved the load carrying capacity of the deep beam ranging between 35 % and 43 %. Higher strength increment was seen in the beam with larger grid bar cross sectional area. FRP reinforcement restrained the propagation of critical diagonal cracks. Thus, higher loads were required to create critical diagonal cracks that penetrate the beam.

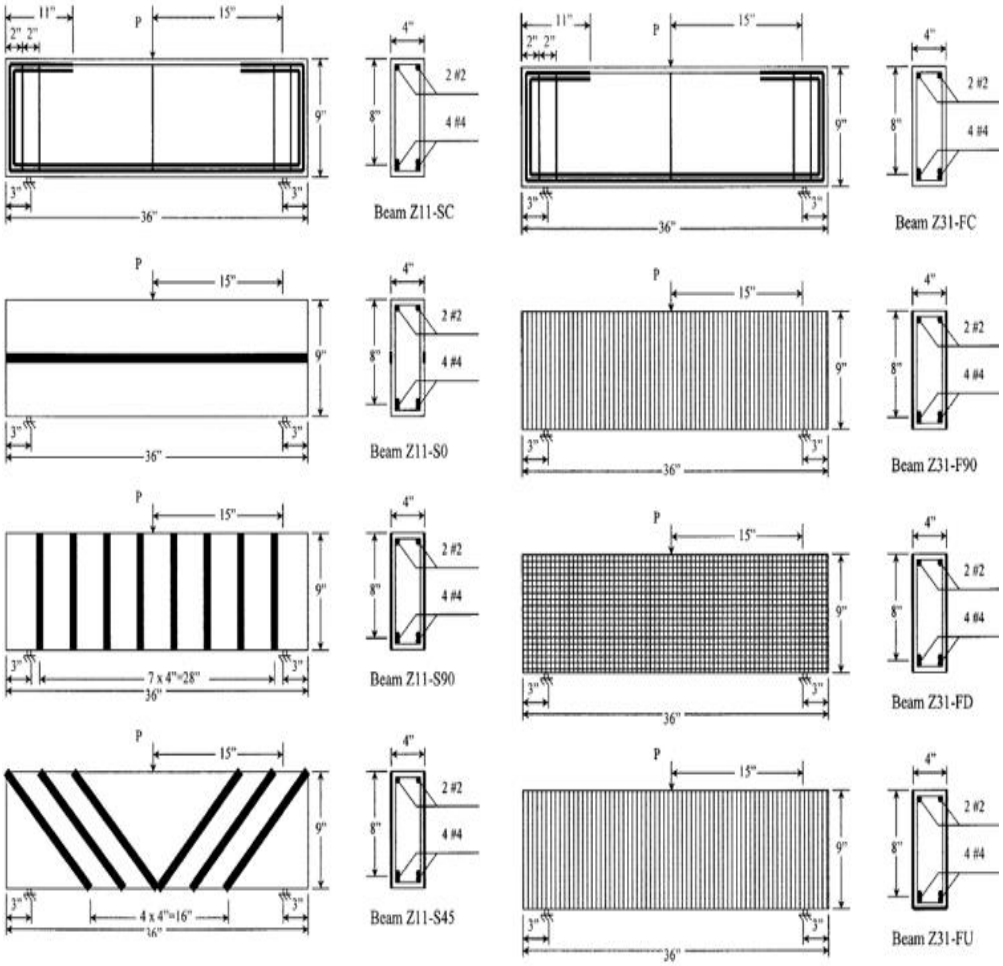

Figure 2.5: CFRP Strips and CFRP Fabrics Detailing (Zhang, et al. 2004).

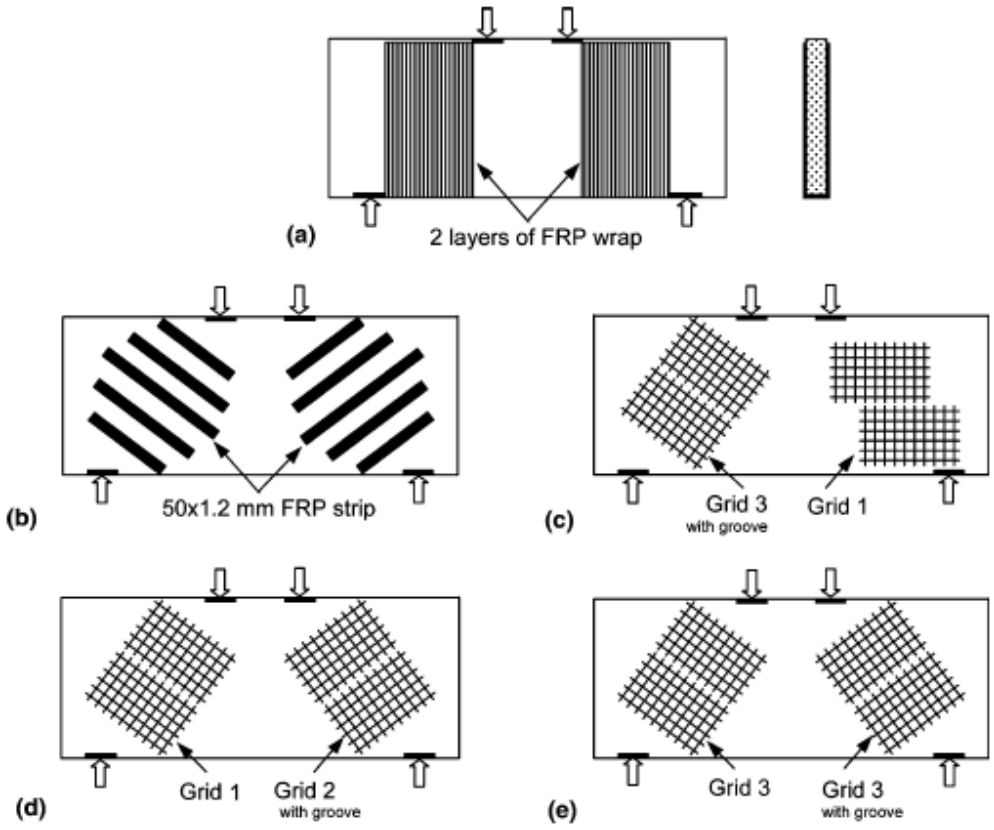

Figure 2.6: Externally Bonded FRP Systems (Islam, et al., 2005).

Maaddawy and Sherif (2009) studied the load carrying capacity of RC deep beam with externally bonded CFRP reinforcement. Four deep beam specimens were wrapped entirely with vertical and horizontal CFRP sheets using epoxy resin, as shown in Figure 2.7. Another nine specimens were conventional deep beams with different opening locations and sizes. As a result, the CFRP reinforcement reinforced deep beam had restrained shear deformation. Therefore, the CFRP reinforcement remarkably increased the beam load carrying capacity, range from 35 % to 73 %. Independent diagonal cracks form in the top and bottom chords of the beams, causing splitting failure and relative rotation of the shear span segments. In contrast, CFRP reinforced beam experienced sudden failure due to the formation of independent diagonal shear cracks along with the concrete disintegration around the top chord wrapped with U-shaped CFRP sheet.

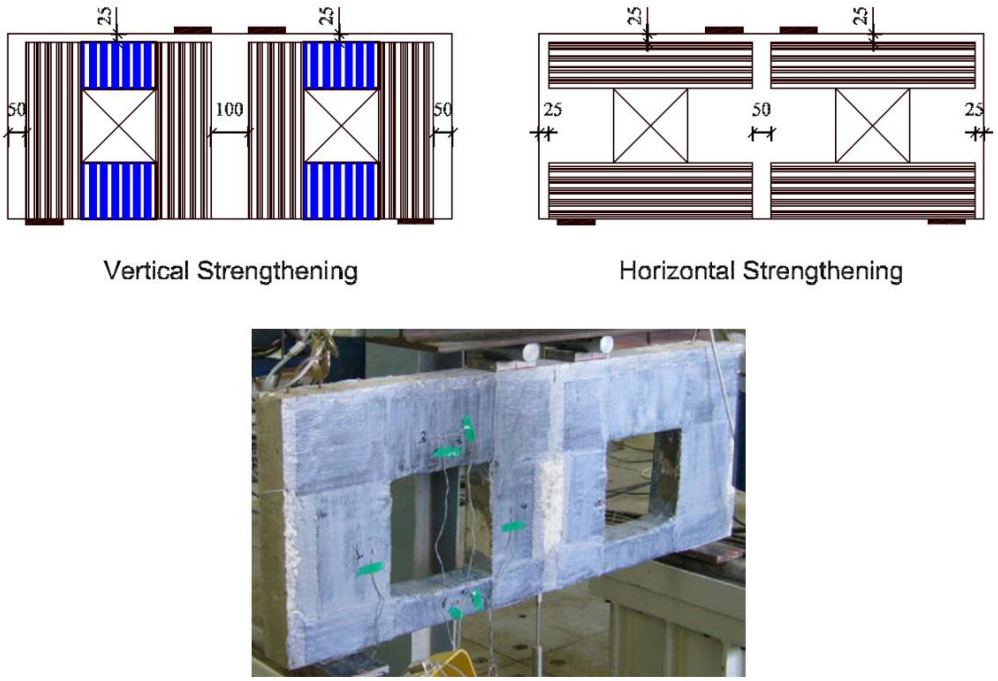

Figure 2.7: Externally Bonded FRP Systems (Maaddawy and Sherif, 2009).

Unlike steel plating systems, the FRP system is non-corrosive. Therefore, it is more durable and sustainable. Moreover, FRP laminates are light, thus easy for transportation. Nevertheless, FRP deep beams were reported to fail in FRP delamination, which is undesirable.

2.2.3 Internal/ Near Surface Mounted (NSM) FRP System

Farghaly and Benmokrane (2013) investigated the behaviour of fiber reinforced polymer (FRP) reinforced RC deep beam without web reinforcement. The primary test variables were the provided longitudinal reinforcement area and the type of reinforcement. The bottom longitudinal steel bars of the deep beam were replaced entirely by carbon fiber reinforced (CFRP) bars and glass fiber reinforced (GFRP) bars with different bar diameters, as shown in Figure 2.8. Different bar diameters represented different longitudinal reinforcement ratios. All the FRP-reinforced deep beams failed by diagonal shear failure, followed by concrete crushing at the top of the compressive strut. The failure mode was regardless of the reinforcement ratio and type. The test results showed that the reinforcement ratio had no effect on the initial flexure and diagonal shear cracking load. However, as the reinforcement ratio increased, the ultimate load carrying capacity of the beam increased significantly. Besides, the GFRP and

CFRP reinforcement decreased the crack width by 43 % and 51 % respectively. Lastly, the absence of web reinforcement had the least effect on the ultimate load but recommended for crack control.

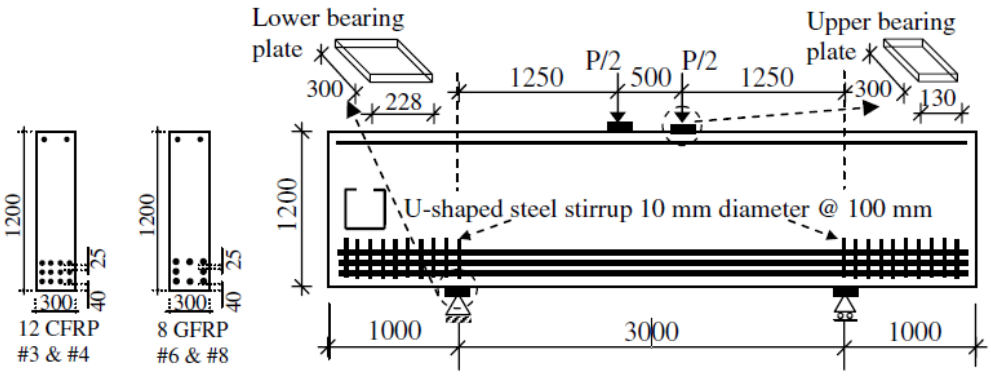

Figure 2.8: Detailing of FRP-reinforced Deep Beam (Farghaly and Benmokrane, 2013).

Albidah, et al. (2019) experimentally and numerically studied the effectiveness of adopted strengthening schemes for RC deep beam. Two types of strengthening schemes were involved: (i) near surface mounted (NSM) CFRP U-wrap strips along with externally bonded horizontal CFRP strips (ii) welded wire mesh (WWM). These schemes were provided only in half span of the beam, while another half span remained as conventional steel web reinforcement, as shown in Figure 2.9. The test observations proved that both strengthening schemes had improved the load carrying capacity of the beam because failure only occurred at the half span with conventional reinforcement, as shown in Figure 2.10. The dominant failure mode was diagonal splitting. The load-deflection curves showed that both schemes improved the stiffness of the beam as well, and the improvements were very similar.

Ibrahim, et al. (2020) studied the load carrying capacity of RC deep beam using near-surface mounted hybrid carbon-glass fiber reinforced polymer strips (NSM-FRP). The NSM-FRP was installed at the left and right surface of the beam, parallel to the steel stirrups. Apart from the number of NSM-FRP, the number of steel stirrups at the critical shear span (CSS) and the configuration of the reinforcement (aligned and unaligned) were investigated as well. The reinforcement configurations are presented in Figure 2.11. This study found that NSM-FRP effectively enhanced the load carrying capacity of the deep beam

ranging between 28.8 % and 55.8 %. Deep beam without CSS stirrup gained greater strength relative to deep beam with CSS stirrup. The unaligned reinforcement configuration gained greater strength due to larger coverage of reinforcement. Other significant enhancements of NSM-FRP reinforced deep beams include increased ultimate deflection, increased energy absorption, and decreased crack width.

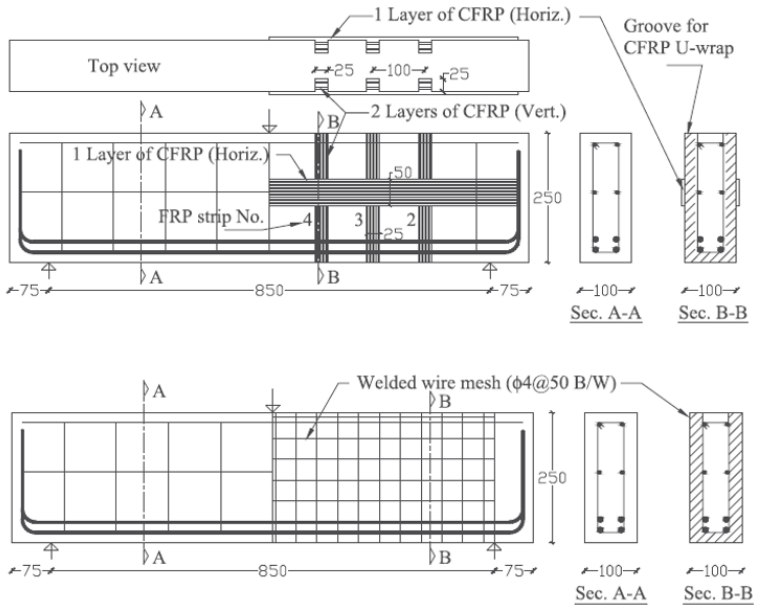

Figure 2.9: FRP and WMM Strengthening Scheme (Albidah, et al., 2019).

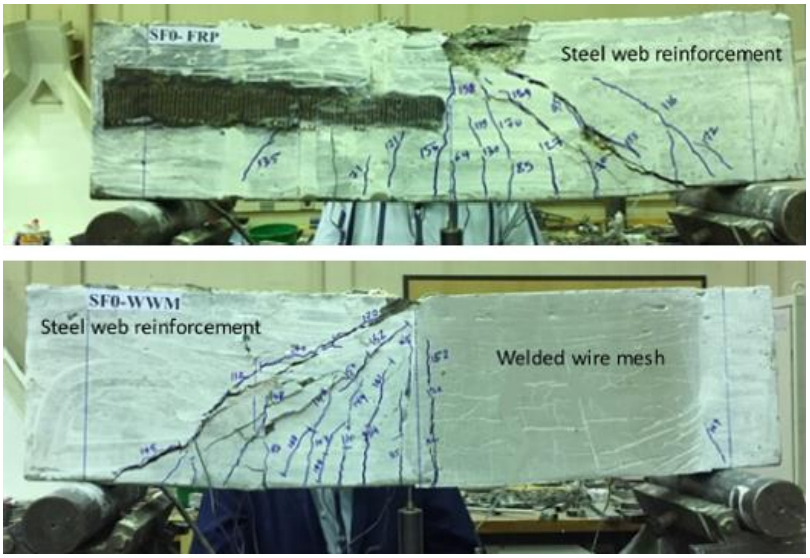

Figure 2.10: Failure of FRP and WMM Deep Beam (Albidah, et al., 2019).

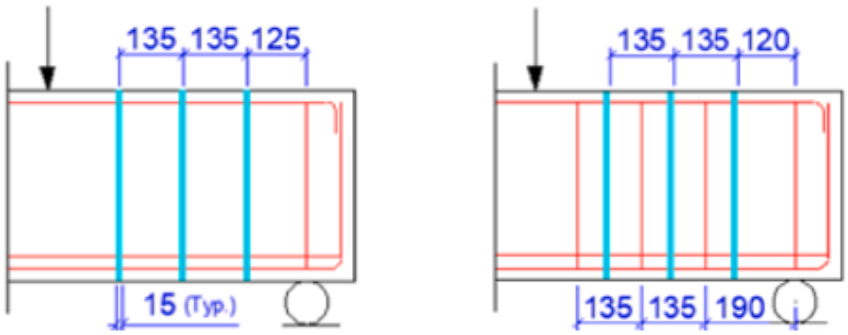

Figure 2.11: Aligned (Left) and Unaligned (Right) Configuration with 3 NSM-FRP and 3 Steel Stirrups (Ibrahim, et al., 2020).

Internal or NSM FRP system could effectively solve the issue of FRP delamination. Most importantly, it boosts the overall performance of RC deep beams. However, these systems involve the rehabilitation and rectification of the existing reinforcement detailing. Therefore, the proposal of novel deep beam shear reinforcement detailing at the design stage remains undiscovered.

2.2.4 Embedded Steel Section

Chen, et al. (2018) tested the behaviour and capacity of steel shape reinforced concrete (SRC) deep beam. Wide flange H-section was embedded into the beam, as shown in Figure 2.12. Softened area is the part located at the exterior of the H-section, where concrete crushes at ultimate state. The deep beam specimens were varied in terms of the H-section dimensions include the section depth, section width, flange thickness, and web thickness. The experimental results showed that the embedded section contributed considerably to the load carrying capacity of the deep beam, up to a maximum value of 5209 kN, which was 200 % of the control beam capacity. Depth of the steel section was the key factor affecting the capacity increment, where deeper section can withstand greater loading. Besides, composite SRC deep beam performed better than non-composite SRC deep beam by 7 % to 23 % in terms of shear capacity. The embedded steel section also provided the deep beam with better ductility than the conventional RC deep beam.

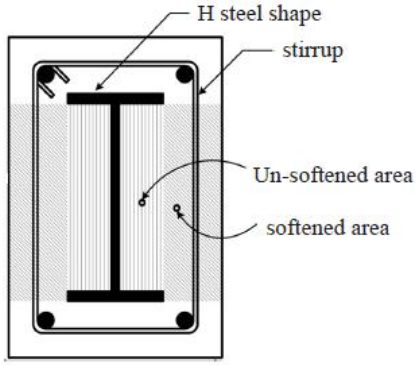

Figure 2.12: SRC Deep Beam Detailing (Chen, et al., 2018).

This method remains the use of conventional shear stirrups. Combining shear stirrups and the steel section may cause reinforcement congestion inside the deep beam. It is difficult for concrete placement and casting, therefore leaving voids inside the concrete and creating concrete honeycombs.

2.3 Reinforcement Methods to Ease Reinforcement Congestion

The simplest yet effective way to improve the performance of a structural member is by increasing the amount of reinforcement used. However, this will lead to another issue, which is reinforcement congestion. Reinforcement congestion causes difficulty in concrete mixing and placement. Moreover, it is difficult for a mechanical vibrator to be placed into the congested reinforcement to ensure the uniformity of the concrete mix. Improper placement and compaction of concrete form honeycomb that deteriorates the load carrying capacity of the structural member. Furthermore, it takes extra time and cost to repair or reconstruct the structure. Therefore, plenty of research was done to identify possible reinforcement methods to ease reinforcement congestion without affecting the overall strength of the structural member.

Kang, et al. (2012) experimentally tested the shear behaviour of steel fiber reinforced lightweight concrete (SFRLC) beams without shear stirrups. The beam specimens were prepared varied in span-to-depth ratio and steel fiber volume fractions. The detailing of the specimen is shown in Figure 2.13. The results proved that the addition of steel fiber in the concrete mix increased the shear capacity by 30 % and improved the ductility as well. Most importantly, it had eliminated the usage of conventional shear stirrups.

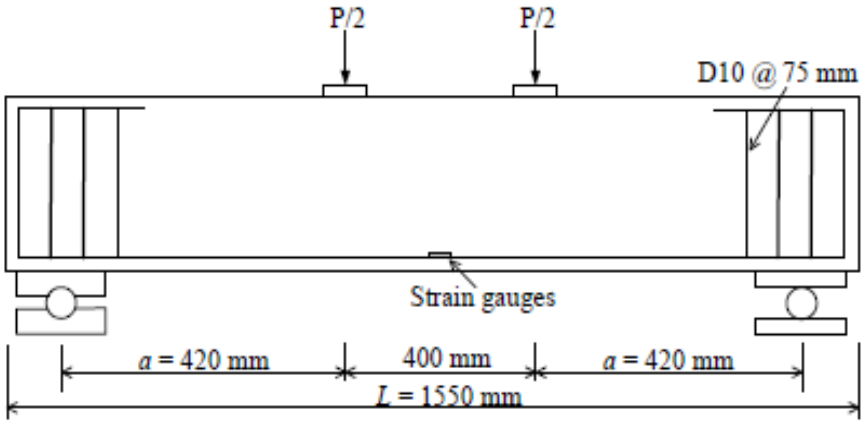

Figure 2.13: SFRLC Beam Detailing (Kang, et al., 2012).

Khai, et al. (2017) tested the effectiveness of bundled diagonal reinforcement in steel-fiber-reinforced concrete (SFRC) coupling beam in seismic action. One control specimen adhered to ACI code-specified reinforcement detailing, while three specimens were reinforced using bundled diagonal reinforcement with different stirrups spacing, as shown in Figure 2.14. All four specimens were made of SFRC. The results proved that bundled diagonal reinforcement enhanced the load carrying capacity of the coupling beam up to 13 % increment as compared to normal arrangement. Furthermore, bundled diagonal reinforcement improved the beam ductility and delayed the stiffness degradation as well. Therefore, it was proven that the application of bundled diagonal reinforcement in SFRC coupling beams considerably reduces the amount of transverse reinforcement required yet improved the seismic performance of the beam.

Kefelegn and Gebre (2020) investigated the structural behaviour of self-compacting concrete (SCC) beams with congested reinforcement. Four SCC beam specimens were prepared, with two vibrated concrete (VC) beams as control. SCC concrete mix of Rank 1 self-compactability was required for high-fluidity concrete to flow into structural members with a minimum clearance of 35-60 mm between the reinforcement. Shear, tension, and compression reinforcement were spaced closely within the range of 35-60 mm to simulate the reinforcement congestion condition, as shown in Figure 2.15. The results showed no significant difference in terms of the crack pattern between SCC and VC beam. However, the load carrying capacity and ductility of the SCC beams were slightly higher than the VC beams.

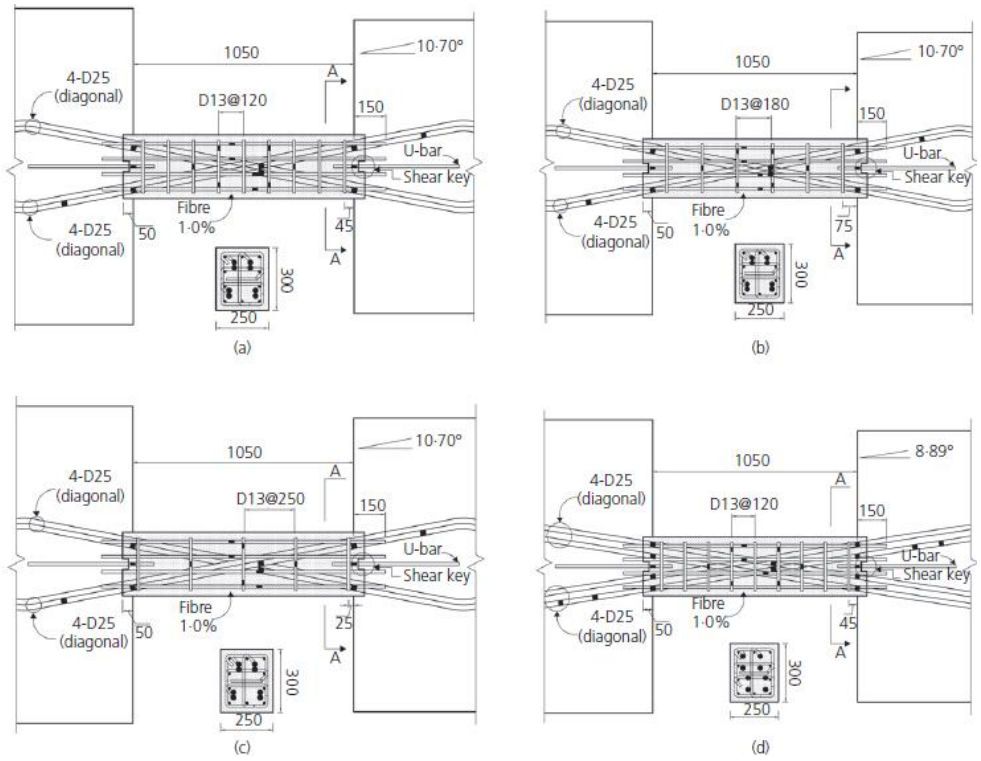

Figure 2.14: Bundle Diagonal Reinforced Coupling Beams (Khai, et al., 2017).

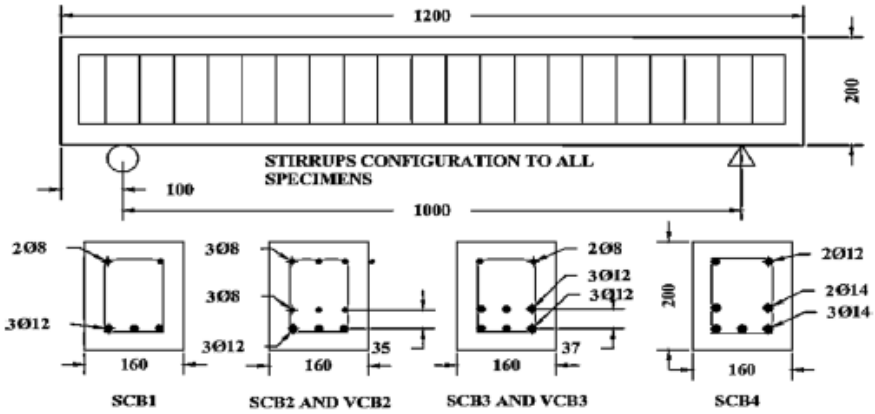

Figure 2.15: SCC and VC Beams Detailing (Kefelegn and Gebre, 2020).

The abovementioned techniques provide remarkable relief to the reinforcement congestion issue in concrete structures and smoothen the casting and placement process. However, these techniques require alteration in the ready-mix concrete proportion, which is very particular, and this may increase the construction cost and time significantly.

2.4 Finite Element Analysis

Finite Element Analysis (FEA) is a computational tool applied in science and engineering to solve complex problems related to structural analysis, thermodynamics, fluid mechanics, electromagnetic potential, etc. FEA divides a complex problem defined by a physical system, such as the Euler-Bernoulli beam equation, into small elements representing different areas in the physical system (Saurabh and Yadav, 2016). Alexander Hrennikoff and Richard Courant first founded FEA in the 1940s. In Hrennikoff's (1941) study on framework analysis, he discovered FEA to resolve the time constraint due to a lack of computation power. Courant (1943) founded FEA with his numerical analysis of the plain torsion problem for multiply connected domains. Both pioneers agreed to one common and essential characteristic of FEA, which is the mesh discretization of a continuous domain into a set of discrete sub-domains.

2.4.1 Structural Finite Element Analysis

Li, et al. (2018) conducted a finite element analysis using OpenSees to investigate the shear behaviour of bolted side plate (BSP) RC beam. The BSP beam was analyzed in terms of the load carrying capacity, crack pattern, and load-deflection behaviour. One beam specimen was tested as the control of the test, while three more specimens were strengthened with side plates of different plate widths, bolt spacings, and the number of bolt rows, as shown in Figure 2.16. Modelling of the concrete, reinforcing bars, steel plates, and bolt connections were completed with multi-layer shell elements, truss elements, flat shell elements, and coupled zero-length elements respectively. The numerical results were validated against experimental results published by Li, et al. (2017). The numerically computed results for the load carrying capacity possessed an error band ranging from 1.8 % to 6.4 % as compared to the experimental results. Besides, the numerical deflection had errors ranging from 4.6 % to 16.2 %. Both the numerical capacity and deflection possessed very little percentage error. Therefore, the numerical model was accurate. In addition, the numerical model predicted the crack pattern accurately, as shown in Figure 2.17. The bolted plates diverted the main diagonal crack into multiple cracks of smaller width. Based on the load-deflection curves presented in Figure 2.18, the numerical

results deviated slightly from the experimental results. However, they followed the same trend, and the curves emerged at a later stage.

Jasim, et al. (2020) conducted finite element analysis on RC deep beam with web openings strengthened externally with carbon fiber reinforced polymer (CFRP) sheets at the left and right surface. This research observed the behaviour of the CFRP reinforced RC deep beam in terms of the failure mode, load carrying capacity, flexural cracking, and the diagonal cracking. Concrete damage plasticity (CDP) model in ABAQUS was implemented to simulate the complex nonlinear behaviour of the concrete. CDP model is preferable in many researches because it considers the degradation in elastic stiffness and strength induced by the tension and compression damages parameter. The numerical results were validated with the experimental results of the CFRP reinforced deep beam tested under two-point symmetric loading, published by Jasim, et al. (2018). The numerical results predicted the occurrence of diagonal splitting failure and shear compression failure, which was in good agreement with the experimental observation, as shown in Figure 2.19. The overall performance of the deep beam was improved as well with the installation of the CFRP reinforcement. However, the stiffness was observed to be higher in the numerical models due to some influences that caused the inaccuracy, as presented in Figure 2.20. Ibrahim and Mahmood (2009) explained that finite element models neglected some potential factors that would reduce the stiffness of the beam, such as micro-cracks due to drying shrinkage and true slip between concrete and steel bonding. Therefore, the numerical stiffness was higher than the experimental value.

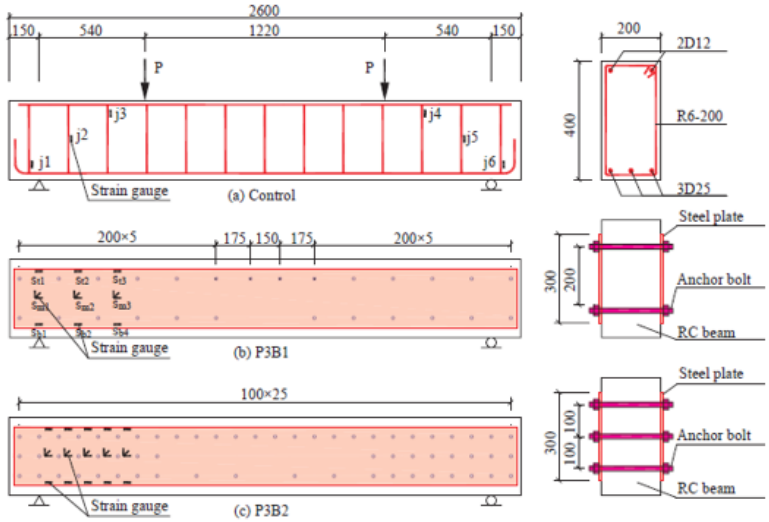

Figure 2.16: BSP Beams Detailing (Li, et al., 2018).

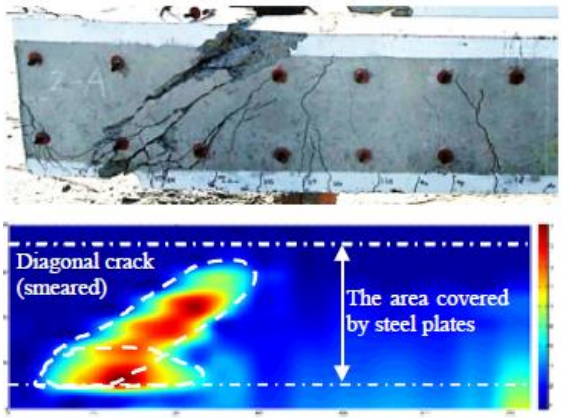

Figure 2.17: Crack Patterns from Experimental Observation and Numerical Analysis (Li, et al., 2018).

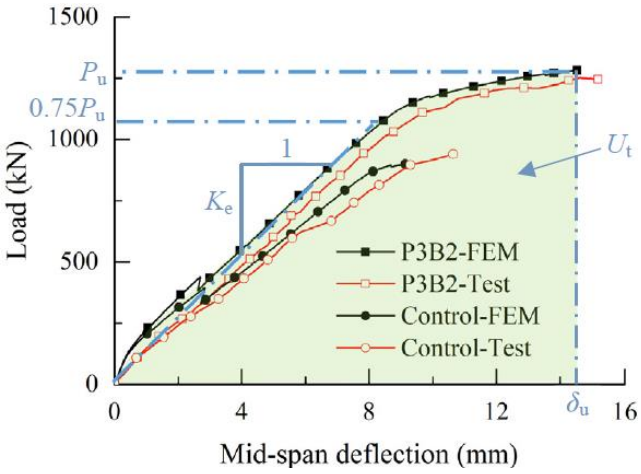

Figure 2.18: Load-deflection Curves of BSP Beam (Li, et al., 2018).

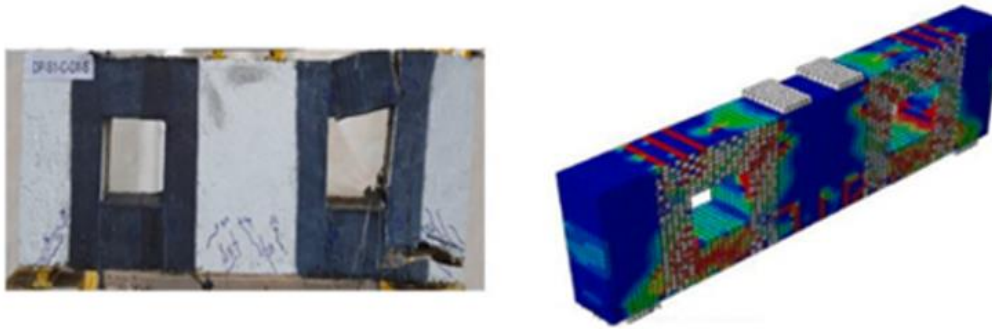

Figure 2.19: Crack Patterns from Experimental Observation and Numerical Analysis (Jasim, et al., 2020).

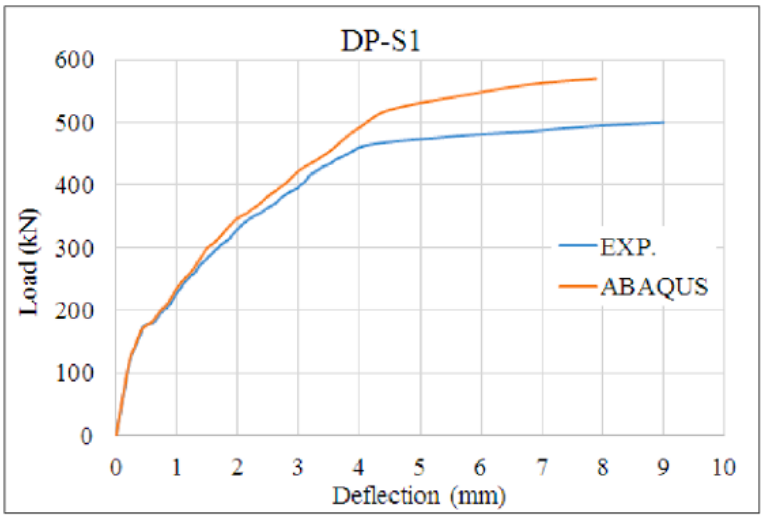

Figure 2.20: Load-deflection Curves of CFRP Beam (Jasim, et al., 2020).

Hawileh, et al. (2012) developed 3D nonlinear finite element models to predict the performance of RC deep beams with web openings strengthened in shear with carbon fiber reinforced polymer (CFRP) composites sheets. Meanwhile, El-Maaddawy and Sherif (2009) published a set of experimental results that proved the shear capacity increment in RC deep beam reinforced with fiber reinforced polymer (FRP) composites around web openings. Hawileh, et al. (2012) validated the numerical results with these experimental results in terms of the load carrying capacity, crack pattern, and deformational characteristics to evaluate the reliability of the finite element models. Six specimens were prepared with different CFRP reinforcement locations, as shown in Figure 2.21. The numerical results were computed using ANSYS ver. 11.0 were proved accurate with only a 3.2 % error band in terms of failure loads prediction and a 14 % error band in terms of deflection capacities prediction.

The results showed CFRP reinforcement around the beam opening had significantly increased the load capacity of the beam. Moreover, the crack pattern projected by the finite element models happened to accord with the experimental observation, as shown in Figure 2.22.

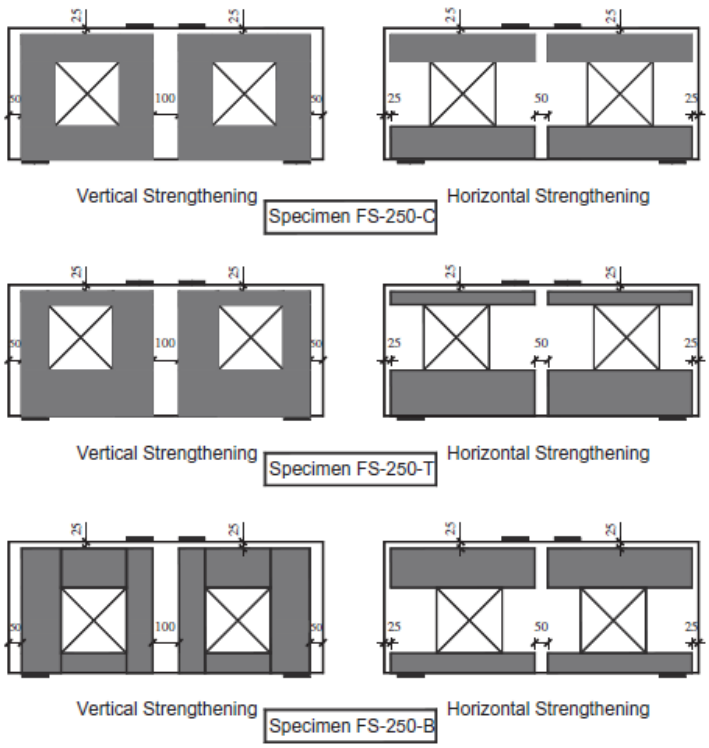

Figure 2.21: Tested Specimens with Various Location of CFRP Reinforcement (Hawileh, et al., 2012).

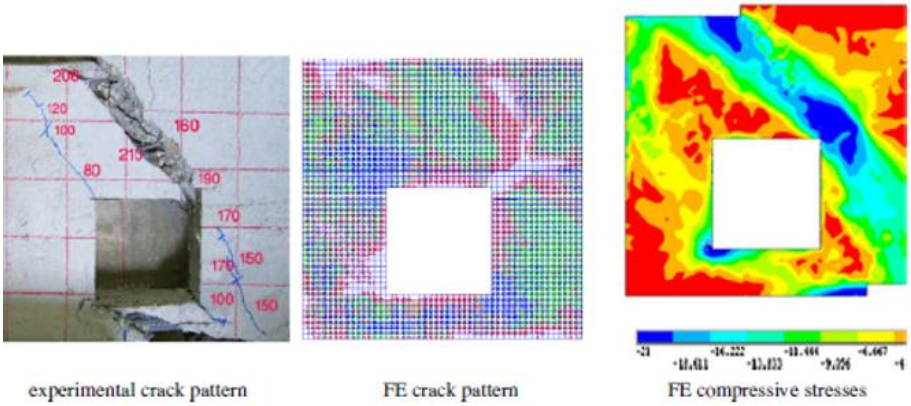

Figure 2.22: Expreimental Crack Patterns and Numerical Principal Compressive Stress (Hawileh, et al., 2012).

Metwally (2015) numerically analyzed the behaviour of RC deep beam reinforced internally with glass fiber reinforced polymer (GFRP) bars using ABAQUS. GFRP-reinforced were used to replace the bottom steel bars, which are prone to corrosion. The reinforcement detailing is shown in Figure 2.23. The numerical models yielded results similar to the experimental results in terms of load-deflection behaviour, failure mode, and crack propagation, as shown in Figure 2.24 and 2.25. Shear compression caused by concrete crushing in the compression zone was the most common failure mode. Metwally (2015) also studied the GFRP bars reinforcement strains that acted as an indicator of the tied arch mechanism inside the beams. The numerical results deviated slightly from the experimental results. However, the values still agreed to a constant trend, where reinforcement strain was higher at the mid-span while lower near the support.

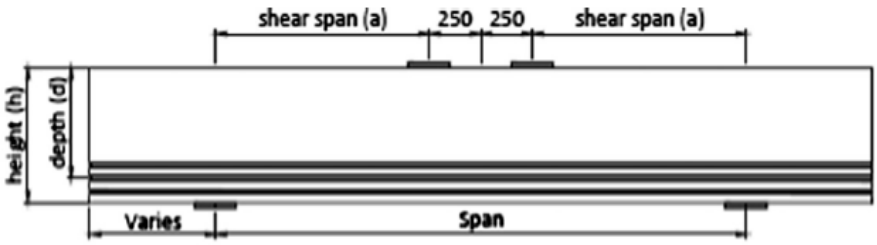

Figure 2.23: GFRP Deep Beam Detailing (Metwally, 2015).

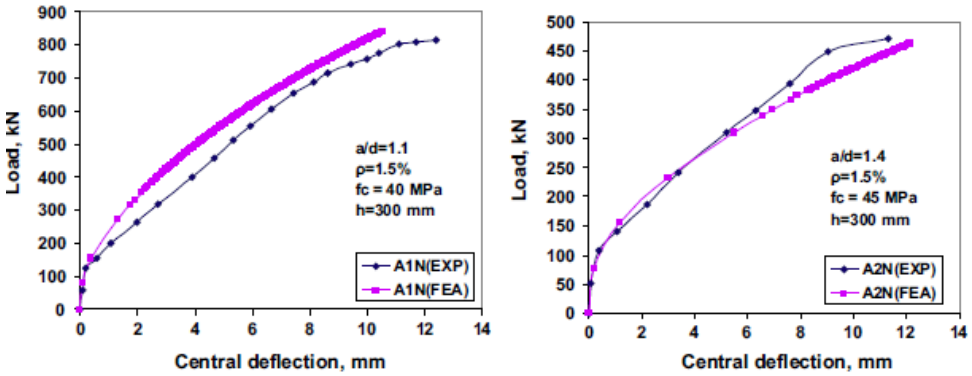

Figure 2.24: Load-deflection Curves of GFRP Deep Beam (Metwally, 2015).

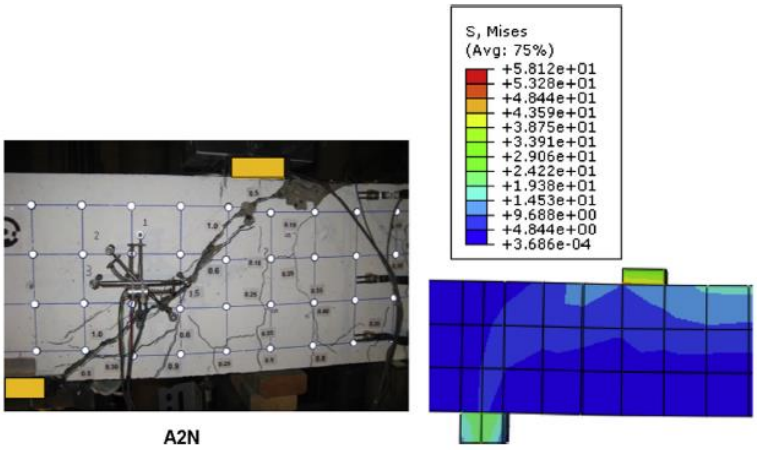

Figure 2.25: Crack Patterns from Experimental Observation and Numerical Analysis (Metwally, 2015).

Ibrahim, et al. (2018) carried out nonlinear finite element analysis to the load carrying capacity and behaviour of deep beam with two proposed internal reinforcement detailing: 1) detailing with embedded struts 2) detailing with intensify ties, as shown in Figure 2.26 and Figure 2.27. Finite element analysis tool implemented in this research was the ABAQUS program to cooperate with the concrete damage plasticity (CDP) model. The reinforcement detailing with embedded struts was more effective when the inclination angle is more than 30˚, where it could withstand 45 % greater von Mises stresses than the intensify ties detailing. The numerical results predicted the capacity of the beam precisely, up to a 99.66 % accuracy. The model projected a crack pattern that matched well with the experimental observation, as shown in Figure 2.28. There was a slight difference in the comparison between load-mid span deflections, which could be explained by the limitations on concrete to deform with damage technique in the ABAQUS program. However, both the numerical and experimental results were showing the same trend.

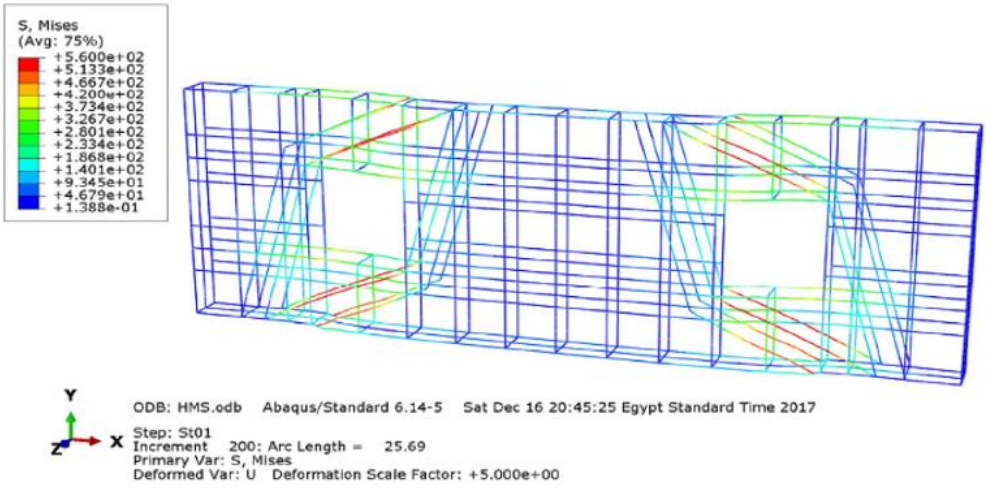

Figure 2.26: Detailing with Embedded Struts (Ibrahim, et al., 2018).

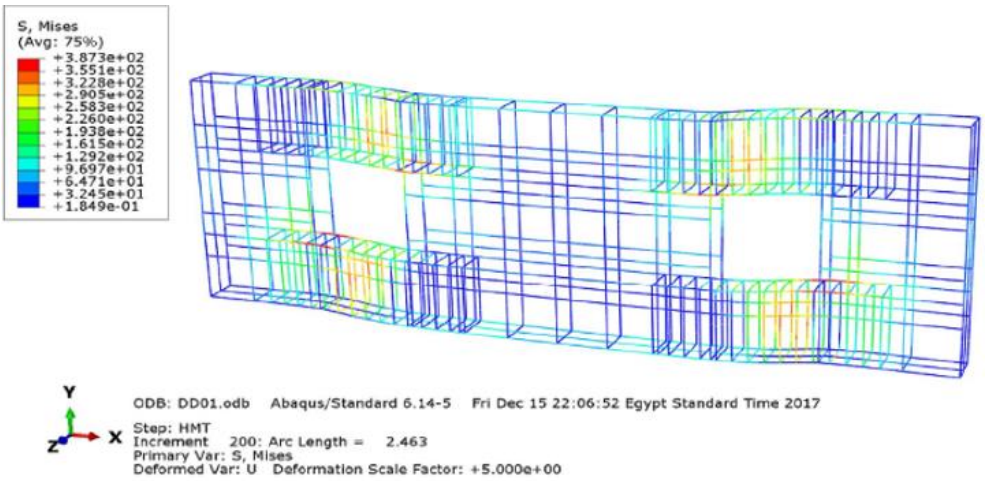

Figure 2.27: Detailing with Intensify Ties (Ibrahim, et al., 2018).

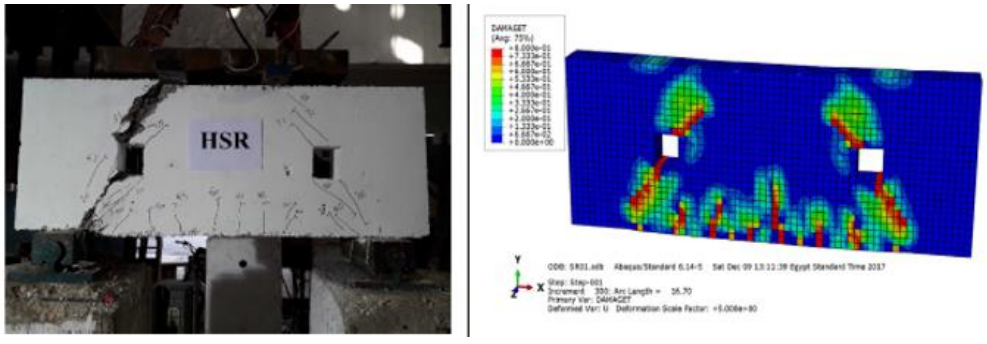

Figure 2.28: Crack Patterns from Experimental Observation and Numerical Analysis (Ibrahim, et al., 2018).

Chiriki and Harsha (2020) studied the behaviour of RC deep beams strengthened internally with I-section and truss reinforcement using ABAQUS software. Five deep beam specimens were prepared and denoted as DB1, DB2, DB3, DB4, and DBWR. DB1 and DB4 had different ratios of conventional shear reinforcement, DB3 had shear reinforcement in the form of truss, DB2 had embedded rolled I-section, and DBWR had no reinforcement. The specimens were analyzed in terms of the load-deflection behaviour and stress capacity. The results showed that the I-section contributed to the highest strength increment, followed by the truss reinforcement, and the conventional shear reinforcement, as shown in Figure 2.29. The shear stress distribution in the deep beams was illustrated with the von Mises contour, as shown in Figure 2.30. Deep beam with embedded I-section and truss reinforcement withheld higher stresses compared to deep beam with conventional shear reinforcement. Deep beam embedded with I-section had the best performance among the four specimens because the bottom flange, top flange, and the web of the I-section were able to withstand a greater amount of tensile stresses, buckling stresses, and shear stresses respectively. In addition, DB1 with a higher conventional shear reinforcement ratio performed better than DB4 with a lower reinforcement ratio in all the testing.

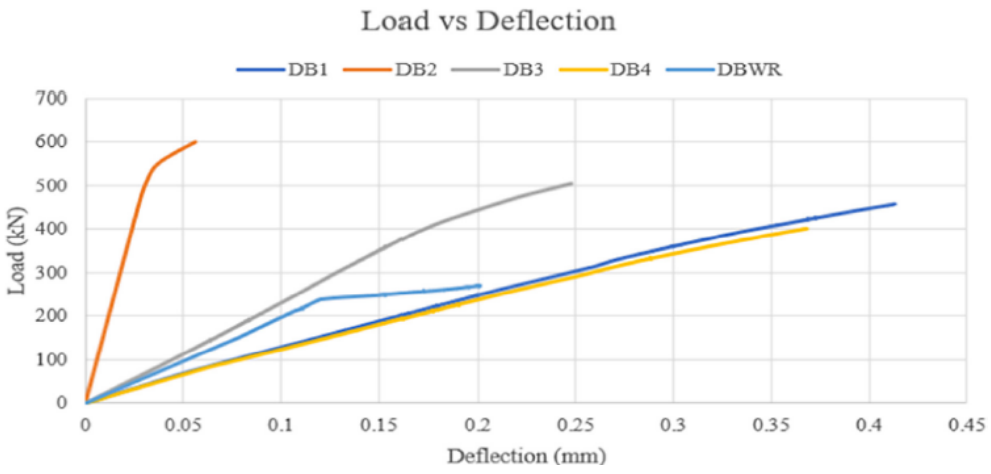

Figure 2.29: Numerical Load-deflection Curve (Chiriki and Harsha, 2020).

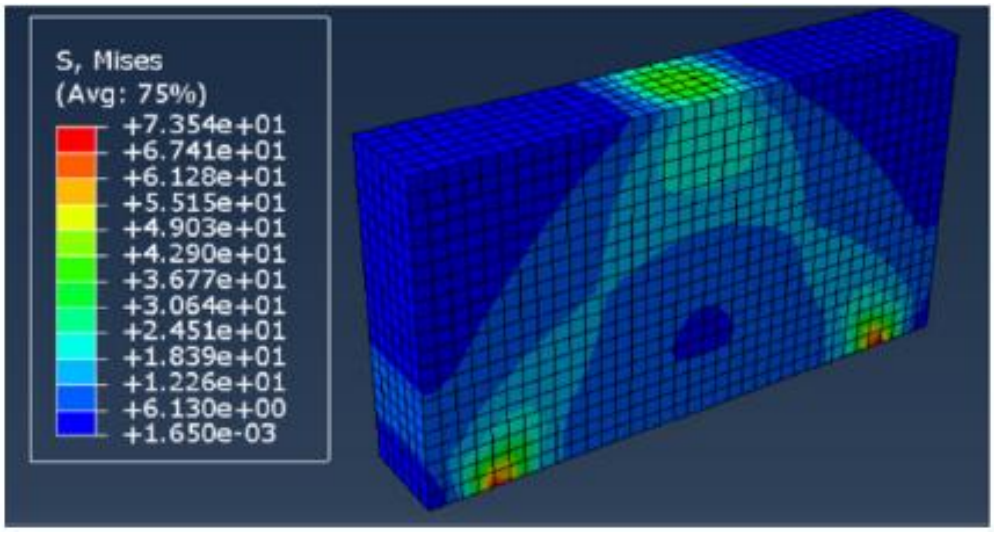

Figure 2.30: Von Mises Stress Contour of DB2 (Chiriki and Harsha, 2020).

Literature has reported on finite element analysis using different computer software such as ABAQUS, ANSYS, and OpenSees to predict the behaviour of RC structures. Besides, the accuracy of these numerical models has been proved by validating the numerical results with experimental publications. The steel-plating system, FRP system, and embedded steel section were numerically analyzed, and the numerical results are reliable. However, the proposed detailing of embedded circular holes thin shear plates need to be investigated further using numerical models in this study.

2.5 Summary

In a nutshell, researchers have established solutions to improve the load carrying capacity, ease reinforcement congestion, and perform numerical analysis on RC structures. External, near-surface mounted and embedded reinforcement systems were effective in increasing the load carrying capacity of RC deep beam (Li, et al., 2017; Ibrahim, et al., 2020; Chen, 2018). Moreover, finite element analysis using computer software generated promising numerical results as compared to the experimental results (Li, et al., 2018; Jasim, et al., 2020). Nevertheless, none of the research conducts a numerical study on the numerical deformation and strength performance of RC deep beam with circular holes thin plates, leaving a research gap that initiated this study.

CHAPTER 3

METHODOLOGY

3.1 Introduction

This study implemented finite element analysis software ABAQUS to develop a numerical model to evaluate the deformation and shear performance of RC deep beam embedded with circular holes thin shear plates. The numerical model was then verified with experimental data to prove the reliability of the model. An optimum design was determined among deep beam specimens reinforced with circular holes thin shear plates of various opening spacing. The optimized design was further investigated with graphics of the numerical results.

Specimen specification and test setup were the foremost pre-process to determine the properties and conditions of the experimental specimens. After that, there were four major stages in this numerical study, including numerical modelling, numerical analysis, results verification, and design optimization.

The first stage was the numerical modelling, which could be further classified into four sub-sections, including material properties modelling, interaction properties modelling, element and mesh size definition, boundary conditions and loading determination. Secondly, numerical analysis was performed in ABAQUS by applying the reference point method. Next, the model was validated by comparing the numerical results with the experimental observations in terms of load-displacement behaviour. Model recalibration is required if the numerical results were inconsistent with the experimental results. Model validation was crucial to avoid errors and increase the results' accuracy. The following stage was the optimization of the spacing between the circular openings to obtain the design that yields the best shear performance. Lastly, the von Mises stress, plastic strain magnitude (PEMAG), and concrete tension damage of the optimized specimen were analyzed and discussed in Chapter 4 for further research purposes.

The general flow of the research methodology is presented in Figure 3.1.

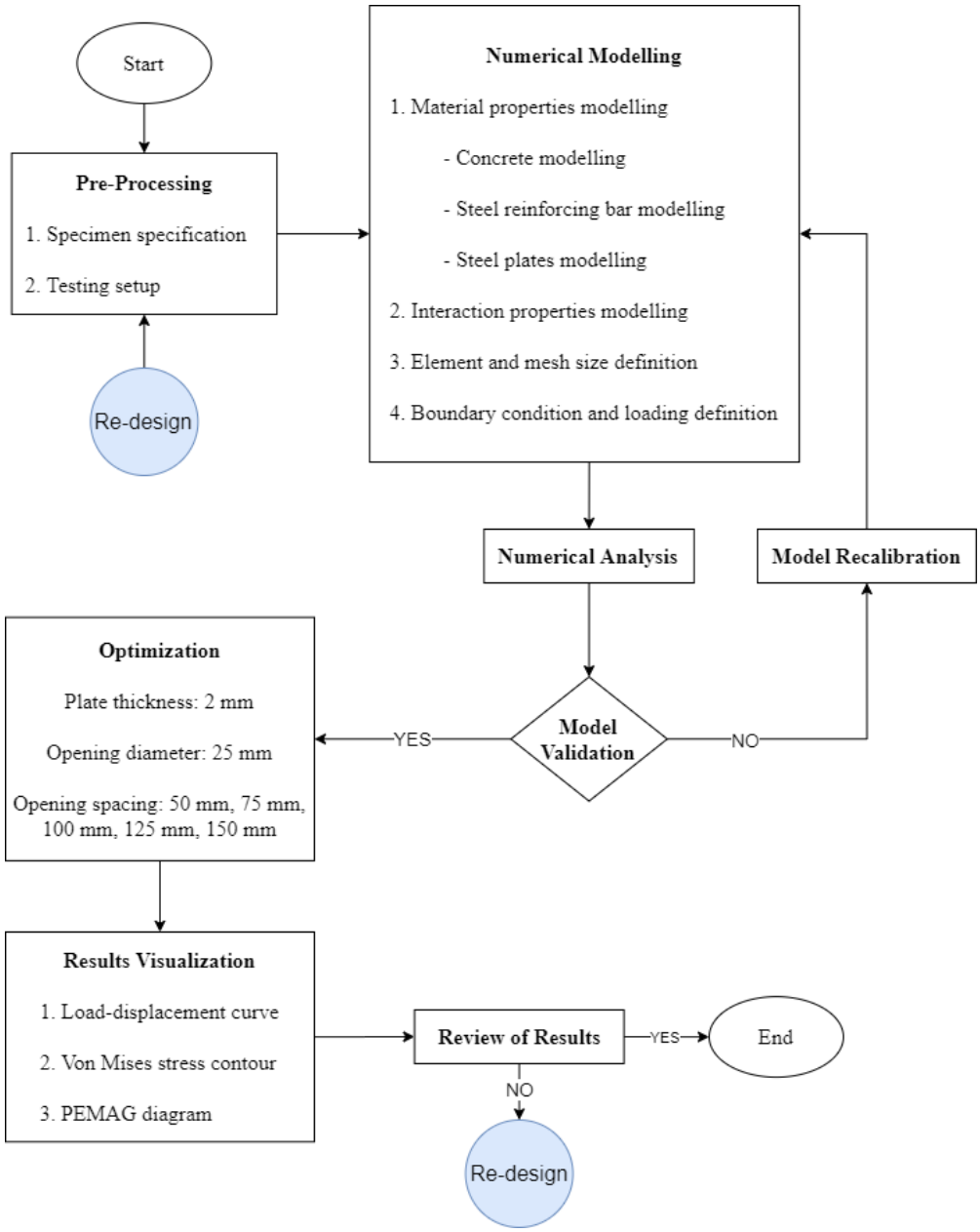

Figure 3.1: General Flow of the Research Methodology.

3.2 Historical Work

Research on deep beam conducted by Jasim, et al. (2020) was used as a reference in this study. Numerical analysis was performed using the reference beam to generate a load-displacement curve. The results were validated with Jasim, et al. (2020) findings to obtain a numerical curve matching the experimental results. Fine-tuning of the material properties and improvement on the simulation technique were performed to improve the compliancy of the numerical results with the experimental results.

3.3 Specimen Specification

Before entering the numerical study, pre-processing works were required to determine the number, physical properties, and reinforcement detailing of the RC deep beams. RC deep beam specimens were divided into three categories: a reference beam, a control beam, and five test specimens.

3.3.1 Reference Beam (Jasim, et al., 2020)

A reference beam was constructed based on the research on deep beam conducted by Jasim, et al. (2020) to validate the numerical modelling technique and the defined material properties. The reference beam was 1500 mm in length, 150 mm in width, and 500 mm in depth, with a clear span to depth ratio of 2.4, which is less than 4.0. Concrete compressive strength provided is 25 MPa. Steel reinforcement provided were 16 mm bottom bar, 6 mm top bar and 6 mm shear link with 90 mm spacing. Besides, T6 steel bars with 86 mm spacing were provided as skin reinforcement at two sides of the beam to limit flexural crack formation. The reference beam geometry and material properties are tabulated in Table 3.1. Figure 3.2 shows the detailing of the reference beam.

Table 3.1: Reference Beam Geometry and Material Properties.

Parameter	**Description**
Annotation	R01
Dimension	1500 mm (length) × 150 mm (width) × 500 mm (depth)
Concrete strength	25 MPa
Flexural reinforcement	2T6 (top), 2T16 (bottom)
Shear reinforcement	T6-90
Skin reinforcement	T6-86

Jasim, et al. (2020) conducted experiment testing on the performance of the RC deep beam and generated results as shown in Figure 3.3 and Figure 3.4. Figure 3.3 shows the load-displacement curve of the experimental reference beam, which served as the main reference for model validation. Figure 3.4 shows the comparison of the failure behavior of the experimental RC deep beam observed experimentally and the numerically simulated stress contour.

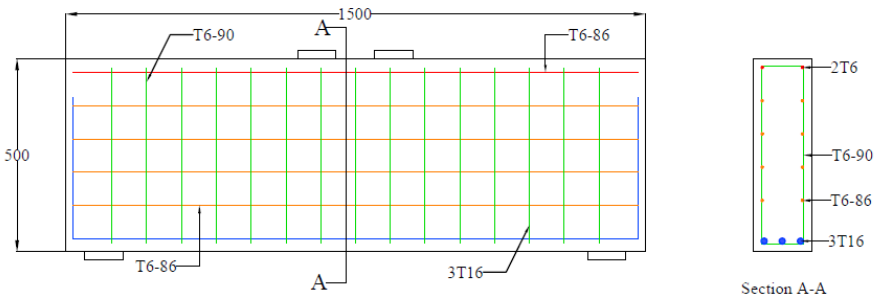

Figure 3.2: Reference Beam Detailing, R01 (Jasim, et al., 2020).

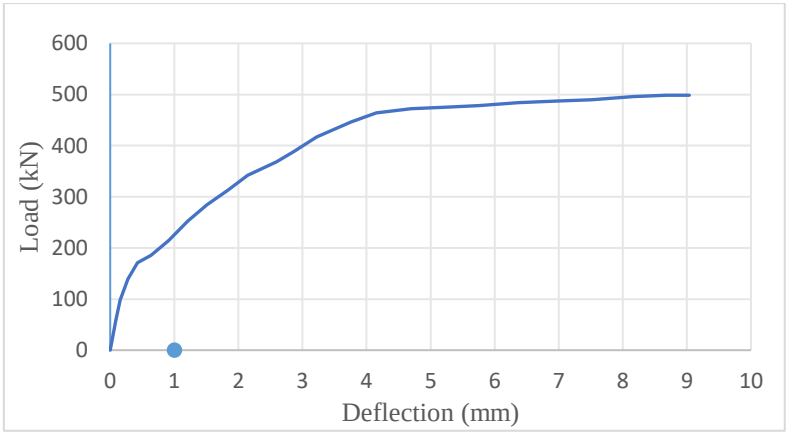

Figure 3.3: Reference Beam Experimental Load-displacement Curve (Jasim, et al. 2020).

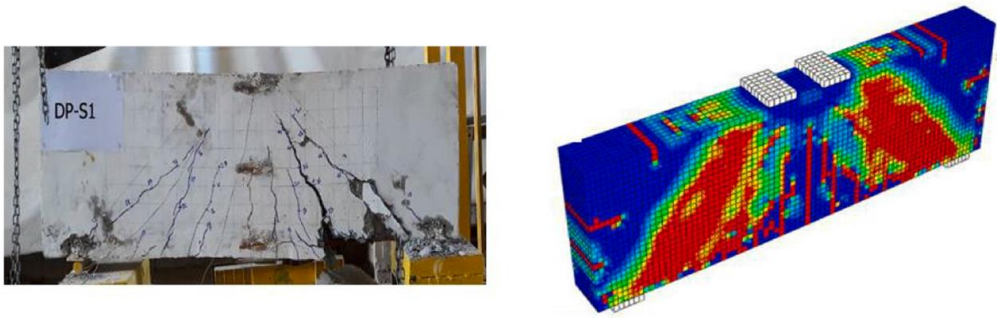

Figure 3.4: Experimental Observation (Left) and Numerical Simulation (Right) of Reference Beam Failure Behaviour (Jasim, et al., 2020).

3.3.2 Control Beam

Control beam noted as C-01 of this study was constructed to examine the performance of RC deep beam reinforced using conventional shear links. The control beam was 1100 mm in length, 150 mm in width, and 275 mm in depth, which had span-to-depth ratio of 4. Concrete casted was Grade C25/30 normal

strength concrete. 12 mm bottom bar was provided as the flexural reinforcement, along with 10 mm top bar. 8 mm shear stirrups with 150 mm spacing were used as the conventional shear reinforcement in the control beam. The control beam geometry and material properties are tabulated in Table 3.2. Figure 3.5 shows the detailing of the control beam.

Table 3.2: Control Beam Geometry and Material Properties.

Parameter	**Description**
Annotation	C01
Dimension	1100 mm (length) × 150 mm (width) × 275 mm (depth)
Concrete strength	25 MPa
Flexural reinforcement	2T10 (top), 2T12 (bottom)
Shear reinforcement	T6-150

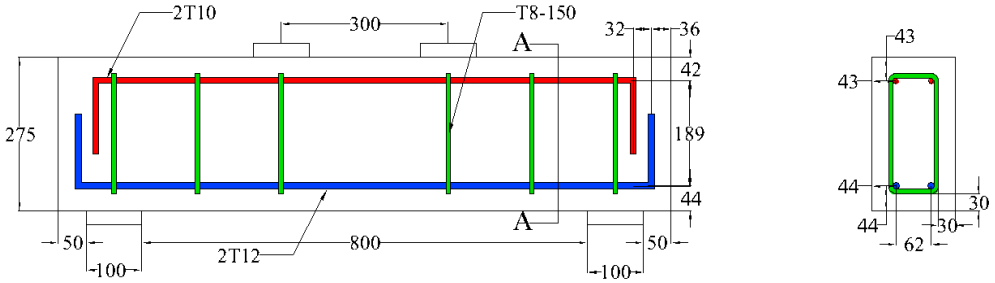

Figure 3.5: Control Beam Detailing, C01.

3.3.3 Test Specimens

Five test specimens were prepared by substituting conventional shear link with 1.5 mm thick circular holes thin shear plates. The shear plates had 25 mm circular holes with different spacing of 50 mm, 75 mm, 100 mm, 125 mm, and 150 mm, as tabulated in Table 3.3. Concrete grade used was Grade C25/30 normal strength concrete. Reinforcement provided were 2T10 top bar, and 2T12 bottom bar, similar to the control beam 1.5 mm thick steel plates were welded at the centre and both ends of the specimen to prevent the disassembling of the reinforcement cage. Figure 3.6 shows the detailing of the test specimens.

Table 3.3: Test Specimens Specification.

Specimen	Description	Remarks
N50	1.5 mm thick plate with equally spaced circular openings.	50 mm spacing, Ø 25 mm opening
N75		75 mm spacing, Ø 25 mm opening
N100		100 mm spacing, Ø 25 mm opening
N125		125 mm spacing, Ø 25 mm opening
N150		150 mm spacing, Ø 25 mm opening

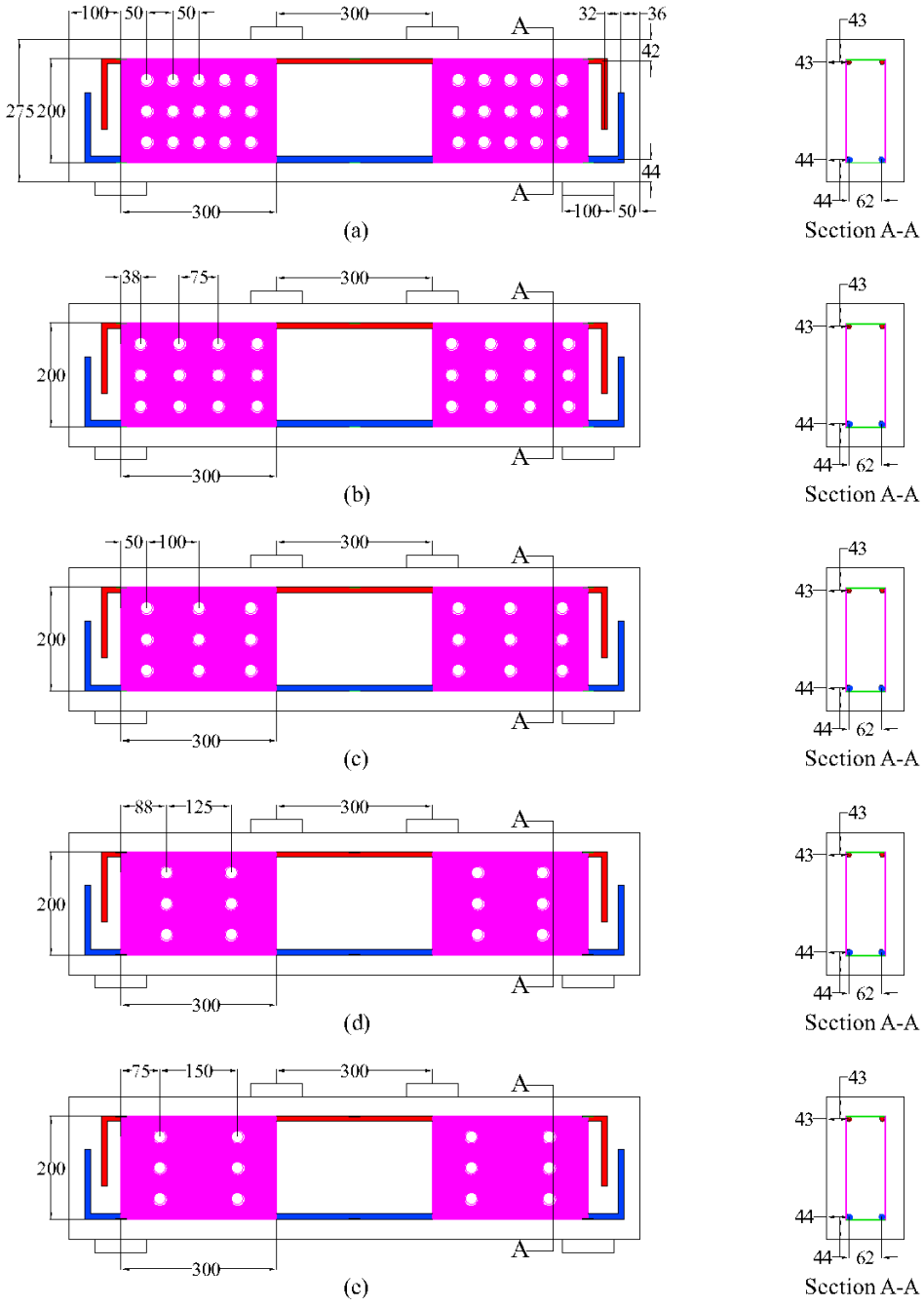

Figure 3.6: Specimen Detailing: (a) N50 (b) N75 (c) N100 (d) N125 (e) N150.

3.4 Numerical Modelling

In this study, nonlinear finite element analysis was conducted using ABAQUS software to study the shear performance of simply supported RC deep beams with circular holes thin shear plate under monotonic loading. ABAQUS provides a series of approaches to representing concrete structure behavior, including the concrete damaged plasticity model, discrete crack model, smeared crack model, and cohesive surface model.

Concrete damaged plasticity (CDP) model was chosen over the other models because it works well to model quasi-brittle structures such as concrete beams, trusses, shells, and solids under monotonic loading. CDP model combines the concepts of isotropic damaged elasticity, isotropic tensile, and compressive plasticity to model the inelastic behaviour of concrete. Viscoplastic regularization is a common technique used in conjunction with the CDP model to overcome the convergence difficulties caused by the softening behaviour and stiffness degradation of the concrete.

Numerical modelling is performed in four stages: material properties modelling, interaction properties modelling, element and mesh size definition, boundary conditions, and loading determination. Material properties modelling determines the properties of concrete, steel reinforcement bar, and steel plate. Interaction properties modelling defines the interactive condition between the reinforcement cage and concrete, and the condition between steel reinforcement bar and steel plate. Element and mesh size definition decide the type of concrete and steel reinforcement element used in the model, and the optimum mesh size to perform finite element analysis. Lastly, all the boundary conditions are added to specify the support condition of the specimens. Two numerical studies of RC deep beam conducted by Demir, et al. (2016) and Ibrahim, et al. (2018) provide guidance in determining necessary parameters in the modelling process.

3.4.1 Material Properties

Material properties modelling inputs the various phenomena observed in the materials into ABAQUS to predict their nonlinear behaviour under desired test conditions. Concrete, steel reinforcing bar, and steel plate are three major components to be modelled in the study of a RC deep beam.

3.4.1.1 Concrete

Concrete parameters of the CBP model include density, characteristic strength of concrete, mean tensile strength, modulus of elasticity, Poisson's ratio, dilation angle, eccentricity, yield stress ratio, ratio of second stress invariant on the tensile meridian, viscosity, and stiffness recovery of the concrete, as tabulated in Table 3.4.

The density of reinforced concrete is 2500 kg/m^3. According to BS EN 1992-1-1:2004 (European Commisssion, 2004), Grade C25/30 concrete has 25 MPa characteristic compressive cylinder strength, and 0.2 Poisson's ratio. Modulus of elasticity of the concrete was calculated as 24569 MPa using Equation (1) by Pauw (1960). The following concrete modelling parameters were obtained from a numerical research by Demir, et al. (2016). The dilation angle is described as the ratio of plastic volumetric strain to plastic shear strain, ranging between 20˚ to 40˚ for concrete. Eccentricity is considered when the loading point is away from the neutral axis of the beam, which was taken as default of 0.1 in this study. The ratio of initial equiaxial compressive yield stress to initial uniaxial compressive yield stress, namely yield stress ratio was taken as the default value of 1.16. The value of the ratio of the second stress invariant on the tensile meridian to that on the compressive meridian was 0.667. The viscosity parameter was 0.0001. It was included in the model to perform viscoplastic regularization that improves the rate of convergence of the model, so more accurate results are generated. For the stiffness recovery parameters, the compression recovery parameter was assumed as 0, while the tension recovery parameter was assumed as 0.8. Zero value of the compression recovery parameter indicates there was no stiffness recovery of the specimen once it failed by crushing in compression.

$$E_c = 0.0736\omega^{1.51}(f_c')^{0.30} \quad (1)$$

where;

f_c = concrete density, kg/m^3

f_c' = comcrete compressive cylinder strength, MPa

Table 3.4: Concrete Parameters of CBP Model (Demir, et al., 2016).

Parameter	**Symbol**	**Value**
Dilation angle	ψ	30˚
Eccentricity	ϵ	0.1
Yield stress ratio	σ_{b0}/σ_{c0}	1.16
Ratio of the second stress invariant on the tensile meridian	K_c	0.667
Viscosity	μ	0.0001
Compression stiffness recovery	ω_c	0
Tensile stiffness recovery	ω_t	0.8

The stress-strain relationship of the concrete due to compression and tension was defined using the stress-strain relationship equation defined in compression and modified tension stiffening model respectively. The stress-strain equations were defined by Carreira and Chu (1985) to define the stress-strain relationship of plain concrete in compression, as shown in Equation (2), and Equation (3). These equations require the input of ultimate strain, which was proposed at 0.002 strain in this study.

$$\beta = \left[\frac{f_c'}{4.7}\right] + 1.55 \quad (2)$$

where;

f_c' = concrete compressive stress, N/mm^2

$$\frac{f_c}{f_c'} = \frac{\beta(\varepsilon/\varepsilon)}{\beta - 1 + (\varepsilon/\varepsilon')^{\beta}} \quad (3)$$

where;

ε = strain, mm/mm

ε' = ultimate strain, mm/mm

For the modelling of stress-strain relationship in tension, Wahalathantri, et al. (2011) modified the proposed model by Nayal and Rasheed (2006) to better fit into ABAQUS software, as shown in Figure 3.7. The modified model created a slanted portion between the critical strain (ε_{cr}, σ_{t0}) to 1.25 critical strain (1.25 ε_{cr}, 0.77 σ_{t0}) to eliminate possible run-time errors in ABAQUS material modelling.

In the calculation of the compression and tension damage parameters, the damage up to the concrete compressive strength was assumed zero. Hence, damage only occurs in the descending limb of the stress-strain curve. Lima, et al. (2016) derived Equation (4) for the compression damage parameter, d_c, and Equation (5) for the tension damage parameter.

$$d_c = 1 - \frac{f_c}{f_c'} \quad (4)$$

where;

f_c = compressive stress on the descending limb, N/mm^2

f_c' = peak compressive stress, N/mm^2

$$d_c = 1 - \frac{\sigma}{\sigma_{t0}} \quad (5)$$

where;

σ = tensile stress on the descending limb, N/mm^2

σ_{t0} = peak tensile stress, N/mm^2

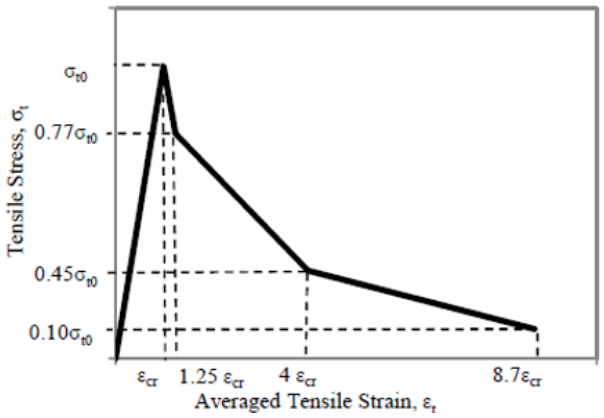

Figure 3.7: Modified Tension Stiffening Model (Wahalatantri, et al., 2011).

Figure 3.8 shows the stress-strain curve of concrete in compression plotted using Carreira and Chu (1985) equations. Figure 3.9 shows the stress-strain curve of concrete in tension plotted based on the modified tension stiffening model by Wahalatantri, et al. (2011). Figure 3.10 and Figure 3.11 show graphs of the concrete compression damage and tension damage respectively.

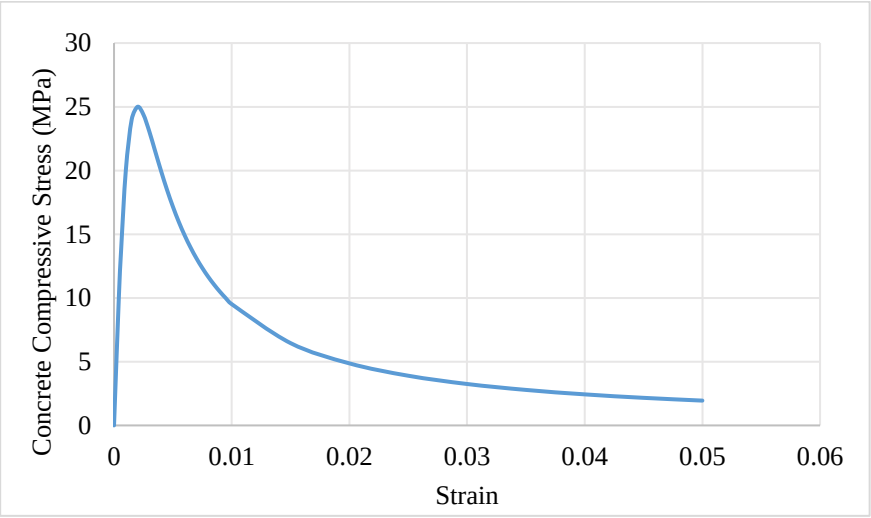

Figure 3.8: Concrete Stress-strain Curve in Compression.

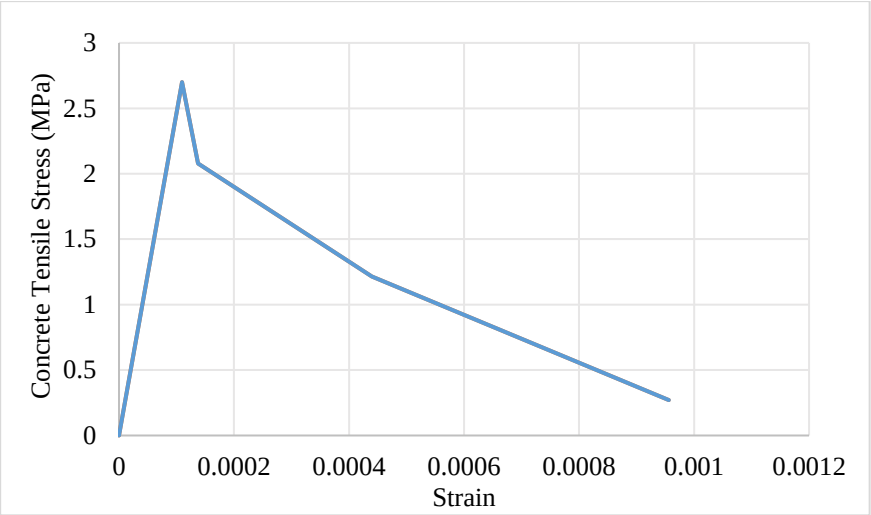

Figure 3.9: Concrete Stress-strain Curve in Tension.

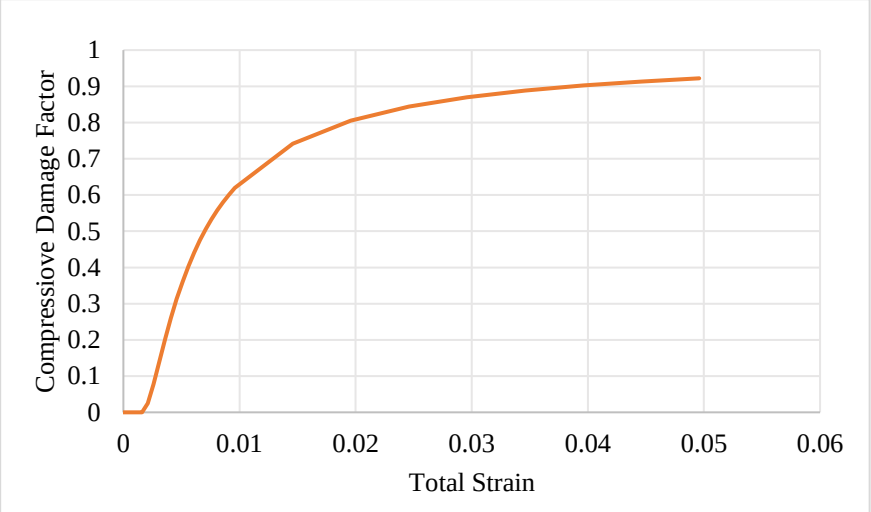

Figure 3.10: Concrete Compression Damage Curve.

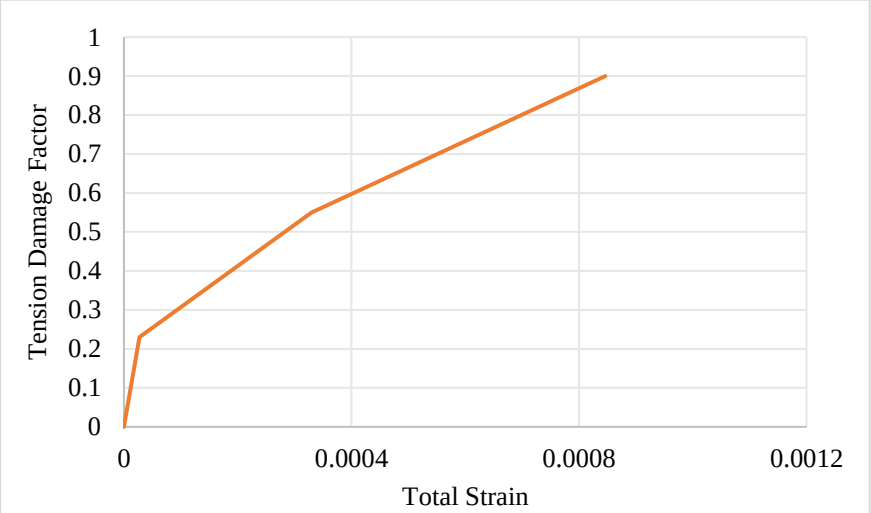

Figure 3.11: Concrete Tension Curve.

3.4.1.2 Steel Reinforcing Bar

Density of the steel reinforcing bar is 7850 kg/m^3. According to BS EN 1993-1-1:2005 (European Commisssion, 2005), structural steels have 0.3 Poisson's ratio in elastic stage. 2T10 mild steel bars were used for top reinforcement, and 2T12 mm steel bars were used for bottom reinforcement. Stress-strain relationship of the steel reinforcing bar could be obtained by conducting a tensile coupon test. However, the test was unable to be conducted due to the Covid-19 pandemic. Therefore, the stress-strain relationship of the reinforcing steel bar was modelled based on the tensile coupon test results by Terng (2019), as shown in Figure 3.12. Furthermore, the results are tabulated in Table 3.5.

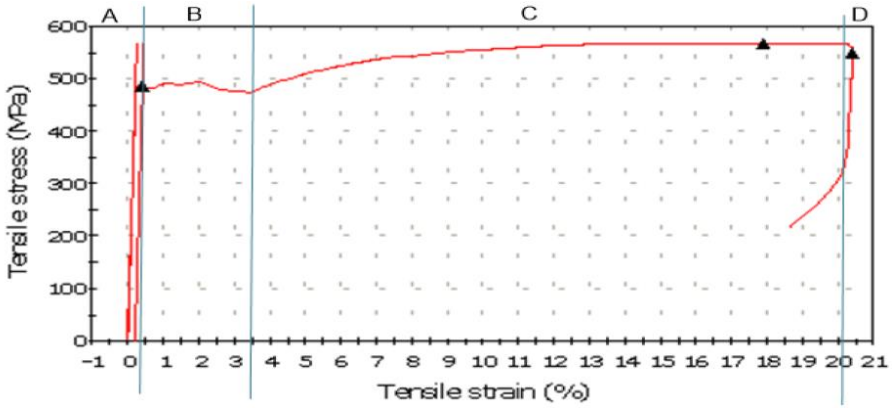

Figure 3.12: Stress-strain Relationship of Steel Reinforcing Bar (Terng, 2019).

Table 3.5: Steel Reinforcing Bar Parameters (Terng, 2019).

Parameter	**Symbol**	**Value**
Elastic Modulus (MPa)	E	214980.30
Yield Stress (MPa)	σ	485.33
Yield Strain (με)	ε	2258
Ultimate Stress (MPa)	f_{yk}	568.25

3.4.1.3 Steel Plate

An 1.5 mm thick steel plates that replaced the conventional shear links have characteristic tensile strength of 500 MPa. The spacing of the openings varied between 50 mm to 150 mm. The stress-strain relationship of steel plates should be tested by tensile coupon test, where only one steel plate, namely the coupon was tested to minimize material wastage. Likewise, the stress-strain relationship

of steel plates were obtained from the literature by Terng (2019), as shown in Figure 3.13, and the results are tabulated in Table 3.6.

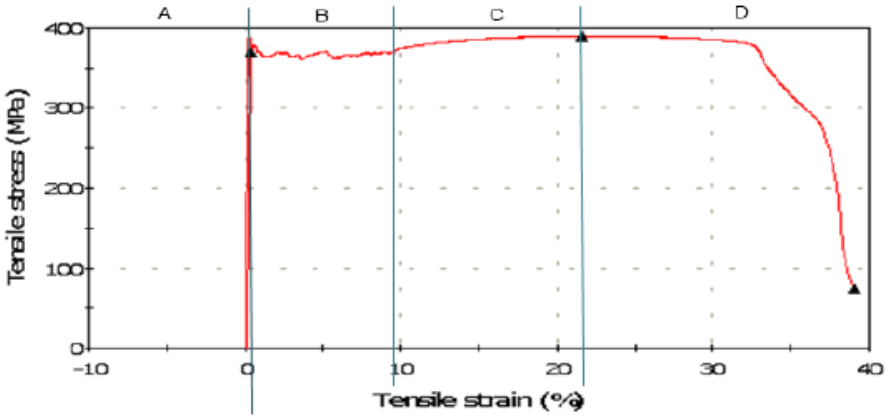

Figure 3.13: Stress-strain Relationship of Steel Plate (Terng, 2019).

Table 3.6: Steel Plate Parameters (Terng, 2019).

Parameter	**Symbol**	**Value**
Elastic Modulus (MPa)	E	178591.97
Yield Stress (MPa)	σ	369.61
Yield Strain (με)	ε	2070
Ultimate Stress (MPa)	f_{yk}	389.69

3.4.2 Interaction Properties

The interaction between the steel plates and steel reinforcing bars was defined using the surface-based tie constraint in ABAQUS. Steel plates with higher stiffness were defined as the master surface, while nodes steel reinforcing bars with lower stiffness were defined as the slave surface. Nodes between the shared surface are eliminated from the master surface to allow multiple slave nodes on the steel bars to tie on a common master surface. Displacement degrees of freedom of the shared nodes were constarained when the steel bars were tied to the steel plates as a solid element, as shown in Figure 3.14 (Dassault Systèmes Simulia Corp., 2017).

Interaction between the steel reinforcement cage and the concrete was specified using the embedded element technique. Concrete, as a three-dimensional solid continuum element, was defined as the host element, and the steel reinforcement cage was embedded in the concrete, as shown in Figure 3.15.

This technique eliminated the initial pore pressure degree of freedom and translational degrees of freedom of the embedded elements and constrained them to the interpolated values of the respective degrees of freedom of the host element. Only rotational degrees of freedom remained initial in the embedded element (Dassault Systèmes Simulia Corp., 2017).

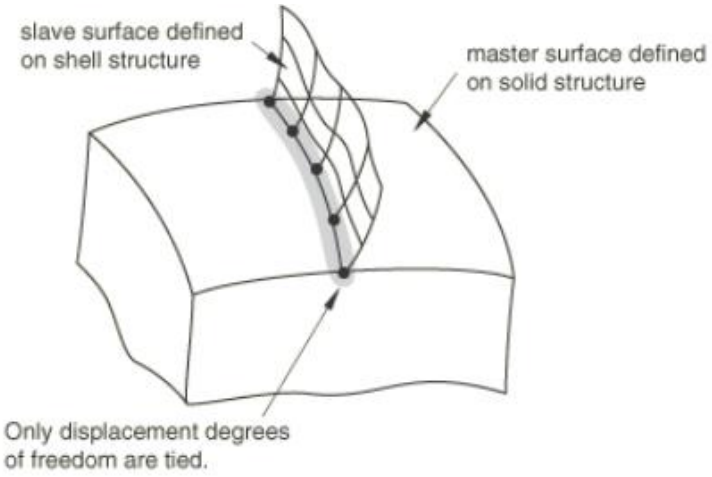

Figure 3.14: Surface-based Tie Constraint on Solid Surface (Dassault Systèmes Simulia Corp., 2017).

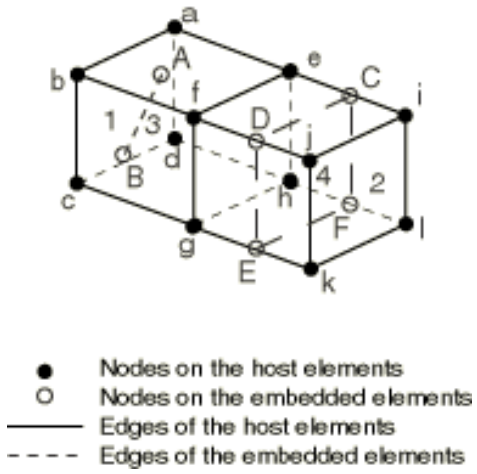

Figure 3.15: Embedded Elements (Dassault Systèmes Simulia Corp., 2017).

3.4.3 Element Type and Mesh Size

Concrete was modelled as a three-dimensional solid continuum element with eight nodes in linear brick pattern, denoted as C3D8R. 'R' indicates that the reduced integration in the element is performed under hourglass control. Hourglassing is a common issue when an unintegrated element produces no

strain and leads to uncontrolled distortion of the mesh. Steel plates were modelled as deformable solid continuum element. Therefore, a similar element type was assigned to the steel plates as C3D8R.

Steel reinforcing bar was stimulated as a 2-node three-dimensional truss element, denoted as T3D2. Truss element is often used to model slender, wired structures such as reinforcement bars that support loading along the axis or centreline of the structure. 2-node straight truss elements linearly interpolate the displacement and position and yield constant stress distribution.

This study used 25 mm mesh size because the coarse aggregate size in the concrete mix is between the range of 20 mm and 25 mm. Hence, 25 mm mesh was optimum to yield converging and accurate results, yet could be done in an acceptable time range.

3.4.4 Boundary Conditions and Load Definition

Support condition of the specimen was roller support. The beam ends were restrained in two degrees of freedom, which are the translation perpendicular to the roller in the 2-direction (U2) and the 3-direction (U3), as shown in Figure 3.16. Translation parallel to the roller and rotation remained unrestrained. Reference points were created at the specimen ends to apply the boundary conditions.

Two-point monotonic loadings with 200 kN magnitude were applied to the loading plates located at the beam centre. Reference points were created to stimulate the loading points. MPC constraint interaction was created between the reference point, as the control point and the centreline of the loading plate that contains the slave nodes. The purpose of creating MPC constraint was to convert the point load into a line load that was evenly distributed along the plate centreline. Concentrated force loading was applied using a static loading step in the 2-direction (U2). Loading was applied at 1×10^{-5} minimum step increment and 10 maximum increment. The maximum number of increments was 10000 or within 10 s time period.

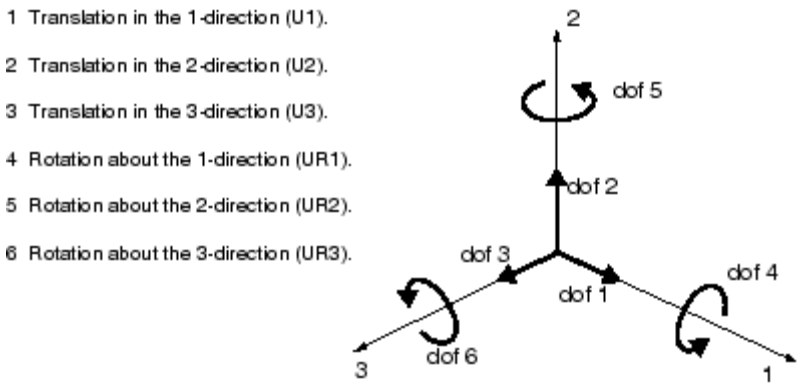

Figure 3.16: Translation and Rotational Degrees of Freedom (Dassault Systèmes Simulia Corp., 2014).

3.5 Results Verification

Numerical results were presented and verified with the experimental results. The main parameter to be verified was the shear bearing capacity based on the load-displacement curve of the specimens. Furthermore, the numerical generated concrete tension damage contour was compared with the experimentally observed crack propagation. Results verification aims to check the compliance of the numerical specimens with the real behaviour of the experimental RC deep beams. Therefore, recalibration is required if the model showed incompliance results. Modifications on the material and mechanical properties of the numerical specimens are performed to recalibrate the model.

3.6 Optimization

The verified numerical model was used to simulate the shear behaviour of RC deep beam specimens reinforced with 1.5 mm thick shear plates of various opening spacing, including 50 mm, 75 mm, 100 mm, 125 mm, and 150 mm.

The main purpose of optimization is to determine the opening spacing that provides similar and reassembles load carrying capacity as the conventional shear link design. Load-displacement curve was the key factor to determine optimum design for the thin shear plates. After that, the optimizated specimen was further investigated in terms of the von Mises stress, plastic strain magnitude (PEMAG), and concrete tension damage. Graphical visualizations were generated to understand better the relationship between the performance of RC deep beam and the opening spacing. The graphics also predicted the

numerical deformation of the specimen throughout the loading process. Moreover, adequately designed detailing could save plenty of time and cost by avoiding unnecessary spending on overdesigned or undersigned detailing.

3.7 Summary

The research methodology consists of four main parts, including numerical modelling, numerical analysis, results verification, and optimization. Numerical modelling defines the material and mechanical properties of the deep beam specimen. Next, numerical analysis generates results and graphics representing the deformation and shear performance of the specimens, thus achieved one of the study objectives. Then, the numerical results are compared with experimental results to complete results verification. Lastly, the verified model is used to determine the optimum design of RC deep beam embedded with circular holes thin shear plates of five different opening spacings.

CHAPTER 4

RESULTS AND DISCUSSIONS

4.1 Introduction

This chapter discusses the results of a reference beam, a control beam, and test specimens stimulated by ABAQUS finite element software. Five test specimens strengthen with 1.5 mm circular hole steel plates with different spacing were numerically tested under monotonic point loads. The results are analyzed in terms of the load-displacement behaviour, von Mises stress contour, plastic strain magnitude (PEMAG), and concrete tension damage.

The discussion starts with a validation of the simulation technique and material properties with a comparison between the numerical results of the reference specimen, R01 and the experimental results by Jasim, et al. (2020). Test results of a control beam, C01 and five test specimens, N50, N75, N100, N125, and N150 were generated with the validated model. The results were compared and optimized to obtain a detailing with the best performance.

4.2 Model Validation with Reference Beam

In the first stage of the analysis, the numerical model was validated by comparing the results between the numerical reference beam, R01 and experimental results by Jasim, et al. (2020). R01 was 1500 mm in length, 150 mm in width, and 500 mm in depth. Flexural reinforcement was 2T6 on top, and 2T16 at the bottom. Conventional shear reinforcement provided was T6 with 90 mm spacing, along with skin reinforcement of T6 with 86 mm spacing.

The main purpose of model validation is to verify the ability of the model to numerically simulate the real behaviour of a RC deep beam. The important material parameters to be validated were the viscosity, and the dilation angle of the concrete property, which were 0.005 and 30˚ respectively. Other than that, the interaction between the instances, along with the other numerical settings were tested to check the correctness of the modelling technique. Model validation was done by comparing the load-displacement curve of R01 with Jasim, et al. (2020) experimental results, as shown in Figure 4.1, and the test values are tabulated in Table 4.1.

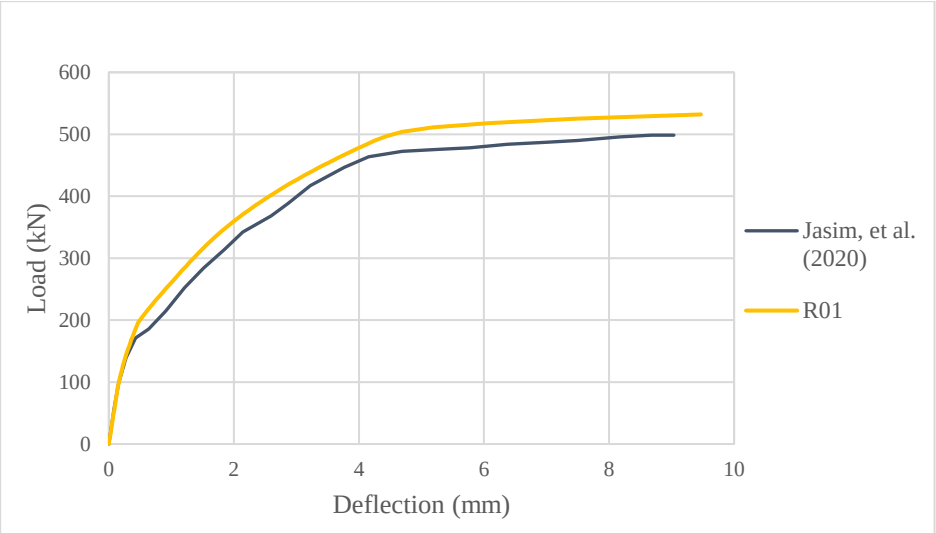

Figure 4.1: Load-displacement Curve of Jasim, et al. (2020) Experimental RC Deep Beam, and Reference Beam, R01.

Table 4.1: Test Results of Jasim, et al. (2020) Experimental RC Deep Beam, and Reference Beam, R01.

Specimen	**Cracking Load (kN)**	**Percentage Difference (%)**	**Yield Strength (kN)**	**Percentage Difference (%)**
Jasim, et al. (2020)	186	-	464	-
R01	200	7.53	504	8.62

Based on Figure 4.1, the cracking of R01 started when the loading reached 200 kN at 0.49 mm deflection, while the first crack of the experiment specimen developed when the loading reached 186 kN at 0.64 mm deflection. Furthermore, the yield strength of R01 is 504 kN at 4.69 mm deflection, while the yield strength of the experimental specimen is 464 kN at 4.15 mm deflection. The yield strength of numerical specimen, R01 is 8.62 % higher than the experimental specimen. It can be concluded that the numerical specimen is having a higher stiffness than the experimental specimen. This increment could be caused by the assumption of the fully embedded interaction between the steel reinforcement and concrete, thereby overestimating the stiffness of the beam (Kachlakev, et al., 2001). In addition, the numerical model did not include microcracks that are likely to develop in the concrete due to drying shrinkage (Ibrahim and Mahmood, 2009).

Apart from comparing the strengths, the numerical concrete tension damage was verified with the experimental cracking of the reference beam. Figure 4.2 shows the experimental cracking of Jasim, et al. (2020) reference beam. Figure 4.3 presents the concrete tension damage contour of R01 that predicted the crack pattern numerically. Both figures clearly illustrate severe cracks at the diagonal concrete strut originated from the supports and propagated towards the loading points. Besides, several vertical cracks developed in the midspan tension region. The numerical deformations of R01 appear to match well with the experimental cracking, thereby proving the ability of the numerical model in crack pattern simulation.

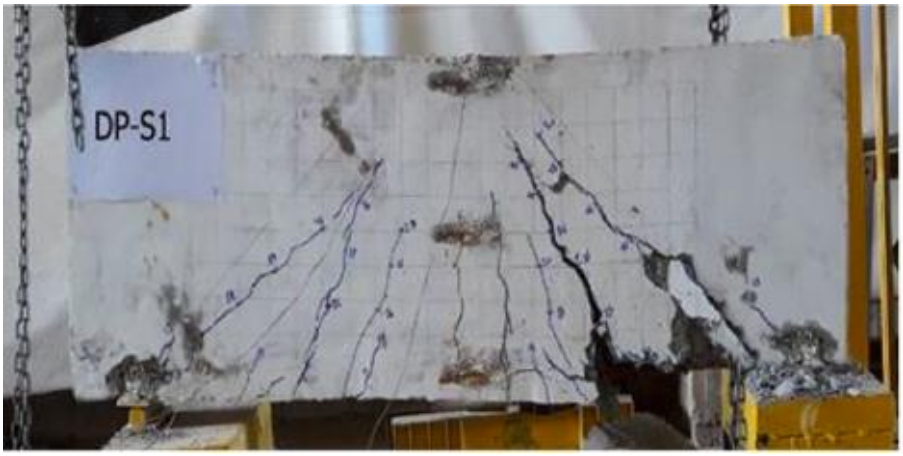

Figure 4.2: Experimental Cracking (Jasim, et al., 2020).

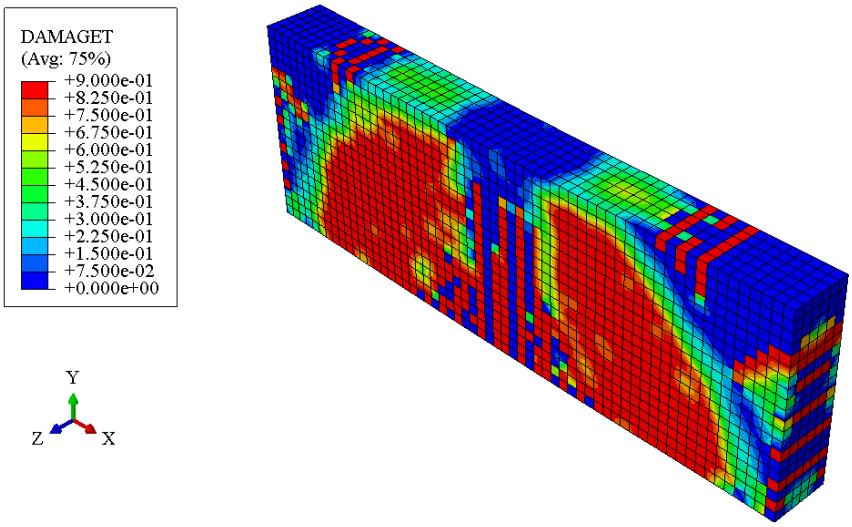

Figure 4.3: Tension Damage Contour of R01.

In short, the numerical specimen, R01 is slightly stiffer than the experimental specimen. However, the load-displacement behaviour of R01 reassembles well with the trend of the experimental results. Besides, the numerical deformations of R01 is in good agreement with the experimental observations. Therefore, the material properties and modelling technique implemented in this study are proven accurate. The developed numerical model is concluded to be reliable in modelling the following test specimens reinforced with circular holes thin shear plates, thereby achieving the study objectives.

4.3 Control Beam with Conventional Shear Link

The verified model was used to analyze the control beam, C01 reinforced with conventional shear links. C01 was 1100 mm in depth, 150 mm in width, and 275 mm in depth. Flexural reinforcement provided was 2T8 top bar, and 2T12 bottom bar. Conventional T8 shear link reinforcement was provided in vertical arrangement and 150 mm spacing. Load-displacement curve of C01 was generated to determine the cracking load and the yield strength of the beam. Figure 4.4 illustrates the load-displacement curve of C01.

Based on Figure 4.4, the load-displacement curve of C01 has the steepest slope at the early elastic region until the first crack developed at 72 kN and 0.49 mm deflection. The curve continues with a linear elastic region until it reaches the yield point at 176 kN and 2.61 mm. After yielding, the curve grows steadily until it reaches the ultimate stress at 200 kN and 9.19 mm deflection.

Load-displacement curve of the control beam, C01 is in good agreement with the behaviour of the reference and experimental specimen. Therefore, the numerical model of C01 was proven to be a reliable control model in the study of the performance of the test specimens strengthened with circular holes thin shear plates.

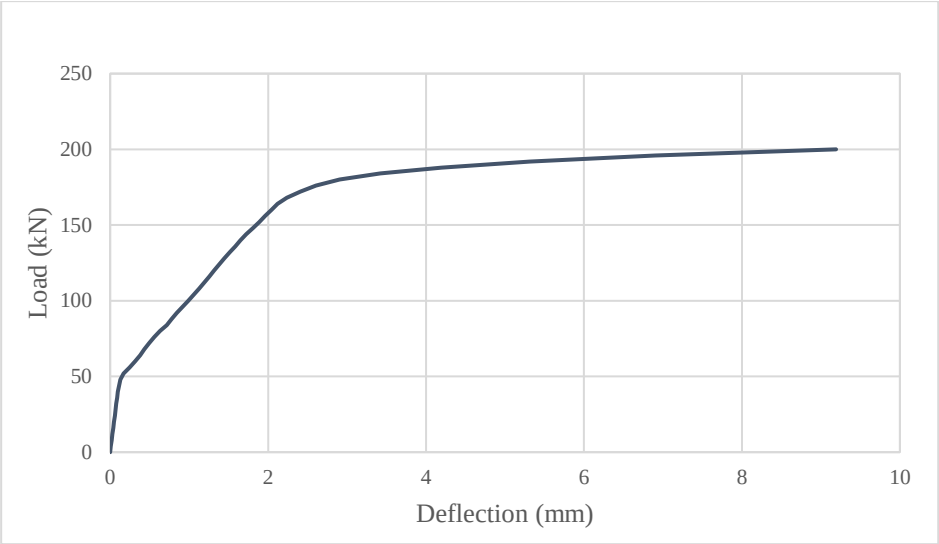

Figure 4.4: Load-displacement Curve of Control Beam, C01.

4.4 Test Specimens with Circular Holes Thin Shear Plates

Test specimens reinforced using 1.5 mm circular holes thin shear plates instead of conventional shear link were studied. The test was carried out under monotonic loading and simply supported condition. In order to determine the optimum design of the shear plates on the deep beam's capacity, five different holes spacing were considered, including 50 mm, 75 mm, 100 mm, 125 mm, and 150 mm, and were denoted as N50, N75, N100, N125, and N150 respectively. In the midst of the Covid-19 pandemic, this study was facing difficulty to obtain the experimental results from laboratory test. Therefore, the results were analyzed using the numerical results of the control beam and the test specimens.

4.4.1 Load-displacement Curve

Figure 4.5, Figure 4.6, Figure 4.7, Figure 4.8, and Figure 4.9 illustrate the load-displacement curve of the respective numerical test specimen compared with the control beam. Figure 4.10 and Figure 4.11 are the enlarged view at the yield point and fracture zone respectively, to obtain more accurate values for the yield strength and ultimate strength. Table 4.2 tabulates the shear reinforcement area, yield strength, ultimate strength, maximum deflection, and the percentage difference of the values as compared to the control beam.

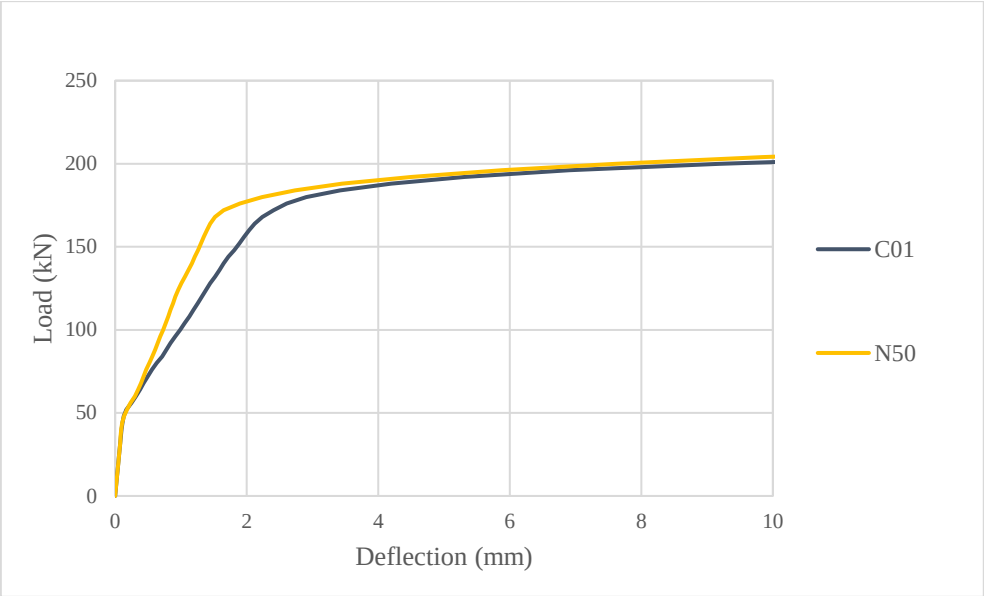

Figure 4.5: Load-displacement Curve of C01 and N50.

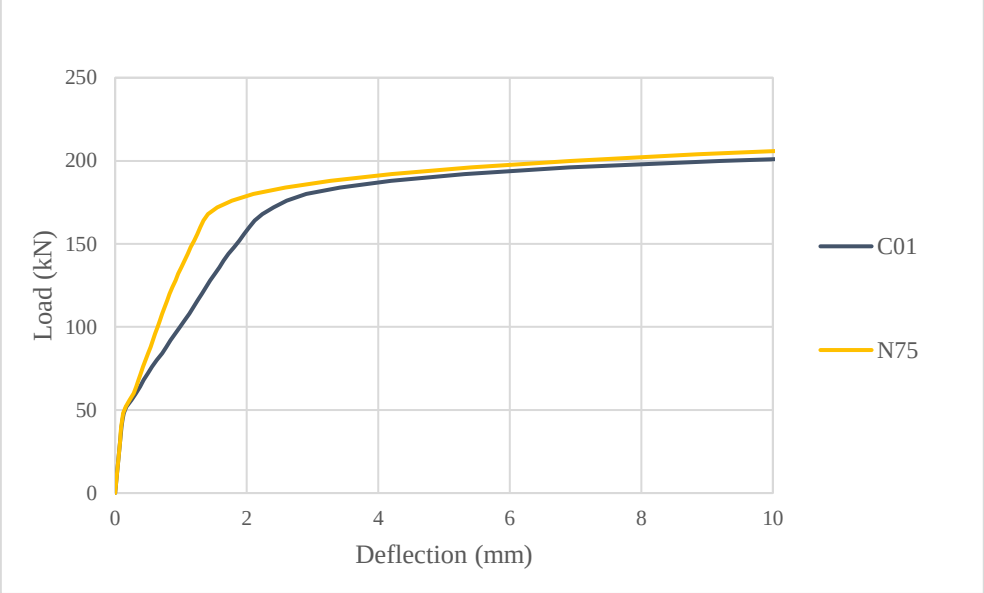

Figure 4.6: Load-displacement Curve of C01 and N75.

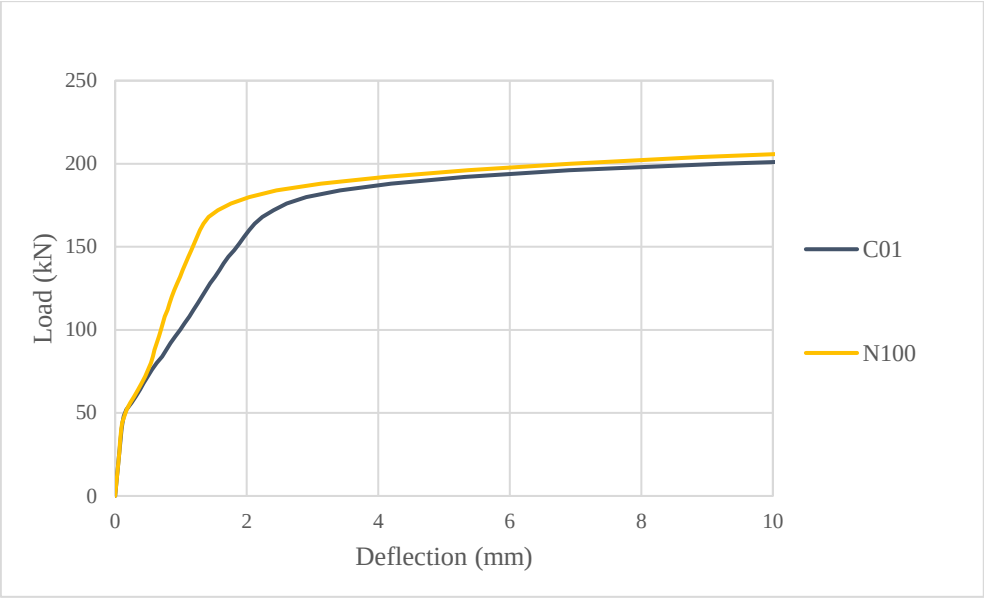

Figure 4.7: Load-displacement Curve of C01 and N100.

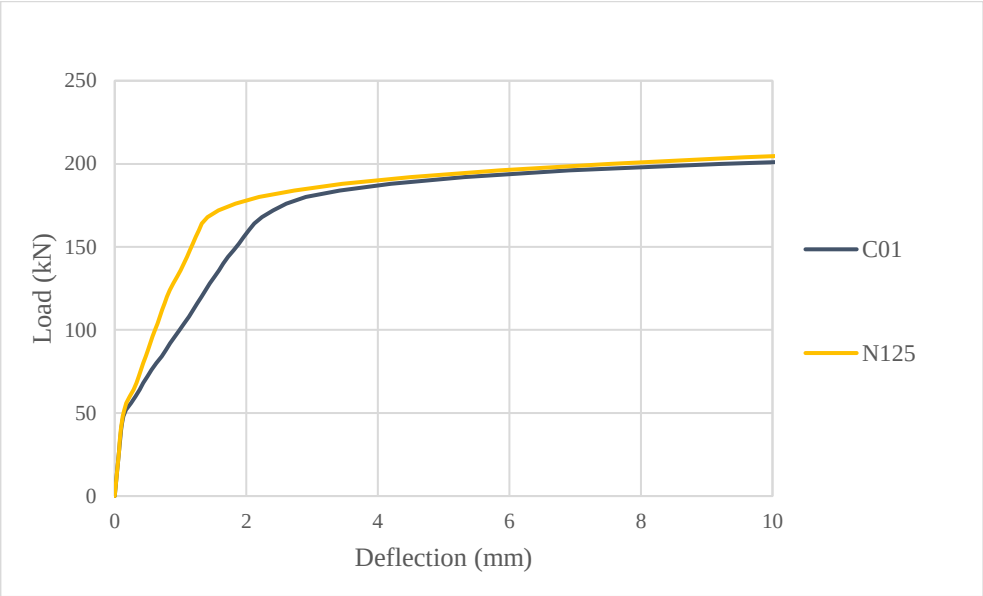

Figure 4.8: Load-displacement Curve of C01 and N125.

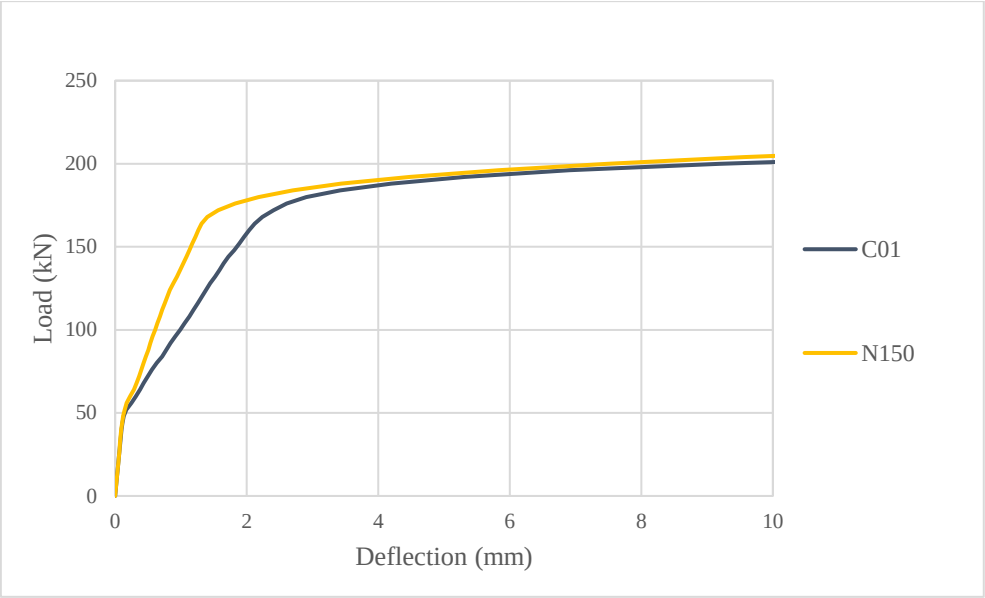

Figure 4.9: Load-displacement Curve of C01 and N150.

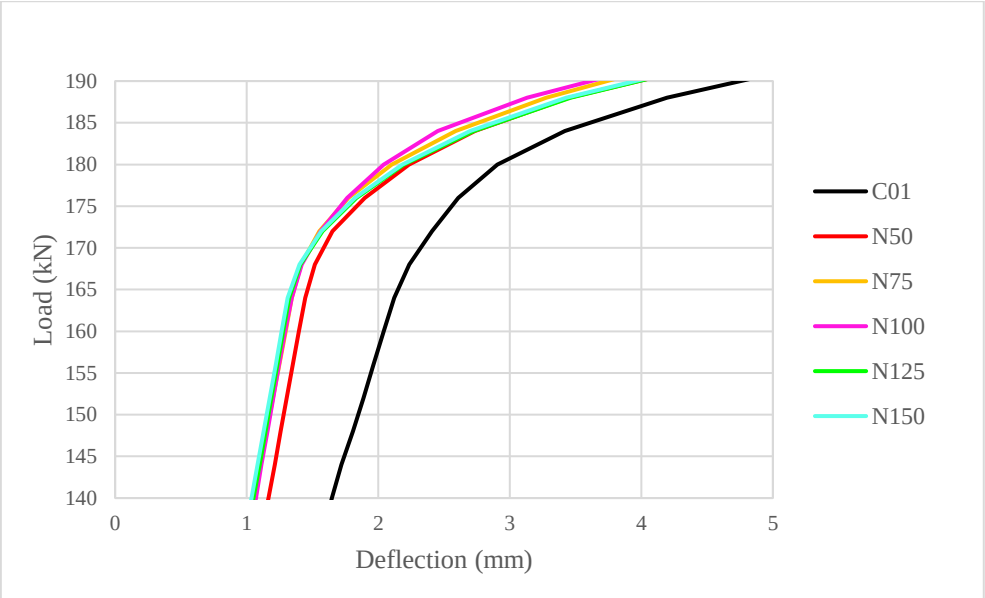

Figure 4.10: Enlarged View at the Yield Point.

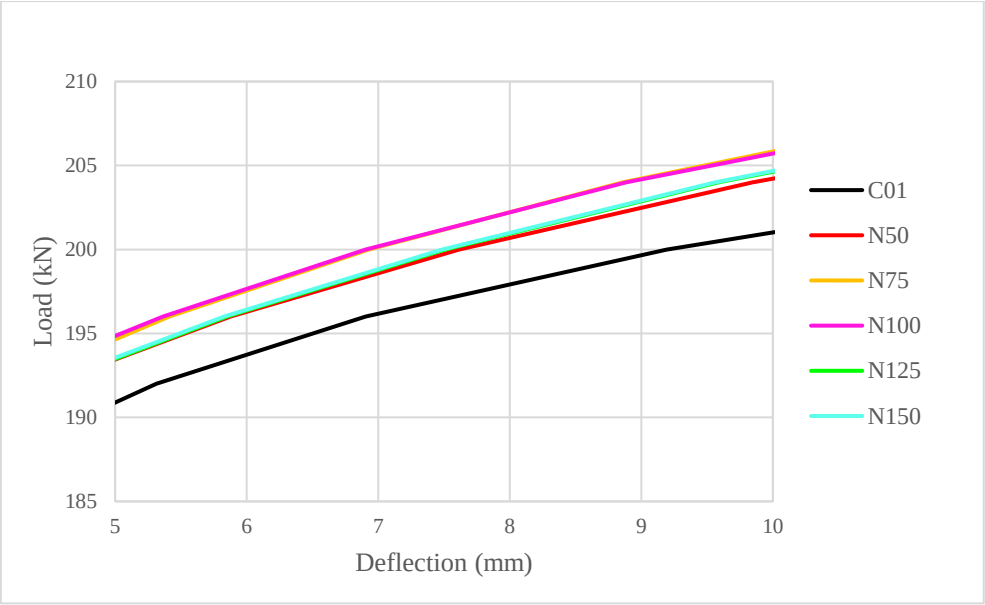

Figure 4.11: Enlarged View at the Fracture Zone.

Table 4.2: Results of Test Specimens.

Specimen	Shear Area (mm2)	Yield Strength (kN)	Percentage Difference (%)	Ultimate Strength (kN)	Percentage Difference (%)
C01	150	164.0	-	201.0	-
N50	264	167.5	2.13	204.2	2.10
N75	300	170.0	3.66	205.7	2.85
N100	339	172.0	4.88	205.8	2.90
N125	375	167.5	2.13	204.6	2.30
N150	376	167.5	2.13	204.7	2.35

The results show that the substitution of thin plates as the shear reinforcement has a noticeable improvement in the ultimate performance of the RC deep beam. Thin shear plates has 1.7 times to 2.5 times the shear reinforcement area provided by conventional shear link. The provided shear reinforcement area increases, as the spacing between the circular holes increases. Thin shear plates also significantly improved the yield strength of the RC deep beam for at least 2.13 % and up to 4.88 % when using 100 mm spacing circular holes thin shear plates. The improvement of the ultimate strength is relatively lower than the yield strength, which ranged from 2.10 % to 2.90 % increment.

The relative small increment in the ultimate strength may be attributed to the reduced bonding strength between steel plates and concrete. Conclusively, both the improvement in yield strength and ultimate strength have proven the ability of circular holes thin shear plates to substitute conventional shear links in RC deep beam, and increasing the load carrying capacity. Besides, the test specimens have improved stiffness as compared to the control beam.

Theoretically, the load carrying capacity of the RC deep beam shall increase as the shear reinforcement area increases. However, the results of N125 and N150 did not comply with the theoretical assumption. The yield strength and ultimate strength of N125 and N150 are lower than N75 and N100, which have smaller shear reinforcement area. The possible cause of this phenomenon is the misinterpretation of the failure point of the test specimens. Due to the lack of experimental data, the failure point of the test specimens was assumed to have occurred at the point where the upcoming numerical deflections were too large and unrealistic, which in this case, was around 10 mm deflection. Therefore, the ultimate strength of the test specimens was being underestimated due to the misinterpretation of the failure point. On the other, the shear reinforcement area of the shear plates was calculated using the full length of the plate. However, in practice, the effective shear area in the form of a compressive strut would be smaller, where located diagonally between the support and the loading point. Thus, there would be an overestimation of the effective shear reinforcement area of the test specimens.

Additionally, the difference in load carrying capacity of all the test specimens is relatively small. This phenomenon is due to the increment of shear reinforcement area has to be very large to yield desirable improvement in the load carrying capacity. It is shown when the difference in shear reinforcement area between C01 and N100 is 126 %, but the increment in ultimate strength is merely 2.85 %. Therefore, the case where the small difference in load carrying capacity between the test specimens is explainable since the specimens have almost similar shear reinforcement area.

In conclusion, circular holes thin shear plates as the shear reinforcement had improved the load-carrying capacity of RC deep beams. Thin plates are proved to be a reliable substitute to conventional shear link to resolve reinforcement congestion issue yet providing sufficient load-carrying capacity.

4.5 Optimization

Based on Table 4.2, specimen N100 reinforced with 100 mm spaced circular holes thin shear plates has the most optimized performance among the test specimens. N100 has the highest improvement in the yield strength, which is 4.88 %. Furthermore, the improvement in the ultimate strength of N100 is an impactful 2.90 %. Therefore, specimen N100 was chosen as the optimum design for the shear plates to continue with further discussions in terms of the von Mises stress distribution, PEMAG plastic strain, concrete tension damage.

The results of test specimen N50, N75, N125, and N150 are attached in Appendix B for reference purposes.

4.6 Generalization and Comparison between Control Beam, C01 and Test Specimen, N100

The discussion continues with the generalization and comparison between the results of the control beam, C01 and the optimized specimen N100. Four subjects are discussed, including von Mises stress in concrete, von Mises stress in reinforcement, concrete plastic strain magnitude (PEMAG), and concrete tension damage. Adequate explanations are provided to clarify the results, and graphical representations such as contours and figures were included to predict the real-life behaviour of RC deep beam.

4.6.1 Concrete Von Mises Stress Contour

The concrete von Mises stress contour of the control beam, C01, and test specimen, N100 were generated using ABAQUS contour plots. Generally, von Mises stress is an indicator of the yield point and the fracture point of a material. Hence, the von Mises contour was captured at two points in terms of the mid-span deflection. The first point is the yield point assumed at 1.5 mm deflection, followed by the ultimate point, which was assumed at 10 mm mid-span deflection. Figure 4.12 and Figure 4.13 show the concrete von Mises stress contour of the control beam, C01, while Figure 4.14 and Figure 4.15 show the concrete von Mises stress contour of the test specimen, N100. Table 4.3 tabulates the peak concrete stress magnitude at respective capture points.

First, the von Mises contours describe the stress distribution in the specimens. Stresses were concentrated at the compression region, higher at the

middle and eventually dispersed to the beam ends. Upon yielding, stresses were developed in the beam cross-section where the concrete compressive strut was located. Stresses were then propagated diagonally along the concrete compressive strut and penetrated towards the supports. The stresses continued to develop until the ultimate point, and the peak stresses at the loading points which indicated in red would cause concrete crushing at the tip of the diagonal crack. Minimal flexural stress was developed at the beam mid-span. The beam is concluded to be failed under shear compression failure along the concrete compressive strut based on the stress development process.

Circular holes thin plates as shear reinforcement in N100 had aided in distributing stress in the compression region. As shown in the contours, stresses in N100 were distributed more evenly and broader over the compression region. Comparing the peak stress magnitude at 10 mm deflection in Table 4.3, N100 had 2.23 % reduced peak stress than C01. The stress reduction could be explained by the effective performance of the thin shear plates in the stress distribution, thereby reducing the stress exerted to the concrete. Furthermore, the stresses along the diagonal strut and near the compression region were also dispersed and reduced in N100, as shown in Figure 4.15. Lastly, both C01 and N100 had minimal flexural stress at the beam mid-span, with a smaller magnitude in N100.

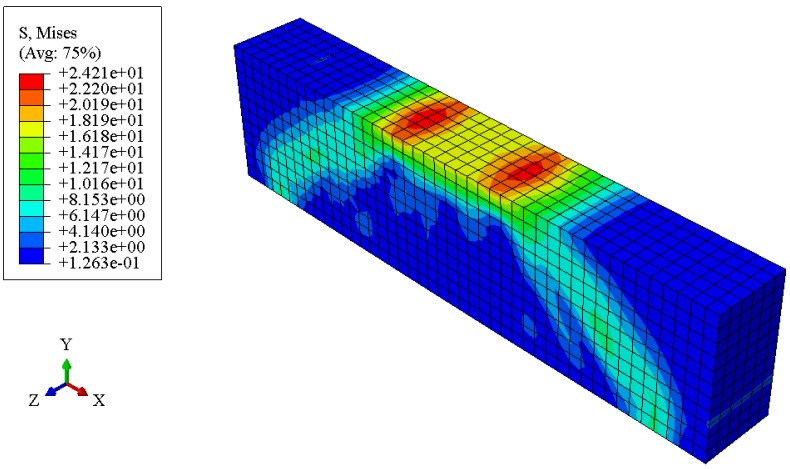

Figure 4.12: Concrete Von Mises Stress Contour of C01 at 1.5 mm.

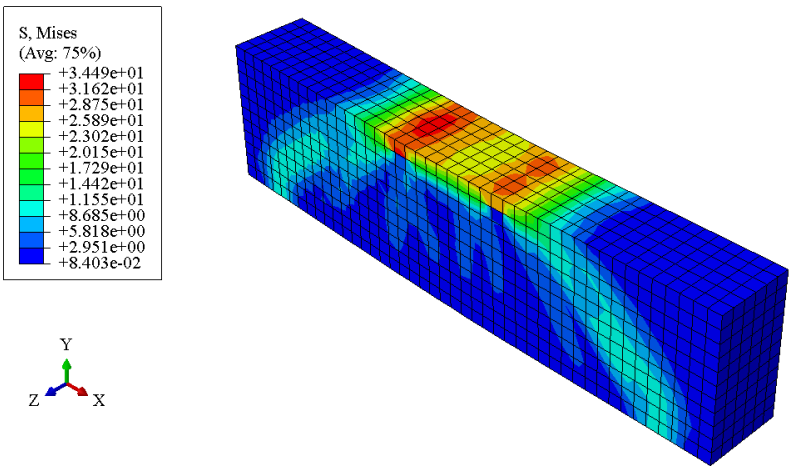

Figure 4.13: Concrete Von Mises Stress Contour of C01 at 10 mm.

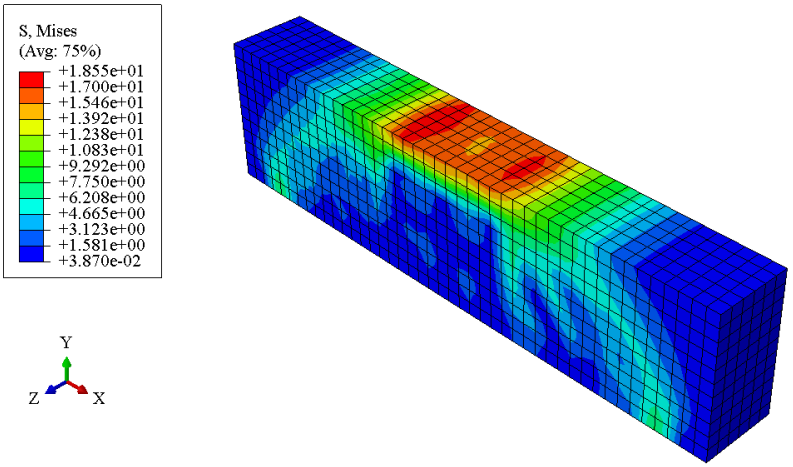

Figure 4.14: Concrete Von Mises Stress Contour of N100 at 1.5 mm.

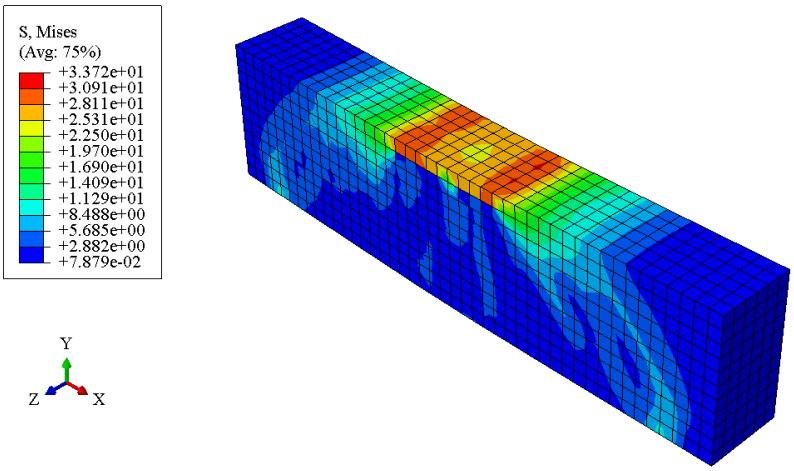

Figure 4.15: Concrete Von Mises Stress Contour of N100 at 10 mm.

Table 4.3: Concrete Von Mises Stress Magnitude.

Specimen	Peak Stress at 1.5 mm (kN/mm^2)	Percentage Difference (%)	Peak Stress at 10 mm (kN/mm^2)	Percentage Difference (%)
C01	24.21	-	34.49	-
N100	18.55	-23.38	33.72	-2.23

4.6.2 Reinforcement Von Mises Stress Contour

Von Mises contours of the steel cage together with the steel plates were generated to investigate the stress changes of the entire reinforcement system throughout the loading process. Likewise, the von Mises stress contour was captured at 1.5 mm and 10 mm deflection to represent the stresses in the reinforcement at the yield point and the fracture point respectively. Figure 4.16 and Figure 4.17 show the reinforcement von Mises stress of the control beam, C01. Figure 4.18 and Figure 4.19 show the reinforcement von Mises stress contour of the test specimen, N100. Table 4.4 tabulates the peak reinforcement stress magnitude at respective capture points.

The stress distribution of the reinforcement is dissimilar to the stress distribution in concrete. High tensile stress was first developed at the bottom tension region, while only mild stress appeared on top. Accumulation of high tensile stresses in the bottom reinforcement can be adequately explained by the natural ability of steel bars in resisting high tension that developed at the concave tension zone. As the loading proceeded to fracture, the high tensile stresses in the bottom bars were spread to a further extent, and the top bars were severely stressed as well. It is important not to overlook the increment of tensile stresses from yield to fracture are merely 4.58 % and 6.88 % in C01 and N100 respectively. A possible explanation is RC deep beam complies with the strut and tie model where the loading is resisted by the concrete compressive strut, thereby failing in shear instead of tension. Therefore, the increment of the reinforcement tensile stresses between these two stages is insignificant.

Apart from that, the stress distribution of the circular holes thin shear plates is similar to the steel bars, particularly at the beam midspan. Whereas, the shear plates had clear existence of diagonal stresses as in the shape of a compressive strut. It is possible to conclude that the shear plates resist shear

stresses due to the arch action in a strut and tie model. Hence, shear plates are proven to be a feasible alternative to replace shear links in deep beam.

Lastly, Table 4.4 shows that the reinforcement peak stress of N100 is 1.79 % higher than C01 at 10 mm deflection. However, the concrete peak stress of C01 is 2.23 % higher than N100, as mentioned in Section 4.6.1. These results appear to confirm the ability of shear plates to resist higher stress, thereby reducing the stresses in concrete and increasing the beam's capacity.

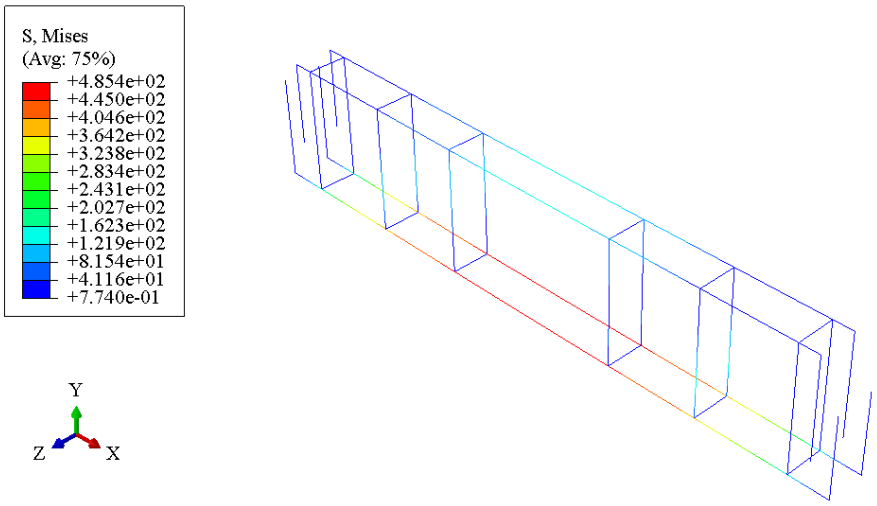

Figure 4.16: Reinforcement Von Mises Stress Contour of C01 at 1.5 mm.

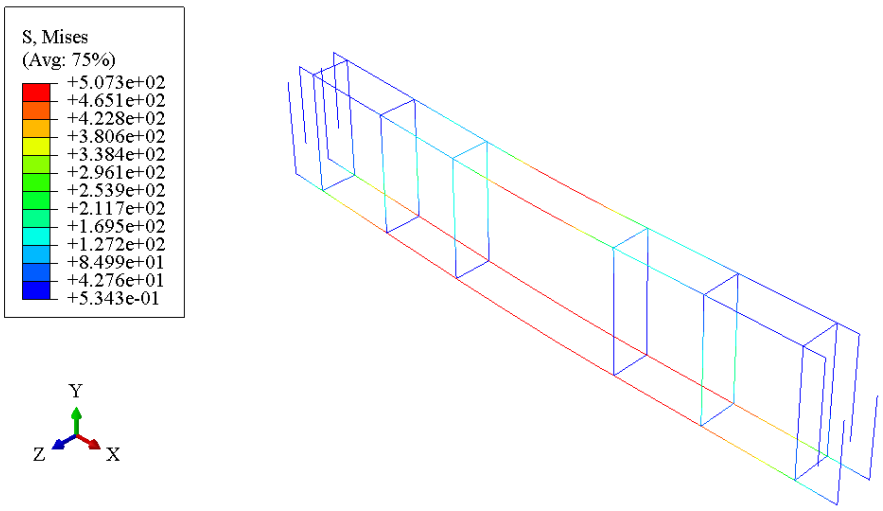

Figure 4.17: Reinforcement Von Mises Stress Contour of C01 at 10 mm.

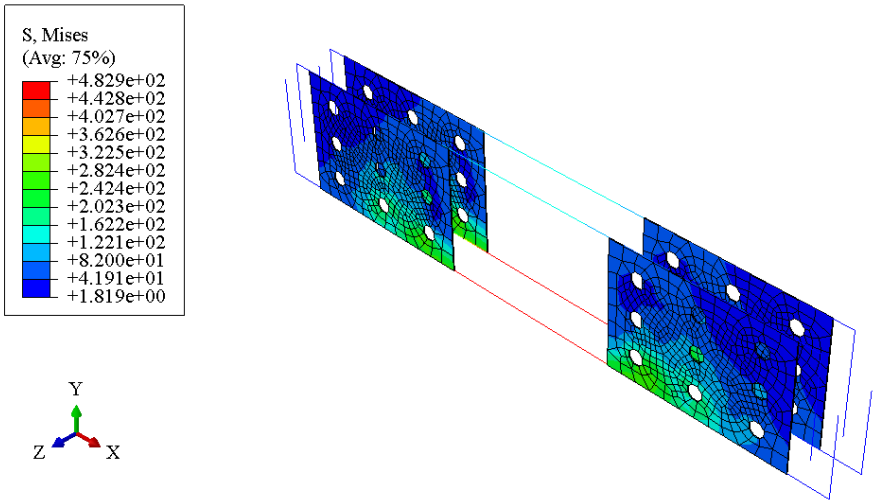

Figure 4.18: Reinforcement Von Mises Stress Contour of N100 at 1.5 mm.

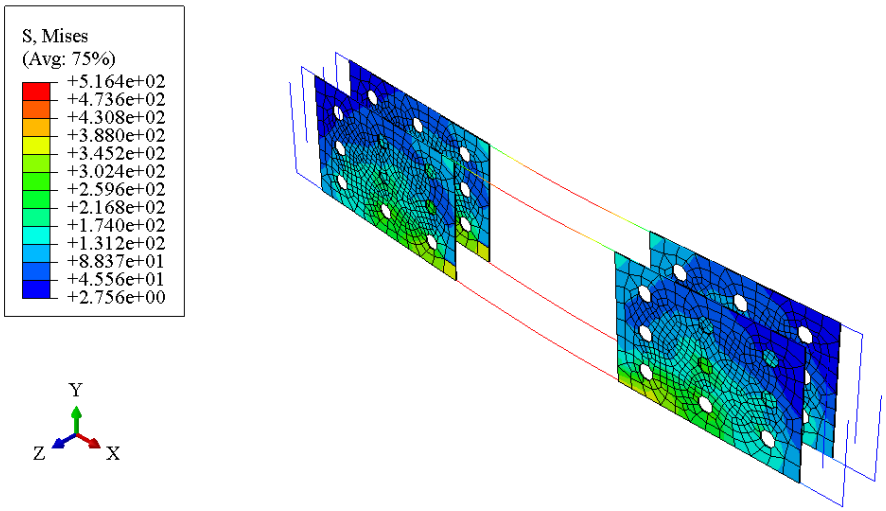

Figure 4.19: Reinforcement Von Mises Stress Contour of N100 at 10 mm.

Table 4.4 Reinforcement Von Mises Stress Magnitude.

Specimen	**Peak Stress at 1.5 mm (kN/mm^2)**	**Percentage Difference (%)**	**Peak Stress at 10 mm (kN/mm^2)**	**Percentage Difference (%)**
C01	485.40	-	507.30	-
N100	482.90	-0.52	516.40	1.79

4.6.3 Plastic Strain Magnitude (PEMAG) Diagram

Plastic strain magnitude (PEMAG) diagrams illustrated the crack distribution in the concrete in terms of the concrete plastic strain. PEMAG diagrams of the RC deep beams were captured at the yield point and the fracture point of the concrete to study the crack development across these two stages. The 1.5 mm mid-span deflection was the first capture point to represent the plastic strain at yield, while 10 mm mid-span deflection was the second capture point to represent the plastic strain at fracture. Figure 4.20 and Figure 4.21 illustrate the PEMAG diagram of the control beam, C01. Figure 4.22 and Figure 4.23 illustrate the PEMAG diagram of the test specimen, N100.

PEMAG diagrams provide a clear illustration of the plastic strain development in concrete. In both C01 and N100, plastic strain started to develop at the tension region during yield, thereby forming scattered vertical cracks at the midspan. Diagonal plastic strain with smaller magnitude indicates the development of diagonal microcracks origin from the supports and propagated along the concrete compressive strut. As the loading increased to fracture, both the existing vertical and diagonal plastic strain magnitude increased drastically, and deeper cracks were formed. Moreover, the presence of plastic strain at the compression region shows concrete crushing between the two loading points.

The PEMAG diagrams show a significant difference in the plastic strain distribution area between the control, C01, and test specimen, N100 at both the compression and tension region. Plastic strain in N100 propagated over a narrower area as compared to C01. The convergence of the plastic strain in the test specimen shows that circular holes thin shear plates are effective in limiting the spread of cracks in RC deep beams. On the other hand, the peak plastic strain magnitude was compared to investigate the increment of the plastic strain from yield to fracture. Peak plastic strain of C01 are 0.01312 mm and 0.04786 mm at yield and fracture respectively, which is an increment of 265 %. In comparison, N100 has a higher increment of peak plastic strain from 0.01066 mm to 0.04894 mm, which is 360 %. The more severe plastic strain increment in N100 can be attributed to the increased beam stiffness and the reduced bonding strength between the thin shear plates and concrete.

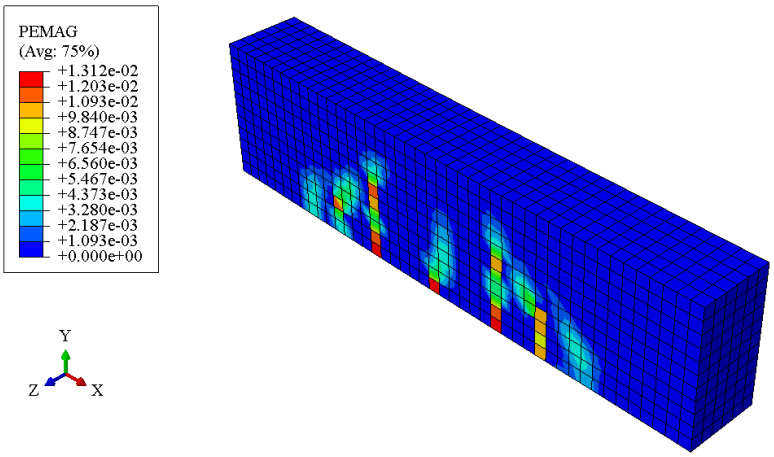

Figure 4.20: PEMAG Diagram of C01 at 1.5 mm.

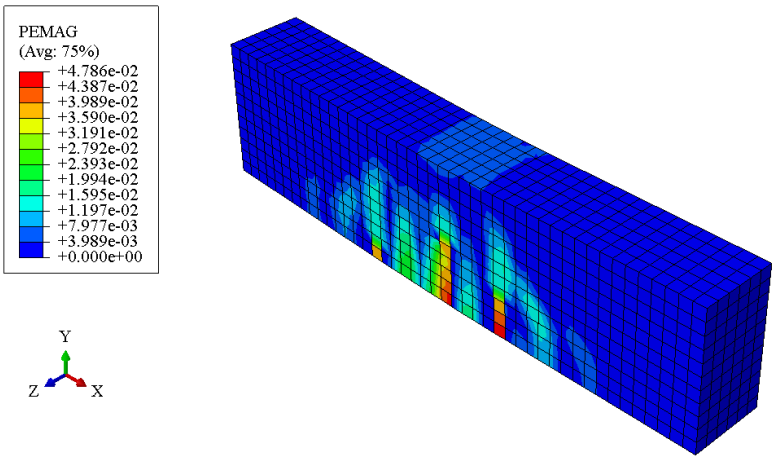

Figure 4.21: PEMAG Diagram of C01 at 10 mm.

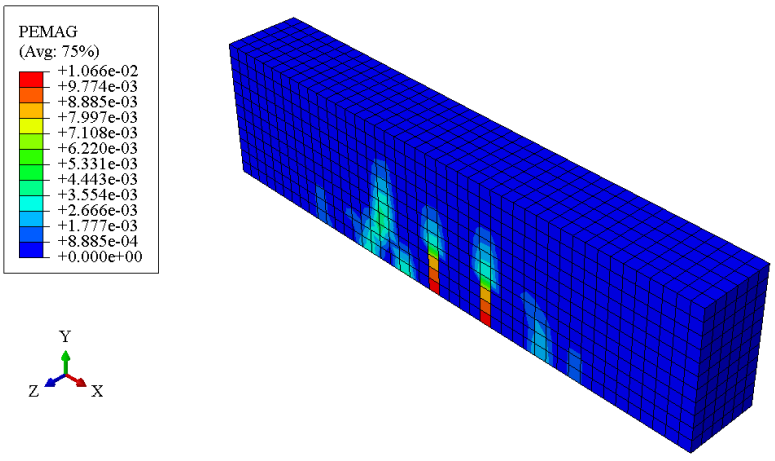

Figure 4.22: PEMAG Diagram of N100 at 1.5 mm.

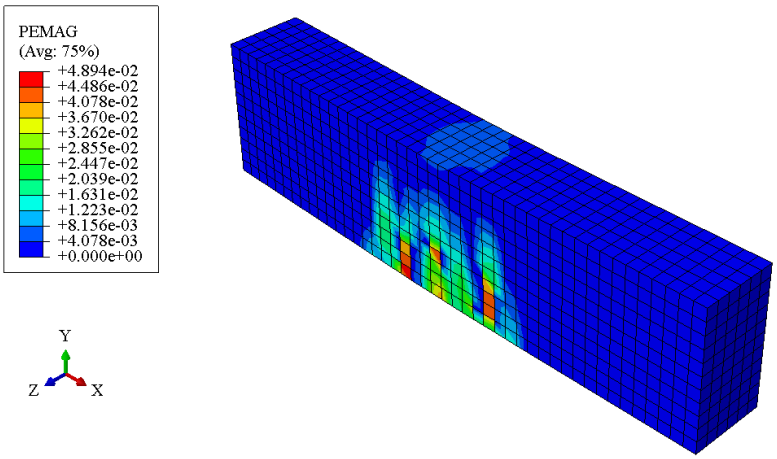

Figure 4.23: PEMAG Diagram of N100 at 10 mm.

4.6.4 Concrete Tension Damage Contour

Concrete tension damage contour is another graphical illustration of cracks development in concrete by the definition of post cracking damage due to tensile stresses. Tension damage contour is a preferable option to simulate crack pattern numerically in RC deep beam due to its ability to yield accurate and precise simulations (Ibrahim, et al., 2018; Jasim, et al., 2020). Tension damage contour were captured at the yield point and the fracture point of the concrete, which were 1.5 mm deflection and 10 mm deflection respectively. One additional capture point was included at 6 mm deflection to obtain a more detailed observation on the developed cracks. Figure 4.24 to Figure 4.26 show the tension damage contour of C01, while Figure 4.27 to Figure 4.29 show the tension damage contour of N100 at 1.5 mm, 6 mm, and 10 mm respectively.

In both C01 and N100, vertical cracks started to develop at the beam midspan at 1.5 mm deflection, and mild diagonal cracks started from the supports. Vertical cracks at the midspan can be accounted by the tensile stress generated in the vertical direction of the tensile tie, which is known as the bursting tensile force. At 6 mm deflection, there were only a few new vertical cracks added in the midspan. However, there were a significant growth of diagonal cracks along the concrete compressive strut and extended to the loading points. The diagonal concrete strut formed an arch action connected by a tension tie at the bottom, and illustrated the strut and tie mechanism in RC deep beams. Furthermore, the compression region at the loading points experienced minor loss in strength. When the beam was loaded to 10 mm, severe

diagonal cracks were developed in the shear span and the concrete compressive strut towards the loaders, thus indicating a shear compression failure in the deep beam. Eventually, the beam failed upon the crushing of concrete strut due to diagonal compression.

Tension damage contour generates an identical crack pattern simulation to the cracks stimulated using plastic strain magnitude (PEMAG) diagrams. However, tension damage contour provides more sensitive and accurate results because it included diagonal cracks development that defined the failure mode of the deep beams. The tension damage contour noted that the tension variable was 0.9, which indicates a nearly total loss in concrete strength. Consequently, severe cracks are formed, and crushing of concrete will occur.

Additionally, concrete tension damage in N100 appears to be fewer as compared to C01, as shown over the three capture points. N100 had comparatively lesser cracks at both the loading region and beam midspan in contrast to C01. Moreover, the less diagonal cracks in the compressive strut are worth noting because diagonal cracks are governing deep beam failures. Hence, the reduction of cracks at all region provided clear evidence that circular holes thin shear plates as a substitute for conventional shear links are effective in improving the capacity of deep beam.

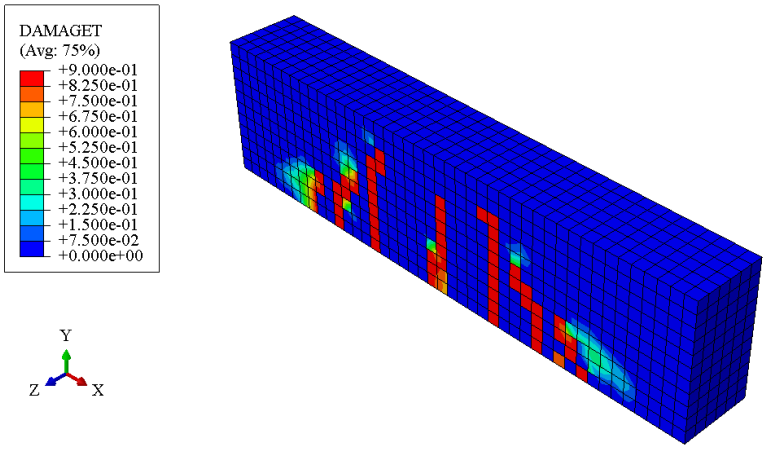

Figure 4.24: Tension Damage Contour of C01 at 1.5 mm.

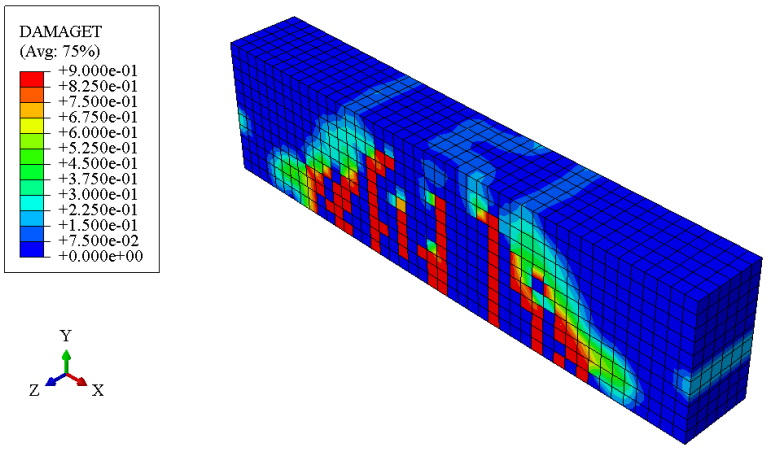

Figure 4.25: Tension Damage Contour of C01 at 6 mm.

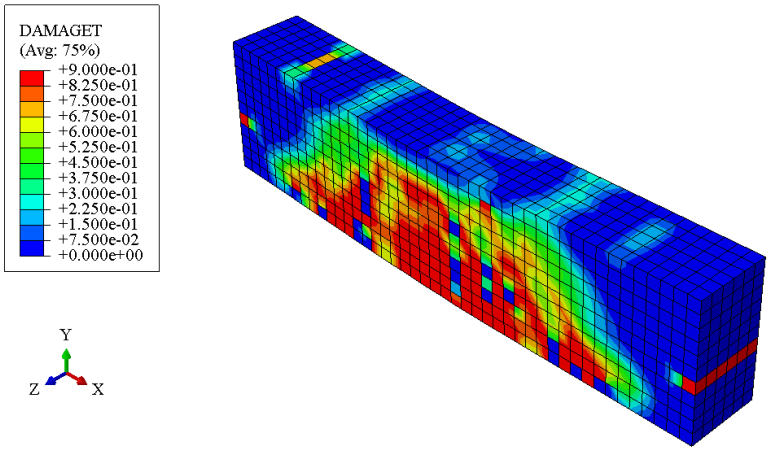

Figure 4.26: Tension Damage Contour of C01 at 10 mm.

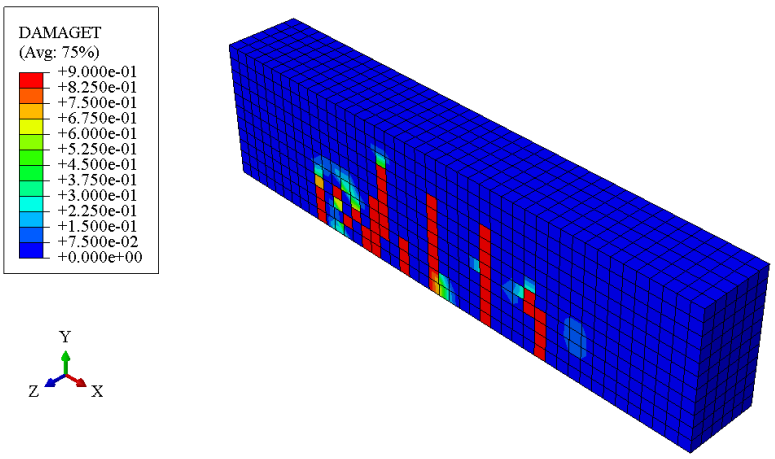

Figure 4.27: Tension Damage Contour of N100 at 1.5 mm.

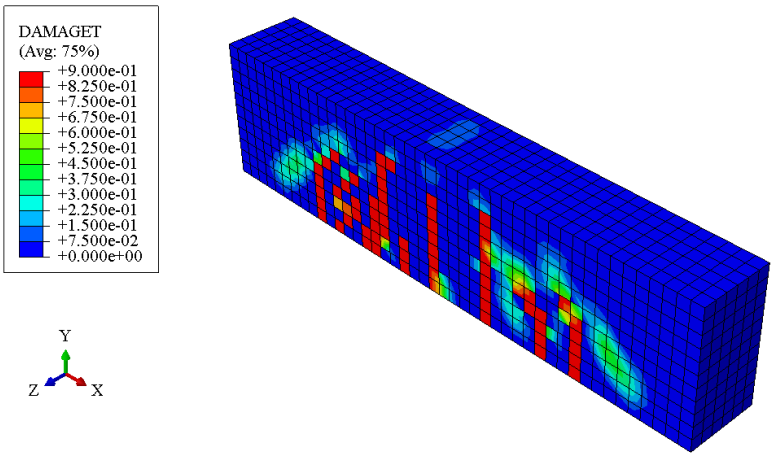

Figure 4.28: Tension Damage Contour of N100 at 6 mm.

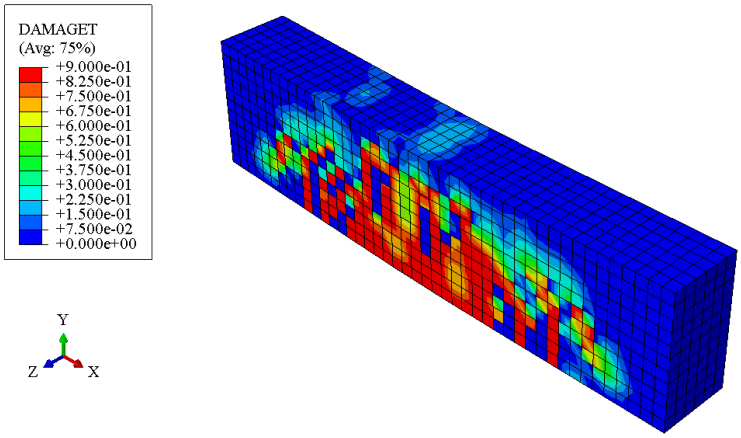

Figure 4.29: Tension Damage Contour of N100 at 10 mm.

4.7 Summary

Chapter 4 started by comparing the numerical results generated using ABAQUS software and the experimental results published by Jasim, et al. (2020). Good matching of the results was observed, thereby proving the validity of the material properties and simulation technique. Numerical modelling continued to generate results for the control beam with conventional shear links, and test specimens with circular holes thin shear plates. Load displacement curves were plotted to investigate the strength performance of the specimens, and the optimum spacing was determined. The last section of Chapter 4 investigated the stress capacity and numerical deformation of the optimized design based on the von Mises stress contour, plastic strain magnitude (PEMAG) diagram, and concrete tension damage contour.

CHAPTER 5

CONCLUSION AND RECOMMENDATIONS

5.1 Conclusion

In conclusion, a finite element analysis (FEA) was completed using ABAQUS software. Seven numerical specimens were developed, including one reference beam, R01, one control beam, C01, and five test specimens with 50 mm, 75 mm, 100 mm, 125 mm, and 150 mm circular holes spacing, which are denoted as N50, N75, N100, N125, and N150 respectively. The study objectives were achieved throughout the numerical analysis process.

The first objective is to verify the numerical results of the reference beam with the experimental results. A referential numerical model was established according to the modelling methodology as listed in Chapter 3, including material properties modelling, interaction properties modelling, element type, mesh size, boundary conditions, and loading definition. The numerical results generated were verified with experimental results published by Jasim, et al. (2020). A good matching load-displacement curve was observed, and the percentage difference in the yield strength was merely 8.62 %. Besides, the concrete tension damage contour generated to predict the crack pattern is in good agreement with the experimental observations. The established numerical model was reliable to carry on with the numerical analysis of the control beam and the test specimens.

The second objective is to evaluate the load-displacement behaviour of RC deep beam with circular holes thin shear plates. Based on the results, the yield strength of the test specimens has improved by 2.13 % to 4.88 %. Also, the improvement of the ultimate strength is 2.10 % to 2.90 %. Low bonding strength between the steel plates and concrete is a contributing factor to the relatively small increment in the load-carrying capacity.

The third objective is to determine an optimum design of RC deep beam embedded with circular holes thin shear plates of various opening spacing. Test specimen embedded with 100 mm holes spacing shear plates, N100 has the largest improvement in yield strength and ultimate strength, which are 4.88 % and 2.90 % respectively. Hence, N100 was determined as the optimum design.

Discussions were continued to investigate the stress capacity and numerical deformation of the optimum design. Von Mises stress contour of concrete and reinforcement were plotted. N100 was found to have a 2.23 % reduced concrete peak stress than C01. Reduced stress in concrete is due to N100 reinforcement resisted 1.79 % greater stress than C01. Moreover, according to the plastic strain magnitude (PEMAG) diagram and tension damage contour, N100 was predicted to deform and fail in shear at the concrete compressive strut.

The accomplishment of all the study objectives had constituted the achievement in the study's aim to perform a numerical analysis of reinforced concrete (RC) deep beam with circular holes thin shear plates.

This study concluded that 100 mm circular holes thin shear plate is a viable alternative to replace conventional shear links in RC deep beams to resolve the problem statements of improving load carrying capacity and eliminating concrete honeycomb. In addition, FEA using ABAQUS is an accurate, time, and cost-saving approach in solving complex engineering problems. Establishing the above-mentioned solutions confirm the significancy of this study's significance to the civil engineering field.

5.2 Recommendations

The proposed circular holes thin shear plate is a relatively novel and undiscovered reinforcement design for the RC deep beam. Hence, there is space for improvements and modifications to match different aims and objectives. The following recommendations are proposed for future studies.

The first recommendation is the application of an alternative concrete stress-strain relationship model. The proposed Carreira and Chu (1985) stress-strain equations have limited ability in modelling the real-life behaviour of concrete. For instance, Carreira and Chu (1985) equations consider the complete cylinder strength as the ultimate stress, f_{ck}. However, the modified Hognestad model established by MacGregor and Wight (2011) introduce a 0.9 reduction factor to include the water-gain effects during the curing and placing of concrete, the modified ultimate stress is considered as $f_{ck}' = 0.9\ f_{ck}$. Additional parameter provided in the equations could increase the modelling accuracy, thereby generating numerical results that fit better with experimental results.

The second recommendation is the modification in the proposed detailing. In this study, the results show a minute difference in the load carrying capacity between various spacings. Future studies could implement steel plates with different thickness or circular holes configuration to investigate the effect on the load carrying capacity. Also, manipulation in the types of steel plates such as using hot-rolled steels, and cold-formed steels could be used to study the relationship between steel yield strength and beam load carrying capacity.

The last recommendation is to include experimental results for the test specimens for verification purposes. In the midst of the COVID-19 pandemic, this study encountered physical constraint to conduct laboratory testing for experimental results. The model validation was completed using the reference by Jasim, et al. (2020), which is rather insufficient, especially in the visualization of the crack pattern. Therefore, laboratory testing should be conducted to produce experimental results and verify the numerical results to write up a more convincing conclusion.

REFERENCES

Adinkrah-Appiah, K., Adom-Asamoah, M., Afrifa, R.O. and Abeka, H., 2018. *Evaluation of shear strength of reinforced concrete deep beams*. In: KNUST (Kwame Nkrumah University of Science and Technology), 1st International Conference on Engineering, Science, Technology and Entrepreneurship (ESTE). Kumasi, Ghana, 6-7 August 2015. Kumasi: KNUST.

Albidah, A., Abadel, A., Abbas, H., Almusallam, T. and Al-Salloum, Y., 2019. Experimental and analytical study of strengthening schemes for shear deficient RC deep beams. *Construction and Building Materials*, [e-journal] Volume 216, pp.673-686. https://doi.org/10.1016/j.conbuildmat.2019.05.024.

American Concrete Institution, 2014. *ACI 318R-14 Commentary on building code requirements for structural concrete*. [online] ACI. Available through: ACI website <https://www.concrete.org/Portals/0/Files/PDF/Previews/318-14_preview1.pdf> [Accessed 2 July 2020].

Barnes, R.A., Baglin, P.S., Mays, G.C. and Subedi, N.K., 2001. External steel plate systems for the shear strengthening of reinforced concrete beams. *Engineering Structures*, [e-journal] 23(9), pp.1162-1176. https://doi.org/10.1016/S0141-0296(00)00124-3.

Beres, A.B. and Rabbatm B.G., 2007. Strut-and-Tie Model for Structural Concrete Design. [e-book] Portland Cement Association. Available at: Structure Point website <https://structurepoint.org/publication/pdf/pdh-Strut-And-Tie-Design-Method.pdf> [Accessed 20 July 2020].

Carreira, D.J. and Chu, K.H., 1985. Stress-strain relationship for plain concrete in compression. *ACI Jorunal, Proceedings*, 82(6), pp.797-804.

Chen, C.C., Lin, K.T. and Chen, Y.J., 2018. Behavior and shear strength of steel shape reinforced concrete deep beams. *Engineering Structures*, [e-journal] Volume175, pp.425-435. https://doi.org/10.1016/j.engstruct.2018.08.045.

Chiriki, S.S. and Harsha, G.S., 2020. Finite element analysis of RC deep beams strengthened with I-section and truss reinforcement. *Materials Today: Proceedings*, [e-journal] https://doi.org/10.1016/j.matpr.2020.03.579.

Choi, Y.W., Lee, H.K., Chu, S.B., Cheong, S.H. and Jung, W.Y., 2012. Shear behavior and performance of deep beams made with self-compacting concrete. *International Journal of Concrete Structures and Materials*, [e-journal] 6(2), pp.65-78. https://doi.org/10.1007/s40069-012-0007-y.

Courant, R., 1943. Variational methods for the solution of problems of equilibrium and vibrations. *Bulletin of the American Mathematical Society*, [e-journal] Volume 49, pp.1-23. https://doi.org/10.1090/S0002-9904-1943-07818-4.

Dassault Systèmes Simulia Corp., 2017. *Applying Boundary Conditions to the Frame*. [online] Available at: <https://abaqus-docs.mit.edu/2017/English/SIMACAEGSARefMap/simagsa-t-applyingboundaryconditionstotheframe.htm> [Accessed 25 August 2020].

Dassault Systèmes Simulia Corp., 2017. *Coupling Constraints*. [online] Available at: <https://abaqus-docs.mit.edu/2017/English/SIMACAECSTRefMap/simacst-c-coupling.htm#simacst-c-coupling-t-KinematicCouplingConstraints-sma-topic5> [Accessed 25 August 2020].

Dassault Systèmes Simulia Corp., 2017. *Embedded Elements*. [online] Available at: <https://abaqus-docs.mit.edu/2017/English/SIMACAECSTRefMap/simacst-c-embeddedelement.htm> [Accessed 25 August 2020].

Demir, A., Ozturk, H. and Dok, G., 2016. 3D numerical modeling of RC deep beam behavior by nonlinear finite element analysis. *Disaster Science and Engineering*, 2(1), pp.13-18.

El Maaddawy, T. and Sherif, S., 2009. FRP composites for shear strengthening of reinforced concrete deep beams with openings. *Composite Structures*, [e-journal] 89(1), pp.60-69. https://doi.org/10.1016/j.compstruct.2008.06.022.

European Commision, 2004. BS EN 1992-1-1:2004 Eurocode 2: *Design of concrete structures – Part 1-1: General rules and rules for buildings.*

Farghaly, A.S. and Benmokrane, B., 2013. Shear behavior of FRP-reinforced concrete deep beams without web reinforcement. *Journal of Composites for Construction*, [e-journal] 17(6). https://doi.org/10.1061/(ASCE)CC.1943-5614.0000385.

Hawileh, R.A., El-Maaddawy, T.A. and Naser, M.Z., 2012. Nonlinear finite element modeling of concrete deep beams with openings strengthened with externally-bonded composites. *Materials & Design*, [e-journal] Volume 42, pp.378-387. https://doi.org/10.1016/j.matdes.2012.06.004.

Hognestad, E., 1951. *Study of combined bending and axial load in reinforced concrete members*. [e-book] University of Illinois at Urbana Champaign, College of Engineering. Engineering Experiment Station. Available at: IDEALS <http://hdl.handle.net/2142/4360> [Accessed 20 August 2020].

Hrennikoff, A.P., 1941. Solution of problems of elasticity by the framework method. *Journal of Applied Mechanics*, 8(4), pp. 169-175.

Ibrahim, A.M. and Mahmood, M.S., 2009. Finite element modeling of reinforced concrete beams strengthened with FRP laminates. *European Journal of Scientific Research*, ˚(4), pp.526-541.

Ibrahim, M., Wakjira, T. and Ebead, U., 2020. Shear strengthening of reinforced concrete deep beams using near-surface mounted hybrid carbon/glass fibre

reinforced polymer strips. *Engineering Structures*, [e-journal] Volume 210. https://doi.org/10.1016/j.engstruct.2020.110412.

Ibrahim, M.A., El Thakeb, A., Mostfa, A.A. and Kottb, H.A., 2018. Proposed formula for design of deep beams with shear openings. *HBRC Journal*, [e-journal] 14(3), pp.450-465. https://doi.org/10.1016/j.hbrcj.2018.06.001.

Islam, M.R., Mansur, M.A. and Maalej, M., 2005. Shear strengthening of RC deep beams using externally bonded FRP systems. *Cement and Concrete Composites*, [e-journal] 27(3), pp.413-420. https://doi.org/10.1016/j.cemconcomp.2004.04.002.

Ismail, K.S., 2016. *Shear behaviour of reinforced concrete deep beams.* PhD. University of Sheffield.

Jasim, W.A., Allawi, A.A. and Oukaili, N.K., 2018. Strength and serviceability of reinforced concrete deep beams with large web openings created in shear spans. *Civil Engineering Journal*, [e-journal] 4(11), pp.2560-2574. https://doi.org/10.28991/cej-03091181.

Jasim, W.A., Tahnat, Y.B.A. and Halahla, A.M., 2020. Behavior of reinforced concrete deep beam with web openings strengthened with (CFRP) sheet. *Structures*, [e-journal] Volume 26, pp.785-800. https://doi.org/10.1016/j.istruc.2020.05.003.

Kachlakev, D., Miller, T., Yim, S., Chansawat, K. and Potisuk, T., 2001. *Finite element modeling of concrete structures strengthened with FRP laminates*. PhD. California Polytechnic State University.

Kang, T.H., Kim, W., Lam, K.M., Martin, R.D., Kim, K., Huang, Y. and Holliday, L., 2012. *Relief of Reinforcing Congestion in Beams and Bent Caps of Concrete Bridges.* [online] Midwest City: Oklahoma Transportation Center. Available at: <http://www.oktc.org/otc/files/finalReports/OTCREOS9.1-27-F.pdf> [Accessed 2 August 2020].

Kefelegn, A. and Gebre, A., 2020. Performance of self-compacting concrete used in congested reinforcement structural element. *Engineering Structures*, [e-journal] Volume 214. https://doi.org/10.1016/j.engstruct.2020.110665.

Khai, M.Q., Han, S.W., Shin, M. and Lee, K., 2017. Reduction of reinforcement congestion in slender coupling beam using bundled diagonal bars. Magazine of Concrete Research, [e-journal] 69(22), pp. 1157-1169. https://doi.org/10.1680/jmacr.16.00530.

Kotsovos, G.M., Vougioukas, E. and Kotsovos, M.D., 2013. Reducing steel congestion without violating seismic performance requirements. *Structural Journal*, 110(3), pp.427-436.

Leng, Y.B., Song, X.B. and Wang, H.L., 2015. Failure mechanism and shear strength of steel–concrete–steel sandwich deep beams. *Journal of Constructional Steel Research*, [e-journal] Volume 106, pp.89-98. https://doi.org/10.1016/j.jcsr.2014.12.012.

Li, L.Z., Cai, Z.W., Lu, Z.D., Zhang, X.L. and Wang, L., 2017. Shear performance of bolted side-plated reinforced concrete beams. *Engineering Structures*, [e-journal] Volume 144, pp.73-87. https://doi.org/10.1016/j.engstruct.2017.04.043.

Li, L.Z., Wu, Z.L., Yu, J.T., Wang, X., Zhang, J.X. and Lu, Z.D., 2018. Numerical simulation of the shear capacity of bolted side-plated RC beams. *Engineering Structures*, [e-journal] Volume 171, pp.373-384. https://doi.org/10.1016/j.engstruct.2018.06.003.

Lima, M.M., Doh, J.H., Hadi, M.N. and Miller, D., 2016. The effects of CFRP orientation on the strengthening of reinforced concrete structures. *The Structural Design of Tall and Special Buildings*, [e-journal] 25(15), pp.759-784. https://doi.org/10.1002/tal.1282.

Mai-Quang, K., Han, S.W., Shin, M. and Lee, K., 2017. Reduction of reinforcement congestion in slender coupling beam using bundled diagonal bars. *Magazine of Concrete Research*, [e-journal] 69(22), pp.1157-1169. https://doi.org/10.1680/jmacr.16.00530.

Metwally, I.M., 2017. Three-dimensional nonlinear finite element analysis of concrete deep beam reinforced with GFRP bars. *HBRC Journal*, [e-journal] 13(1), pp.25-38. https://doi.org/10.1016/j.hbrcj.2015.02.006.

Mohamed, A.R., Shoukry, M.S. and Saeed, J.M., 2014. Prediction of the behavior of reinforced concrete deep beams with web openings using the finite element method. *Alexandria Engineering Journal*, [e-journal] 53(2), pp.329-339. https://doi.org/10.1016/j.aej.2014.03.001.

Mohammadhassani, M., Nezamabadi-Pour, H., Suhatril, M. and Shariati, M., 2013. Identification of a suitable ANN architecture in predicting strain in tie section of concrete deep beams. *Struct Engineering and Mechanics*, [e-journal] 46(6), pp.853-868. https://doi.org/10.12989/sem.2013.46.6.853.

Nayal, R. and Rasheed, H.A., 2006. Tension stiffening model for concrete beams reinforced with steel and FRP bars. *Journal of Materials in Civil Engineering*, [e-journal] 18(6), pp.831-841. http://doi.org/10.1061/(ASCE)0899-1561(2006)18:6(831).

Osman, B.H.A., 2008. *Shear in R.C deep beams.* Master's Degree. University of Khartoum.

Pauw, A., 1960. Static modulus of elasticity of concrete as affected by density. *ACI Jorunal, Proceedings*, [e-journal] 57(12), pp.679-687. https://doi.org/10.14359/8040.

Raj, L. and Gangolu, A. R., 2013. Performance of RC deep beams with different combinations of web reinforcement. *Applied Mechanics and Materials*, [e-journal] Volume 343, pp.21-26. https://doi.org/10.4028/www.scientific.net/AMM.343.21.

Risser, R. and Hoffman, M., 2010. *Reinforcing Congestion*. [online] Available at: <https://www.concreteconstruction.net/how-to/materials/reinforcing-congestion_o> [Accessed 2 July 2020].

Saurabh and Yadav, Y., 2016. Literature review on finite element method. *International Journal of Enhanced Research in Science, Technology & Engineering*, 5(3).

Siow, S.Y., 2015. *Effect of opening with various size and location on RC deep beam*. Bachelor's Degree. Universiti Malaysia Pahang.

Solomon, S.K., Smith, D.W. and Cusens, A.R., 1976. Flexural tests of steel-concrete-steel sandwiches. *Magazine of Concrete Research*, 28(94), pp.13-20.

Tan, K.H., Tong, K. and Tang, C.Y., 2003. Consistent strut-and-tie modelling of deep beams with web openings. *Magazine of Concrete Research*, [e-journal] 55(1), pp.65-75. https://doi.org/10.1680/macr.2003.55.1.65.

Terng, O.K., 2019. *Flexural behaviour of reinforced concrete beams with 0.5 mm and 0.8 mm galvanised iron sheet as shear reinforcement*. Bachelor's degree. University of Tunku Abdul Rahman.

Wahalathantri, B.L., Thambiratnam, D.P., Chan, T.H.T. and Fawzia, S., 2011. *A material model for flexural crack simulation in reinforced concrete elements using ABAQUS*. In : QUT (Queensland University of Technology), 1st International postgraduate conference on engineering, designing, and developing the built environment for sustainable wellbeing. Brisbane, Australia, April 2011. Brisbane: Queensland University of Technology.

Wight, J.K. and MacGregor, J.G., 2011. *Reinforced concrete mechanics and design*. 6th ed. New Jersey: Prentice Hall.

Yang, K.H., Chung, H.S., Lee, E.T. and Eun, H.C., 2003. Shear characteristics of high-strength concrete deep beams without shear reinforcements. *Engineering Structures*, [e-journal] 25(10), pp.1343-1352. https://doi.org/10.1016/S0141-0296(03)00110-X.

Yang, K.H., Eun, H.C. and Chung, H.S., 2006. The influence of web openings on the structural behavior of reinforced high-strength concrete deep beams. *Engineering Structures*, [e-journal] 28(13), pp.1825-1834. https://doi.org/10.1016/j.engstruct.2006.03.021.

Zhang, Z., Hsu, C.T.T. and Moren, J., 2004. Shear strengthening of reinforced concrete deep beams using carbon fiber reinforced polymer laminates. *Journal of Composites for Construction*, [e-journal] 8(5), pp.403-414. https://doi.org/10.1061/(ASCE)1090-0268(2004)8:5(403).

Zhu, Y., Su, R.K.L. and Zhou, F.L., 2007. Seismic behavior of strengthened reinforced concrete coupling beams by bolted steel plates, Part 1: Experimental study. *Structural Engineering and Mechanics*, [e-journal] 27(2), pp.149-172. https://doi.org/10.12989/sem.2007.27.2.149.

APPENDICES

APPENDIX A: Design Calculations

Reference	Calculation
	Specification Concrete grade = C25/30 Concrete cover = 30 mm Beam length = 1100 mm Beam depth = 275 mm Beam width = 150 mm 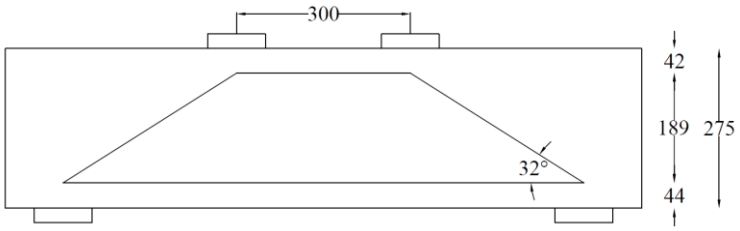 Figure A-1: Strut Detailing of Control Beam.
Goodchild, et al. (2014)	**Tie Depth and Lever Arm Design** Minimum tie depth required, $= 0.12 \times min\ (length, depth)$ $= 0.12 \times 275\ mm$ $= 33\ mm$ Actual tie depth, $= 46\ mm\ (> 33\ mm)\ OK!$ Lever arm requirement, $= [0.6 \times 275\ mm,\ \ 0.7 \times 275\ mm]$ $= [165\ mm,\ \ 192\ mm]$ Actual lever arm depth, $= 275\ mm - 45\ mm - 46\ mm$ $= 189\ mm (> 165\ mm < 192\ mm)\ OK!$

	<u>Node Allowable Stress</u>
BS EN 1992-1-1:2004 6.5.4	CCC node, $\sigma_{(Rd,max)CCC}$ $= 1.0\left(1 - \frac{f_{ck}}{250}\right)(0.85 f_{ck})$ $= 1.0\left(1 - \frac{25}{250}\right)(0.85 \times 25)$ $= 19.1\ MPa$
BS EN 1992-1-1:2004 6.5.4	CCT node, $\sigma_{(Rd,max)CCT}$ $= 0.85\left(1 - \frac{f_{ck}}{250}\right)(0.85 f_{ck})$ $= 0.85\left(1 - \frac{25}{250}\right)(0.85 \times 25)$ $= 16.3\ MPa$
BS EN 1992-1-1:2004 6.5.4	Concrete strut, $\sigma_{(Rd,max)strut}$ $= 0.85\left(1 - \frac{f_{ck}}{250}\right)(0.85 f_{ck})$ $= 0.85\left(1 - \frac{25}{250}\right)(0.85 \times 25)$ $= 16.3\ MPa$
	<u>Internal Force Analysis</u> a_v/z $= 300\ mm/\ 189\ mm$ $= 1.59\ (< \sqrt{3})$ ∴Type II Plastic model. Shear is taken by 1 major strut and 2 minor struts, as shown in Figure A-2. 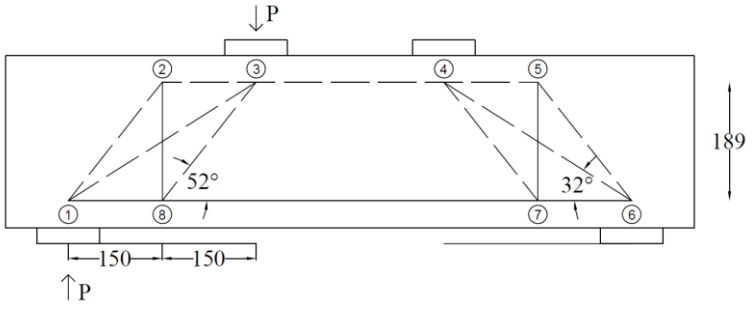 Figure A-2: Type II Plastic Model of Control Beam.

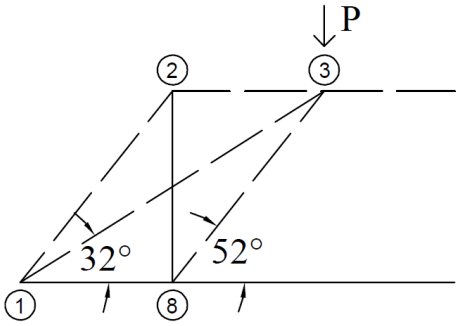

Figure A-3: Type II Concrete Strut.

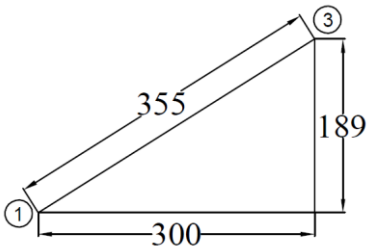

Figure A-4: Major Strut.

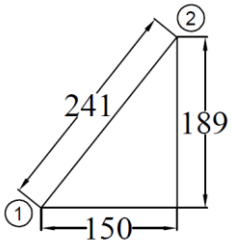

Figure A-5: Minor Strut.

Vertical compenent of minor strut,

$= \left(\frac{\frac{a_v}{z}-1}{\sqrt{3}-1}\right)P$

$= \left(\frac{1.59-1}{\sqrt{3}-1}\right)P$

$= 0.81P$

$= T_{28}$

Vertical compenent of major strut,

$= (1 - 0.86)P$

$= 0.14P$

Compression at major strut,

$= 0.14P \times \left(\frac{355}{189}\right)$

$= 0.26P$

$= C_{13}$

At Node 2,

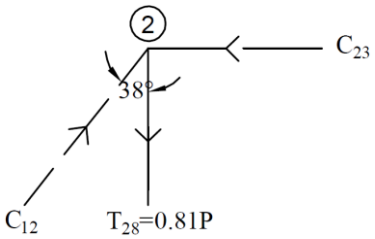

Figure A-6: Node 2.

$\Sigma F_y = 0$

$(C_{12})cos38° = T_{28}$

$(C_{12})cos38° = 0.81P$

$C_{12} = 1.03P$

$\Sigma F_x = 0$

$C_{23} = (C_{12})sin38°$

$C_{23} = (1.03P)sin38°$

$C_{23} = 0.63P$

At Node 1,

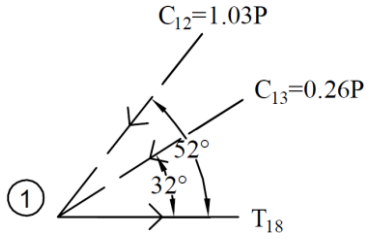

Figure A-7: Node 1.

$\Sigma F_x = 0$

$T_{18} = (C_{12})cos52° + (C_{13})cos32°$

$T_{18} = (1.03P)cos52° + (0.26P)cos32°$

$T_{18} = 0.85P$

At Node 8,

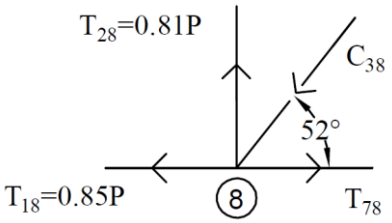

Figure A-8: Node 8.

Since C_{38} has similar angle as C_{12}

$\therefore C_{38} = C_{12} = 1.03P$

$\Sigma F_x = 0$

$T_{78} = T_{18} + (C_{38})cos52°$

$T_{78} = 0.85P + (1.03P)cos52°$

$T_{78} = 1.48P$

At Node 3,

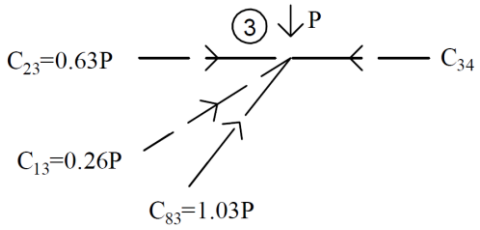

Figure A-9: Node 3.

$\Sigma F_x = 0$

$C_{34} = C_{23} + (C_{13})cos32° + (C_{83})cos52°$

$C_{34} = 0.63P + (0.26P)cos32° + (1.03P)cos52°$

$C_{34} = 1.48P$

Summary of internal forces,

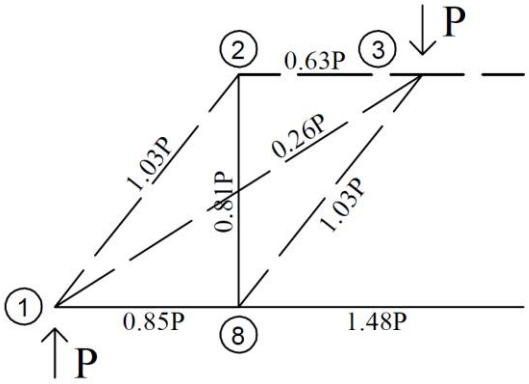

Figure A-10: Summary of Strut Interal Forces.

Combing major strut (Node 1-3) and minor strut (Node 1-2)

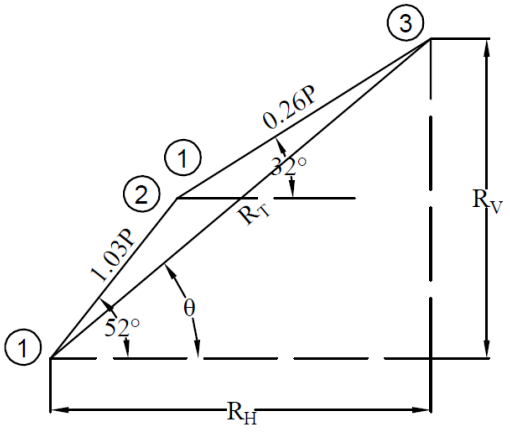

Figure A-11: Combined Struts.

$$R_V = (C_{12})sin52° + (C_{13})sin32°$$
$$R_V = (1.03P)sin52° + (0.26P)sin32°$$
$$R_V = 0.95P$$

$$R_H = (C_{12})cos52° + (C_{13})cos32°$$
$$R_H = (1.03P)cos52° + (0.26P)cos32°$$
$$R_H = 0.85P$$

$$R_T = \sqrt{(0.95P)^2 + (0.85P)^2} = 1.27P$$
$$\theta = tan^{-1}(\frac{0.95}{0.85}) = 48°$$

Hee, M. C. (2014)	**Shear Design** Bursting tensile force in strut, 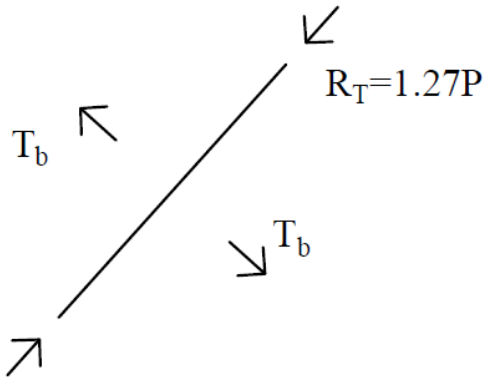 Figure A-12: Bursting Tensile Force in Strut. Consider ultimate limit state, $tan(\alpha) = 1/5$ Bursting tensile force, $T_b = R_T\, tan(\alpha)$ $T_b = 1.27P(1/5)$ $T_b = 0.25P$ 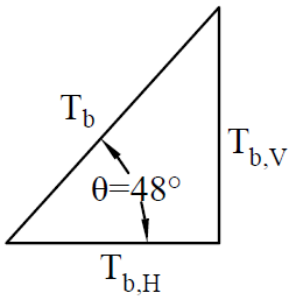 Figure A-13: Components of Bursting Tensile Force. $T_{b,V} = (T_b)sin48°$ $T_{b,V} = (0.25P)sin48°$ $T_{b,V} = 0.19P$ $T_{b,H} = (T_b)cos48°$ $T_{b,H} = (0.25P)cos48°$ $T_{b,H} = 0.17P$

	For bursting, $A_{sV,req} = T_{b,V}/f_{yk}$ $A_{sV,req} = 0.19P/500$ $A_{sV,req} = (0.00038P)mm^2$ $A_{sH,req} = T_{b,H}/f_{yk}$ $A_{sH,req} = 0.17P/500$ $A_{sH,req} = (0.00034P)\ mm^2$ For vertical shear, $A_{sv,req} = T_{28}/f_{yk}$ $A_{sv,req} = 0.81P/500$ $A_{sv,req} = (0.00162P)\ mm^2$ Total reinforcement area required, $(A_{sv,req})_{total} = max\{A_{sV,req}, A_{sH,req}\} + A_{sv,req}$ $(A_{sv,req})_{total} = max\{0.00038P, 0.00034P\} + 0.00162P$ $(A_{sv,req})_{total} = (0.002P)mm^2$ Reinforcement area provided, $A_{sv,prov} = 2\ sides \times T8$ $A_{sv,prov} = 2\ sides \times \pi \times (4\ mm)^2$ $A_{sv,prov} = 100.50\ mm^2$ Allowable shear force (from shear reinforcement only), $(P_{sv,allow})_{reinforcement} = A_{sv,prov}/(A_{sv,req})_{total}$ $(P_{sv,allow})_{reinforcement} = 100.50/0.002$ $(P_{sv,allow})_{reinforcement} = 50\ kN$

	Effective depth, $d = h - C_{nom} - 0.5\emptyset_{bar}$ $d = 275 - 44 - 0.5(12)$ $d = 225\ mm$ Shear resistance of concrete, $v_c = min\left\{\frac{100A_s}{bd}, 0.8\sqrt{fck}, 5\ N/mm^2\right\}$ $\frac{100A_s}{bd} = \frac{100(2 \times \pi \times 6^2)}{150 \times 225} = 0.67$ $0.8\sqrt{fck} = 0.8\sqrt{25} = 4\ N/mm^2$ $v_c = min\{0.67,4,5\} = 0.67\ N/mm^2$ Allowable shear force (from concrete only), $V_c = v_c \times b \times d$ $V_c = 0.67 \times 150 \times 225$ $V_c = 23kN$ Total allowable shear force, $(P_{sv,allow})_{total} = (P_{sv,allow})_{reinforcement} + V_c$ $(P_{sv,allow})_{total} = 50 + 23$ $(P_{sv,allow})_{total} = 73kN$
Hee, M. C. (2014)	**<u>Tension Tie Design</u>** Reinforcement area required, $(A_{sf,req})_{total} = max\{T_{18}, T_{87}\}/f_{yk}$ $(A_{sf,req})_{total} = max\{0.85P, 1.48P\}/500$ $(A_{sf,req})_{total} = (0.00296P)mm^2$ Reinforcement area provided, $A_{sf,prov} = 2T12$ $A_{sf,prov} = 2\ \times \pi \times (6\ mm)^2$ $A_{sf,prov} = 226.19\ mm^2$

	Total allowable flexural force, $(P_{sf,allow})_{total} = A_{s,prov}/(A_{s,req})_{total}$ $(P_{sf,allow})_{total} = 226.19/0.00296$ $(P_{sf,allow})_{total} = 76kN$
	Conclusion From the calculations above, the total allowable flexural force is larger than the total allowable shear force. $(P_{sf,allow})_{total} = 76kN > (P_{sv,allow})_{total} = 73kN$ It can be concluded that the designated specimen would fail in shear instead of flexural, thereby meeting the scope of study.

APPENDIX B: Test Results Graphics

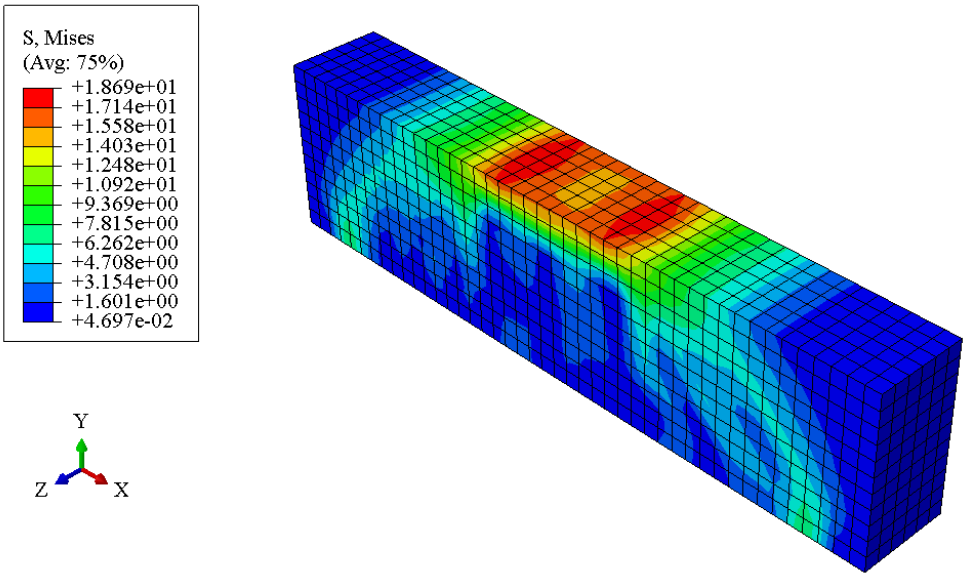

Figure B-1: Concrete Von Mises Stress Contour of N50 at 1.5 mm.

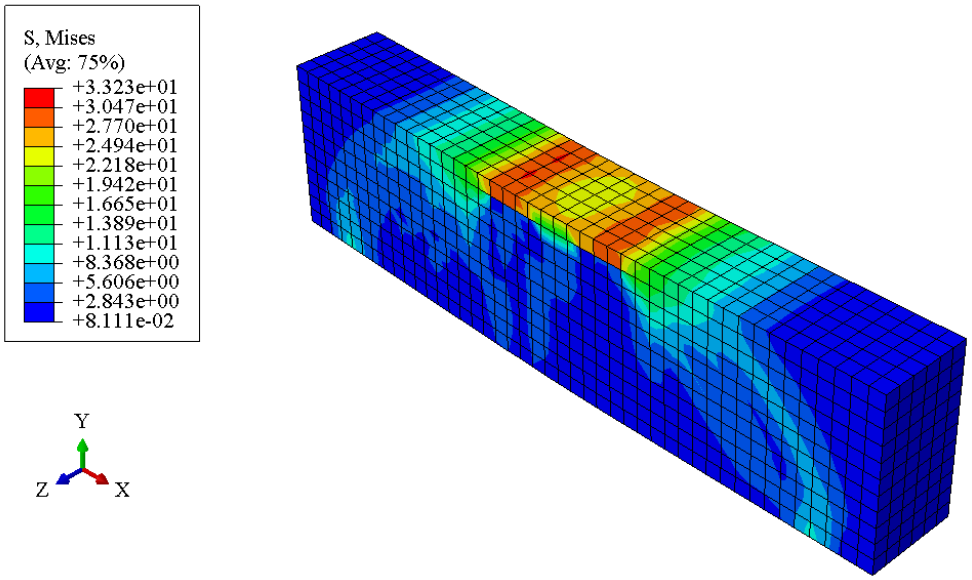

Figure B-2: Concrete Von Mises Stress Contour of N50 at 10 mm.

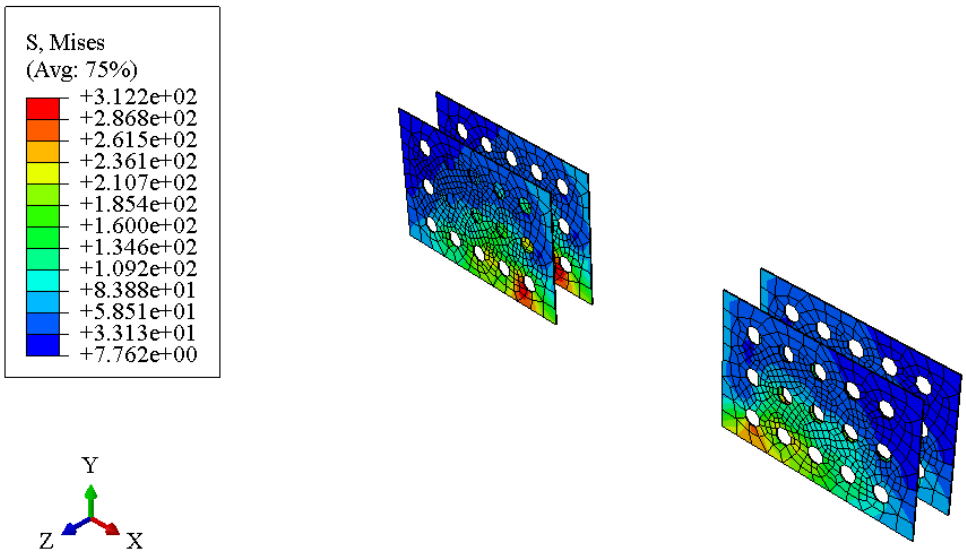

Figure B-3: Reinforcement Von Mises Stress Contour of N50 at 1.5 mm.

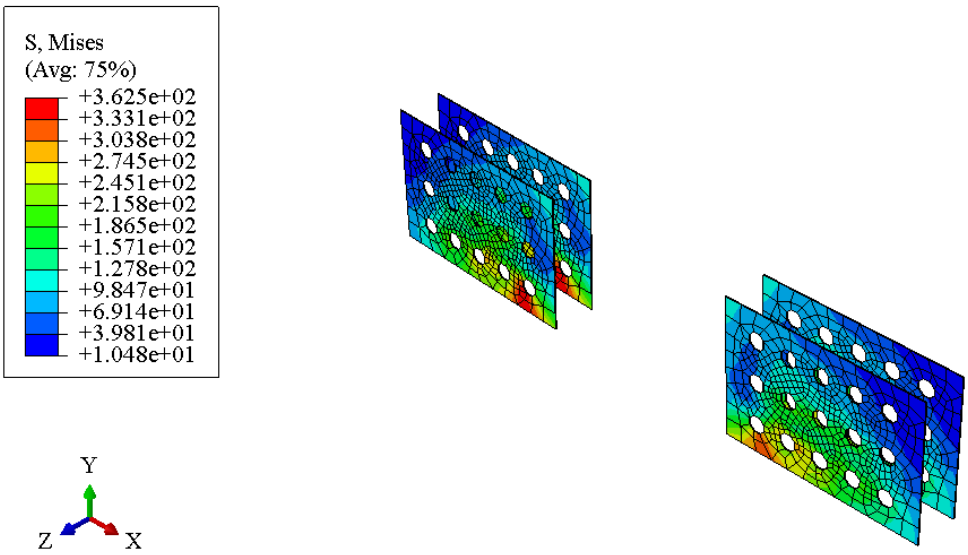

Figure B-4: Reinforcement Von Mises Stress Contour of N50 at 10 mm

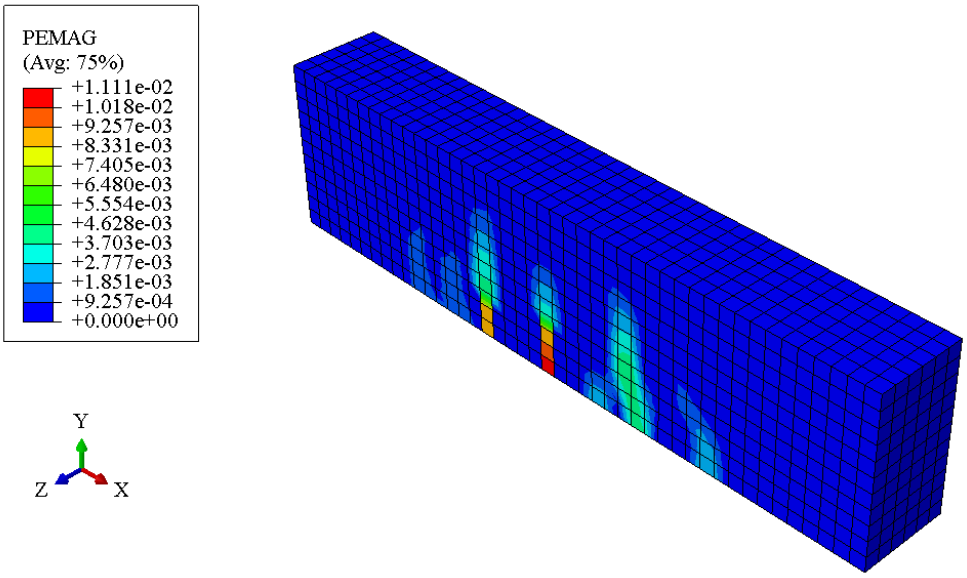

Figure B-5: PEMAG Diagram of N50 at 1.5 mm.

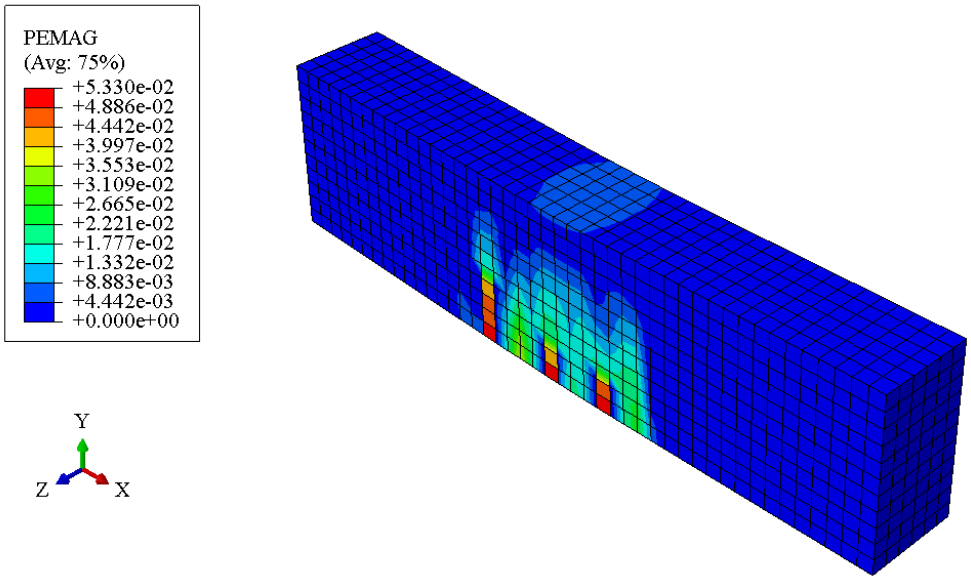

Figure B-6: PEMAG Diagram of N50 at 10 mm..

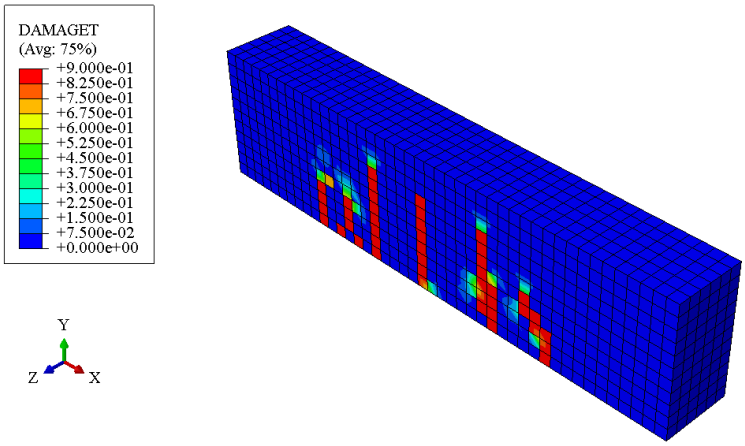

Figure B-7: Tension Damage Contour of N50 at 1.5 mm.

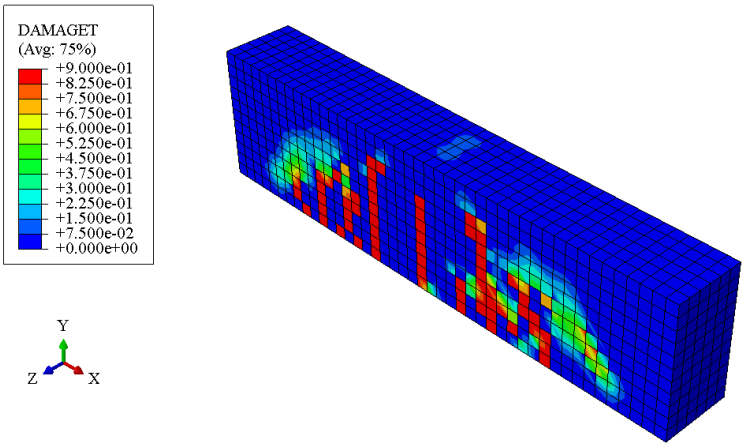

\

Figure B-8: Tension Damage Contour of N50 at 6 mm.

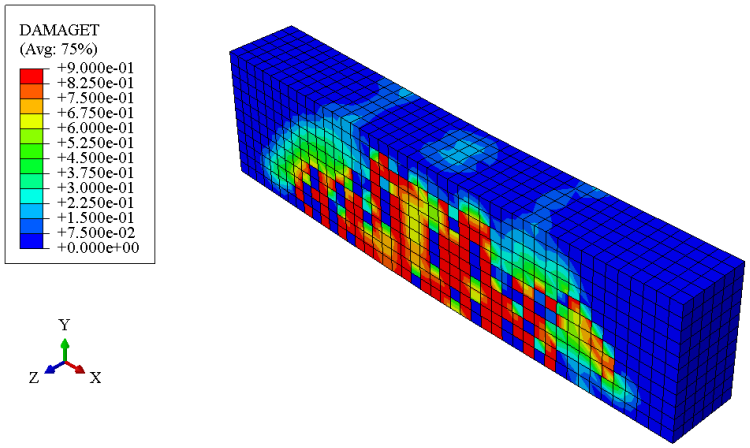

Figure B-9: Tension Damage Contour of N50 at 10 mm.

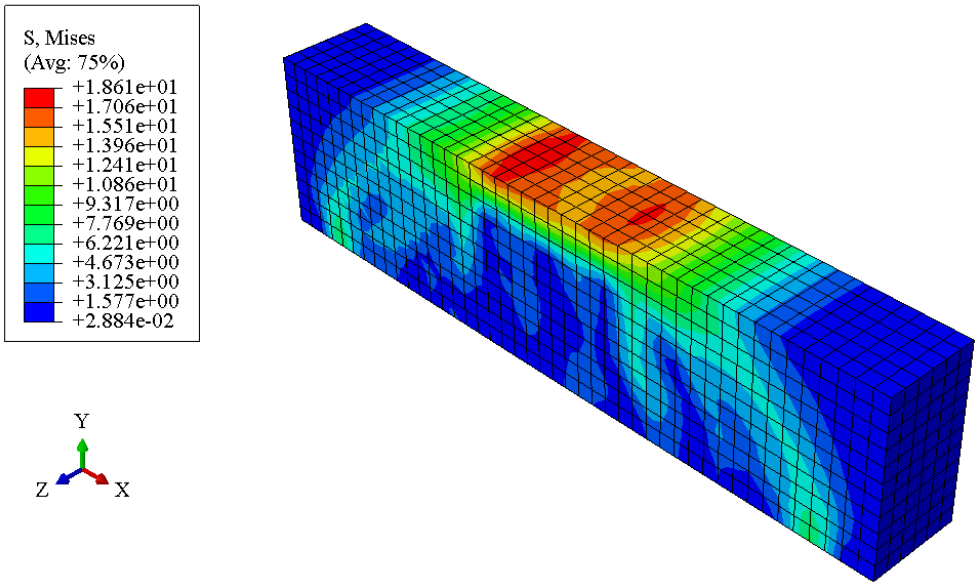

Figure B-10: Concrete Von Mises Stress Contour of N75 at 1.5 mm.

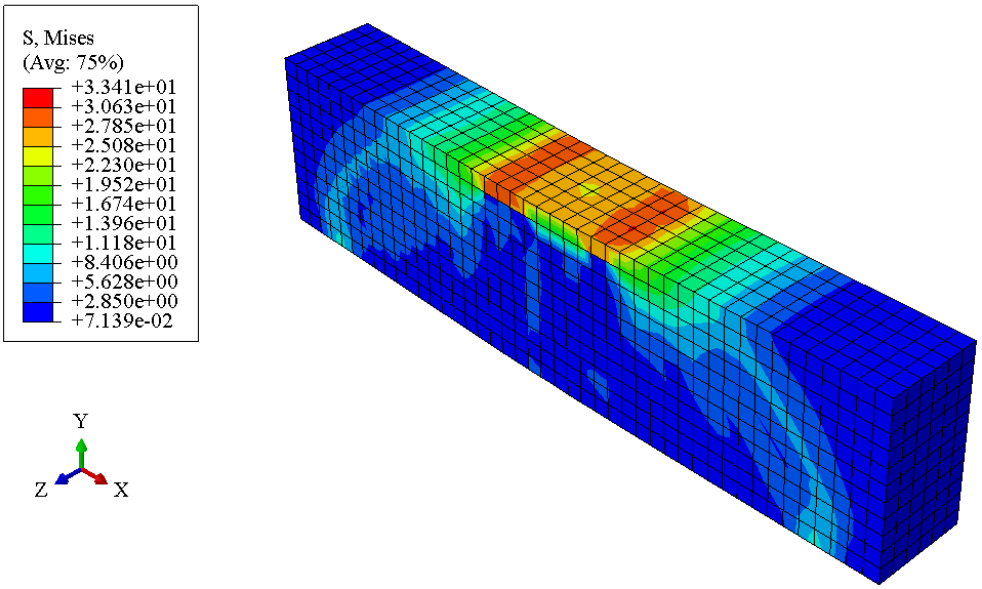

Figure B-11: Concrete Von Mises Stress Contour of N75 at 10 mm.

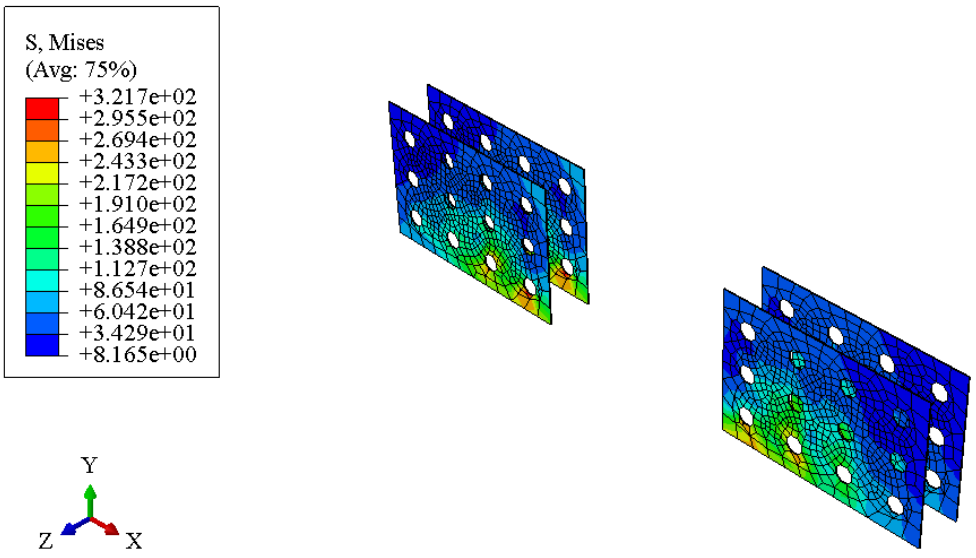

Figure B-12: Reinforcement Von Mises Stress Contour of N75 at 1.5 mm.

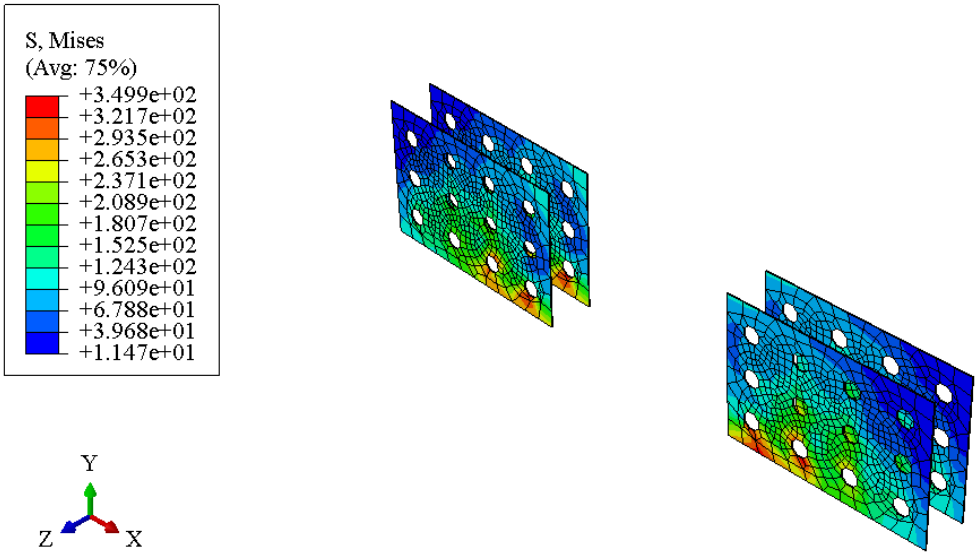

Figure B-13: Reinforcement Von Mises Stress Contour of N75 at 10 mm.

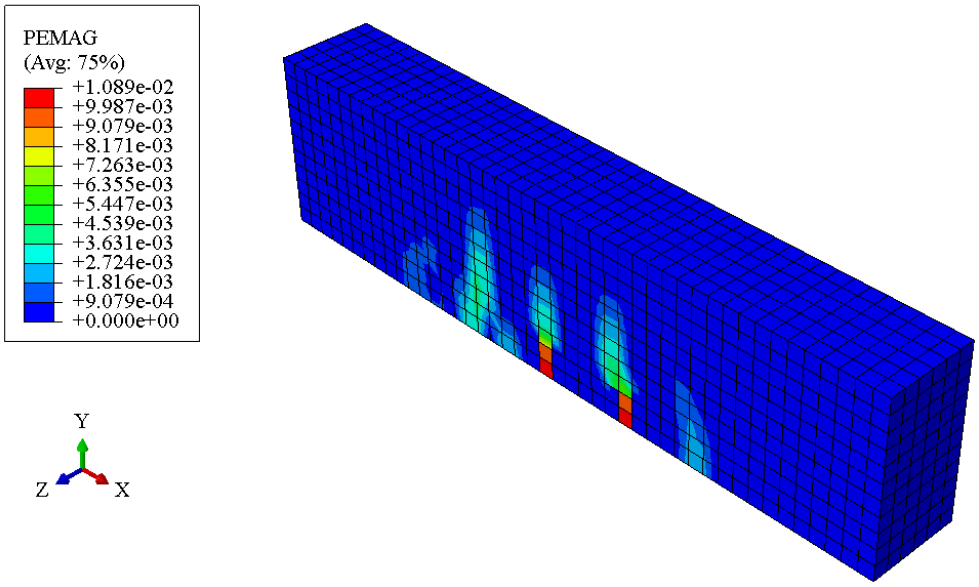

Figure B-14: PEMAG Diagram of N75 at 1.5 mm.

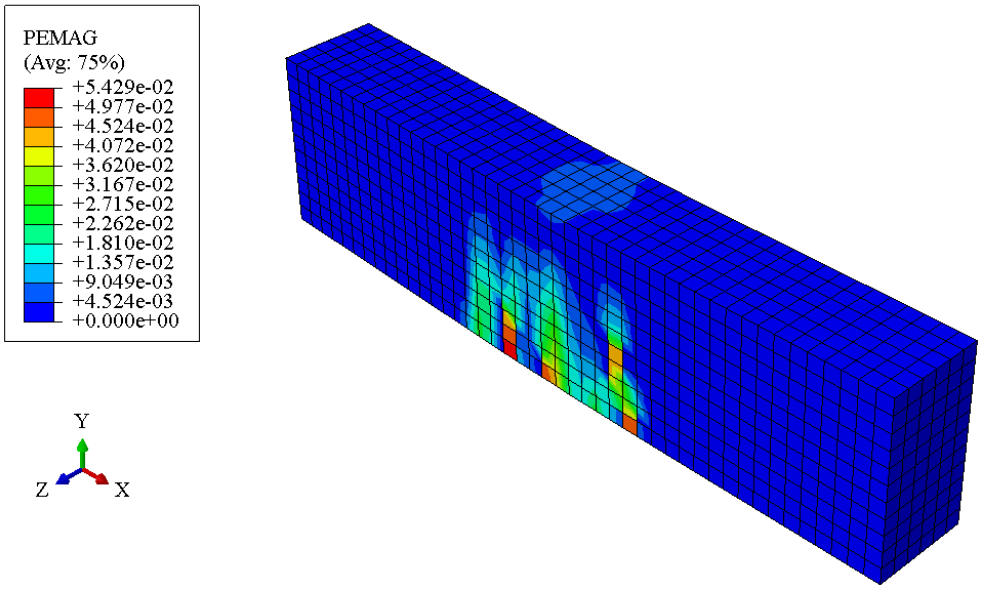

Figure B-15: PEMAG Diagram of N75 at 10 mm.

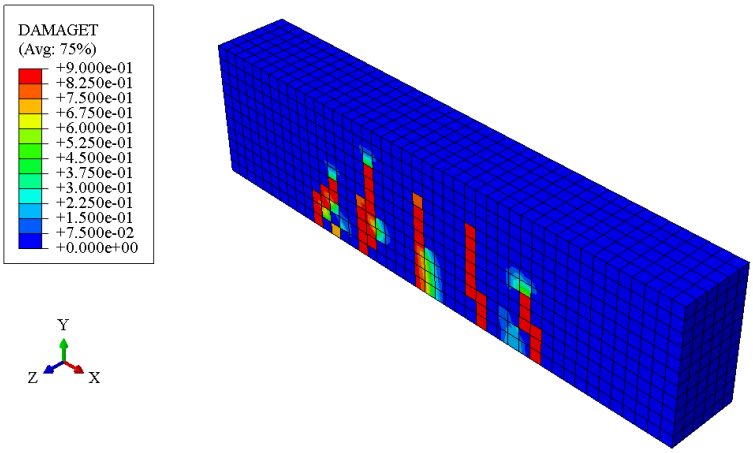

Figure B-16: Tension Damage Contour of N75 at 1.5 mm.

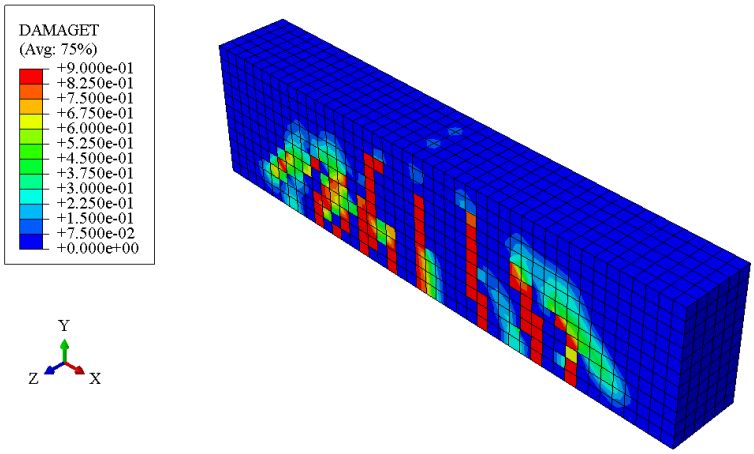

Figure B-17: Tension Damage Contour of N75 at 6 mm.

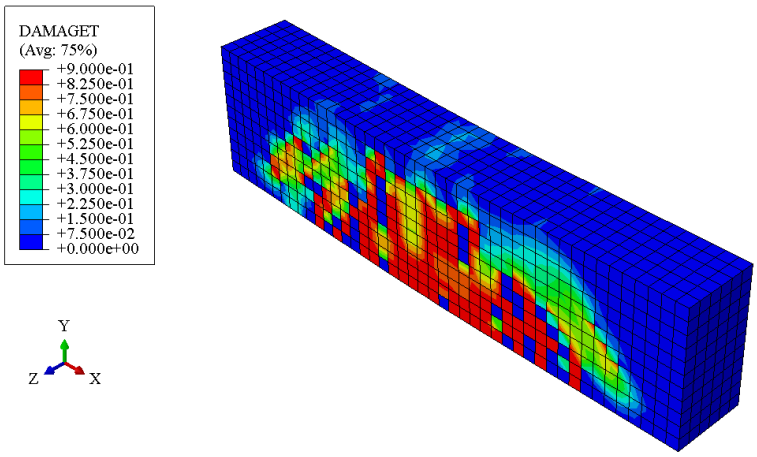

Figure B-18: Tension Damage Contour of N75 at 10 mm.

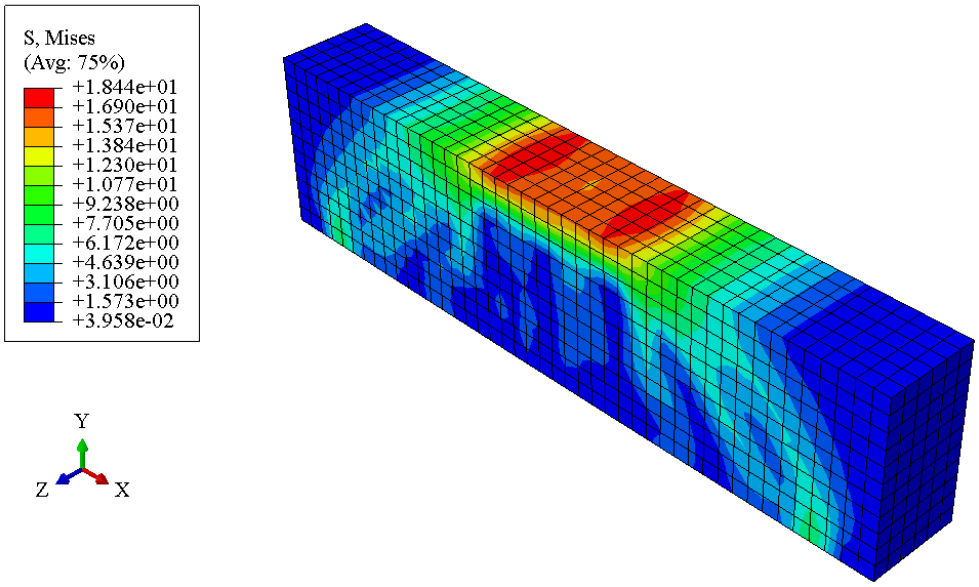

Figure B-19: Concrete Von Mises Stress Contour of N125 at 1.5 mm.

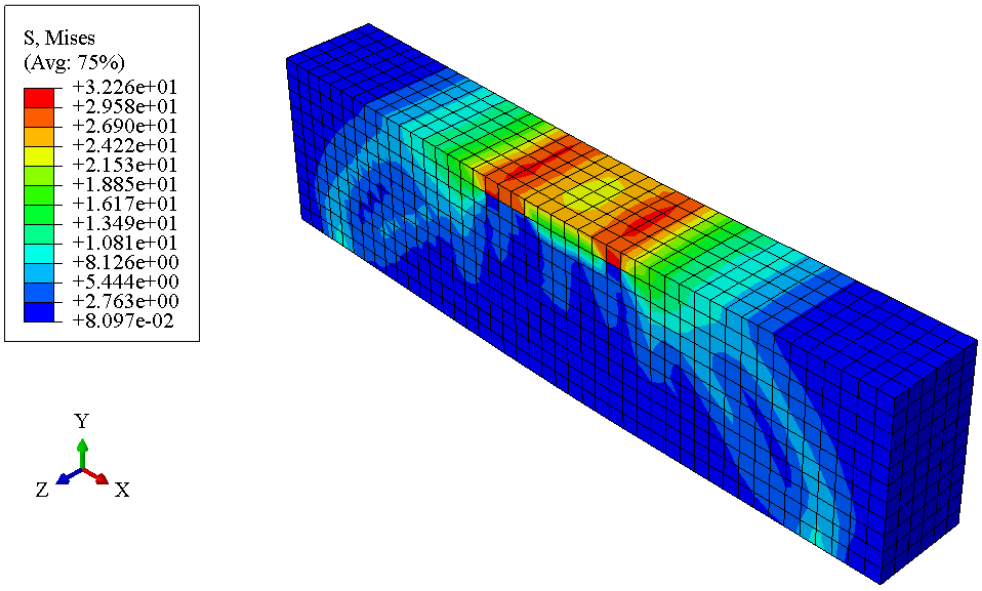

Figure B-20: Concrete Von Mises Stress Contour of N125 at 10 mm.

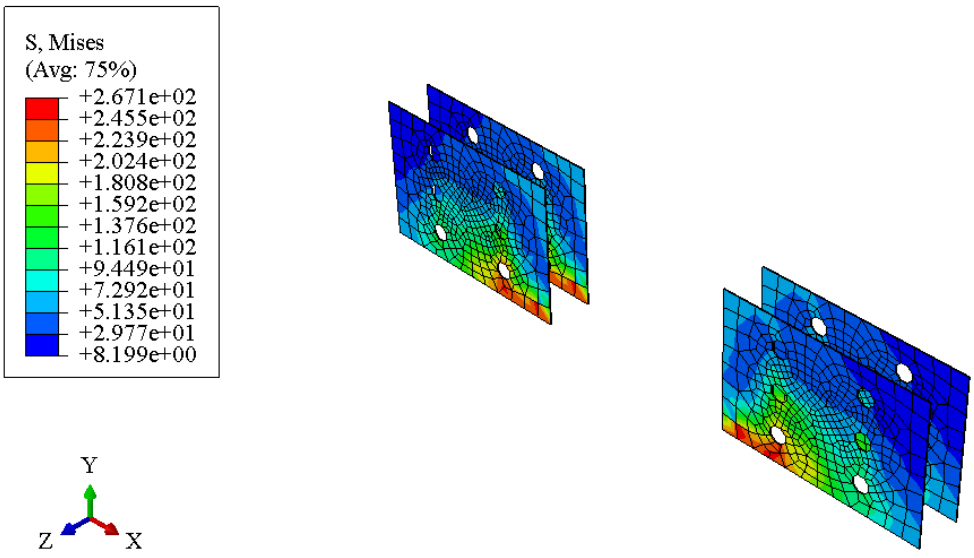

Figure B-21: Reinforcement Von Mises Stress Contour of N125 at 1.5 mm

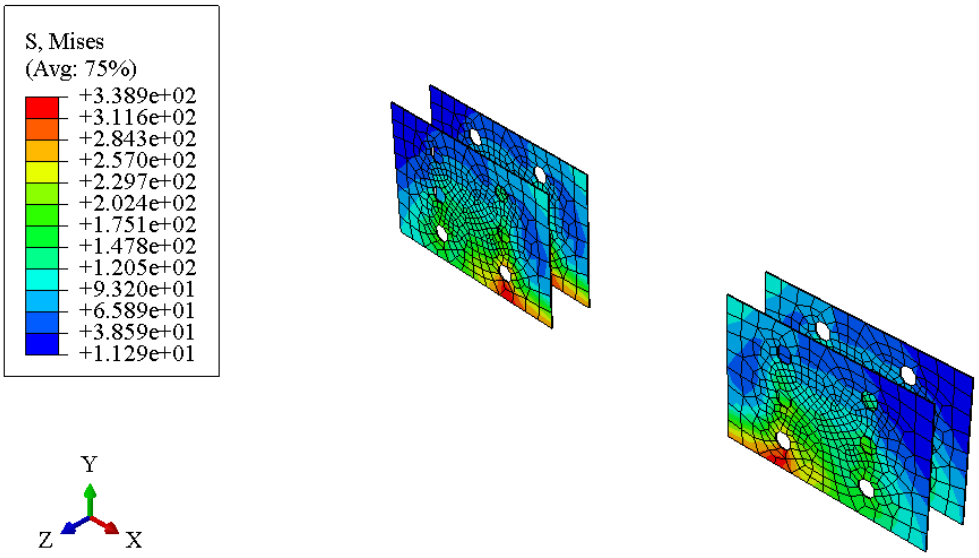

Figure B-22: Reinforcement Von Mises Stress Contour of N125 at 10 mm

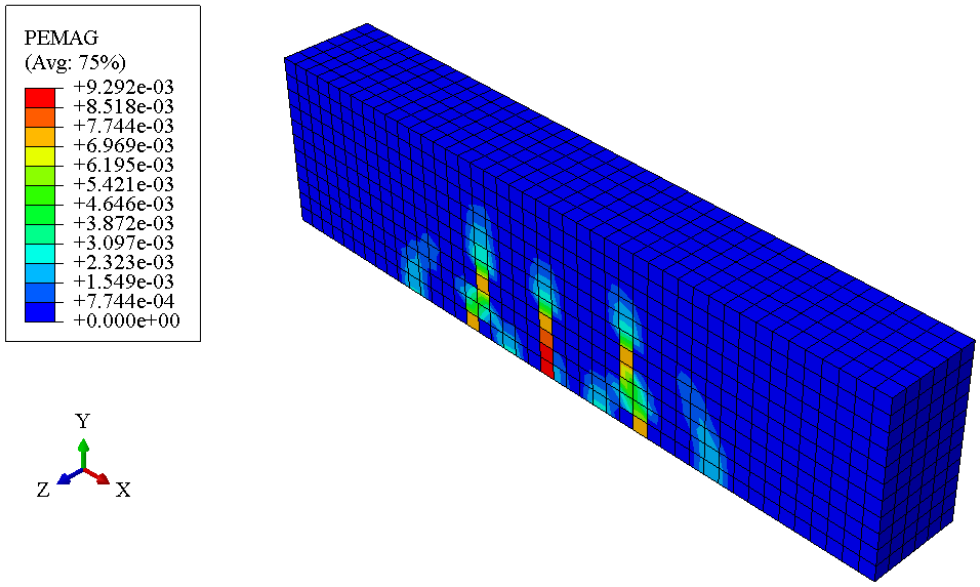

Figure B-23: PEMAG Diagram of N125 at 1.5 mm.

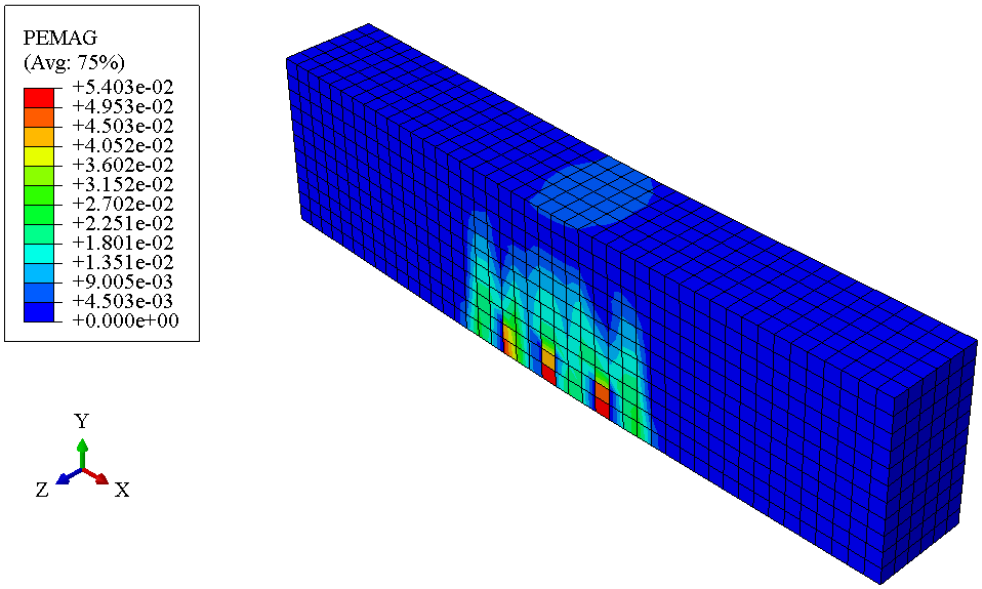

Figure B-24: PEMAG Diagram of N125 at 10 mm.

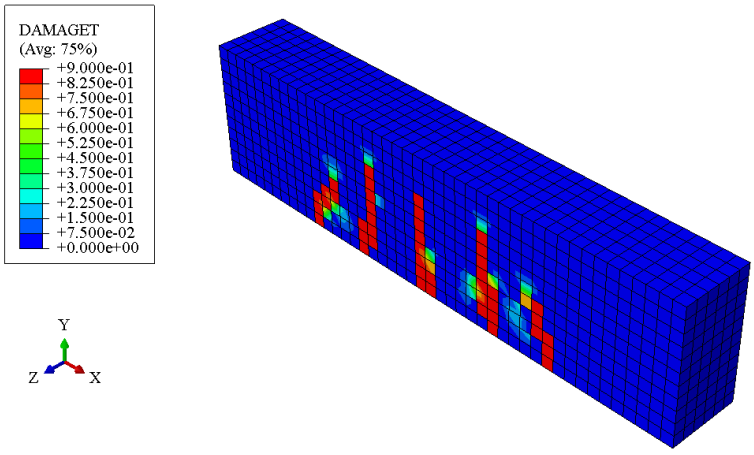

Figure B-25: Tension Damage Contour of N125 at 1.5 mm.

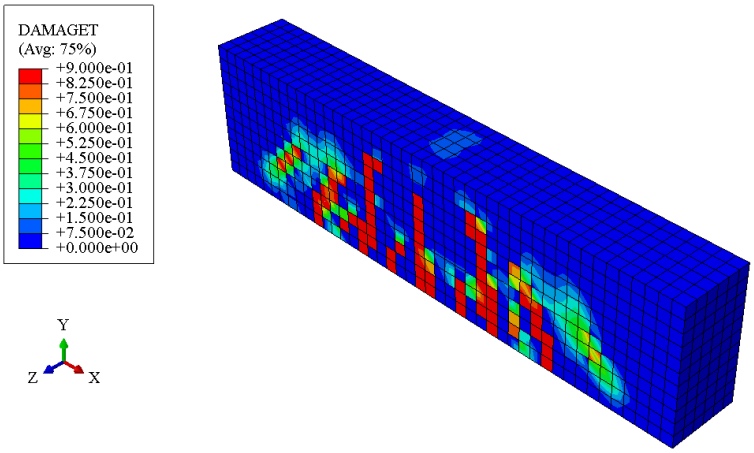

Figure B-26: Tension Damage Contour of N125 at 6 mm.

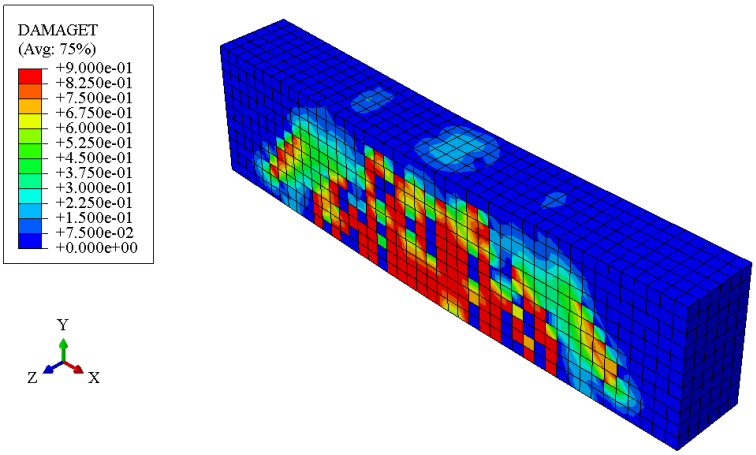

Figure B-27: Tension Damage Contour of N125 at 10 mm.

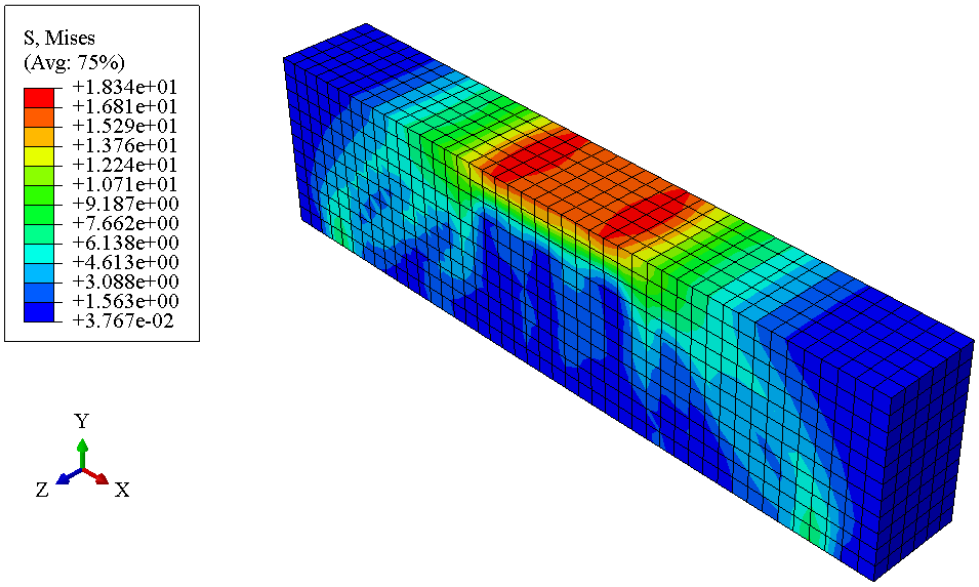

Figure B-28: Concrete Von Mises Stress Contour of N150 at 1.5 mm.

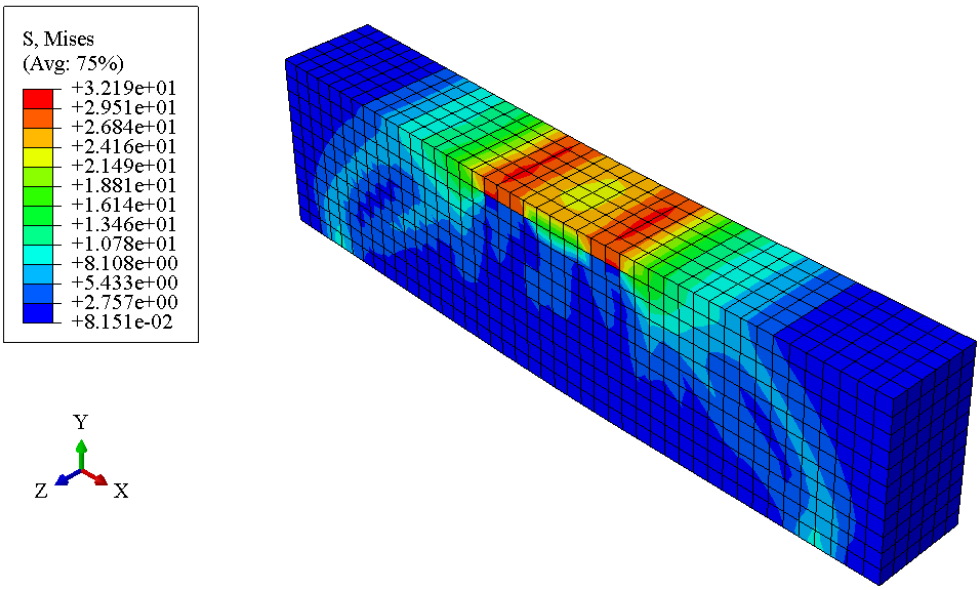

Figure B-29: Concrete Von Mises Stress Contour of N150 at 10 mm.

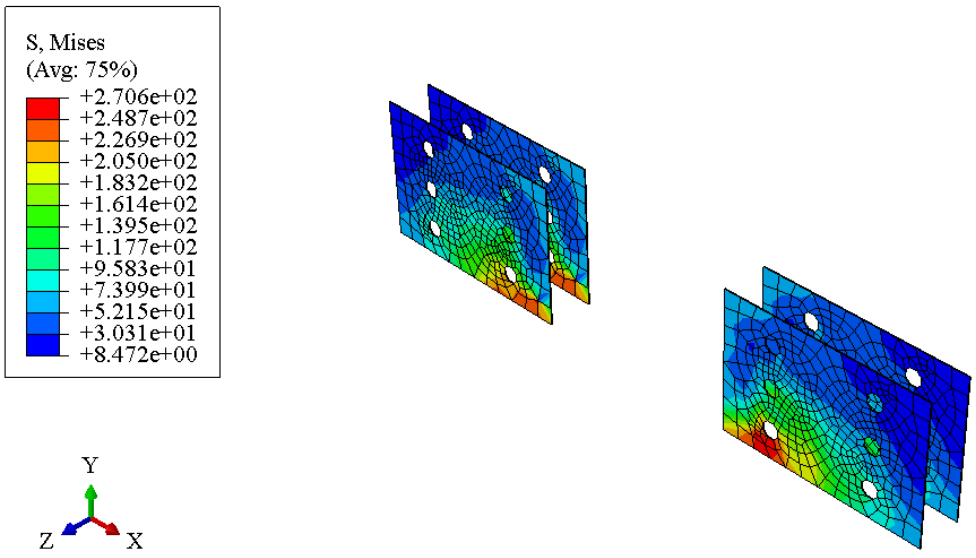

Figure B-30: Reinforcement Von Mises Stress Contour of N150 at 1.5 mm

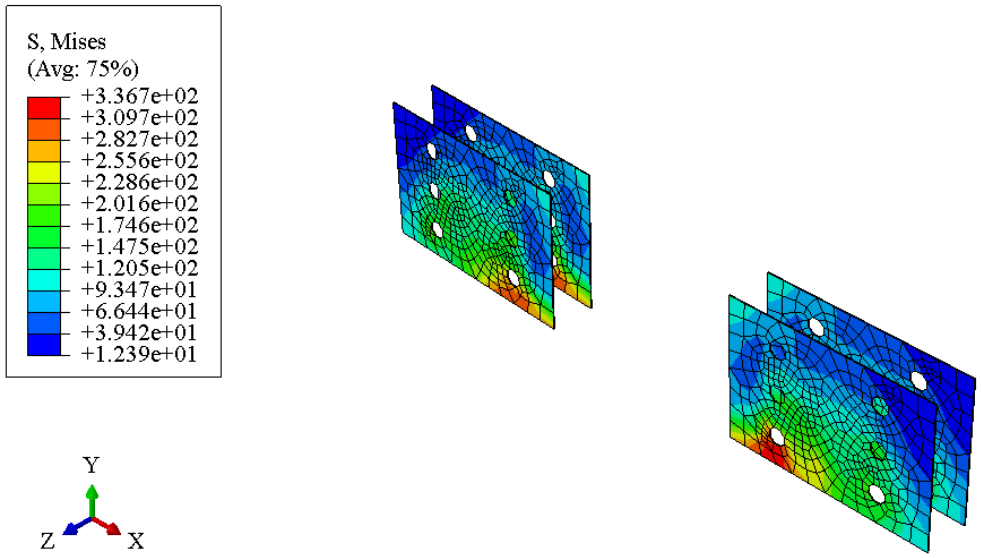

Figure B-31: Reinforcement Von Mises Stress Contour of N150 at 10 mm

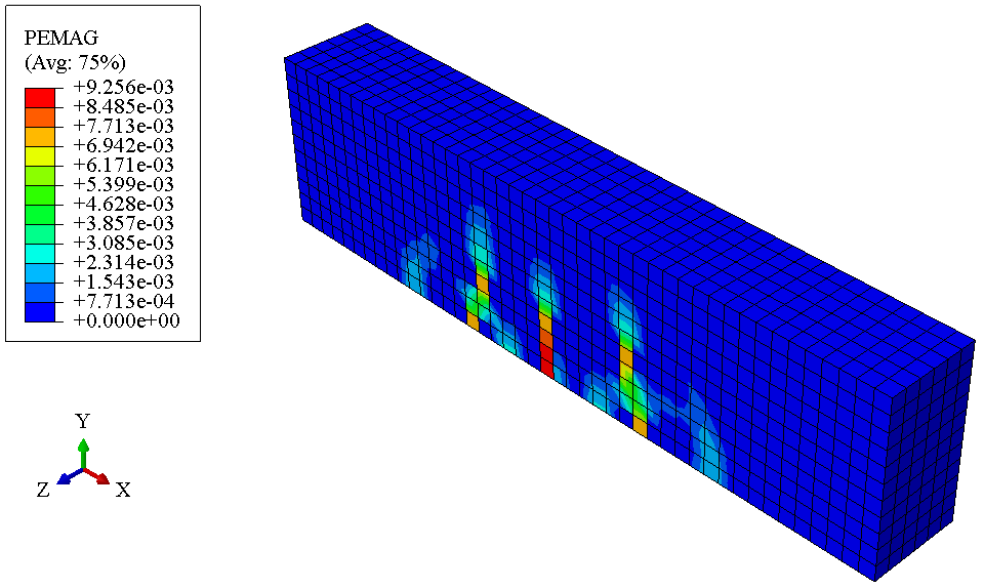

Figure B-32: PEMAG Diagram of N150 at 1.5 mm.

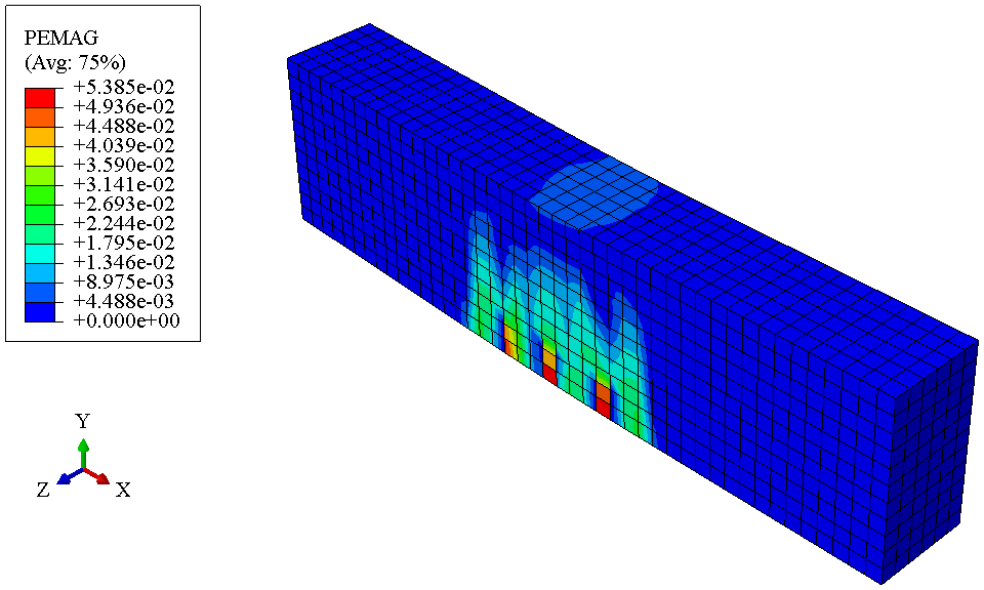

Figure B-33: PEMAG Diagram of N150 at 10 mm.

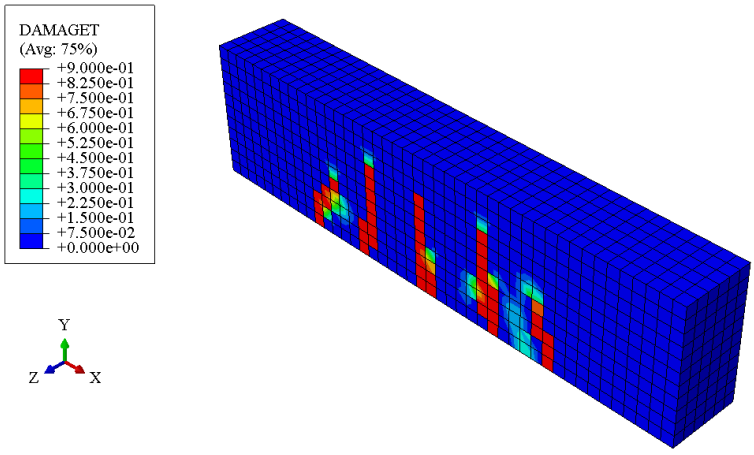

Figure B-34: Tension Damage Contour of N150 at 1.5 mm.

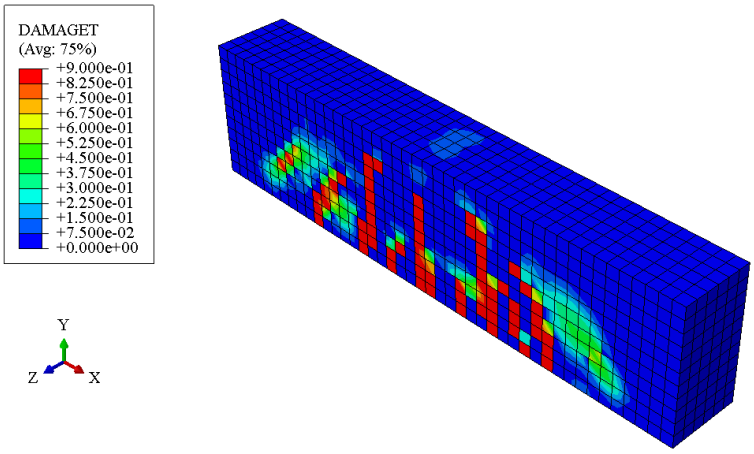

Figure B-35: Tension Damage Contour of N150 at 6 mm.

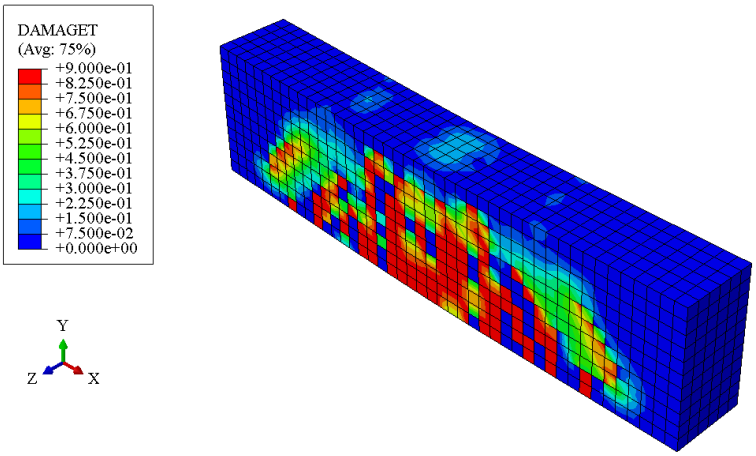

Figure B-36: Tension Damage Contour of N150 at 10 mm.